Advanced Applications of Nanoelectromechanical Systems

Thesis by

Peter Hung

In Partial Fulfillment of the Requirements for
the degree of
Doctor of Philosophy

CALIFORNIA INSTITUTE OF TECHNOLOGY
Pasadena, California

2016
(Defended May 24, 2016)

© 2016

Peter Hung
ORCID: 0000-0002-9034-5330

ACKNOWLEDGEMENTS

First and foremost, I would like to express my deepest gratitude to my advisor, Professor Michael Roukes, for his support throughout my graduate career. He has given me the freedom to work on various research projects over the years and he has always been supportive. He has also given me the opportunity to mentor many students throughout the years, ranging from high school student volunteers to SURF Fellows, and allowed me to serve as a teaching assistant for various classes. Last but not least, when he curated the inaugural TEDxCaltech early in my graduate career, he invited me to be part of the team that made it all happened. He has given me everything so that I can have a balanced set of skills in leading, teaching, mentoring, and performing research.

I also want to thank Professor Philip Feng who taught me everything there is to know about nano systems, from fabrication to measurement. He walked with me through challenges in research and in life and shared with me common pitfalls in graduate schools so I could avoid them. He treated me as one of his own children and has continued to mentor me after he started his professorship at Case Western.

Many others in the Roukes Group advised and supported me over the years: Dr. Warren Fon, Professor Luis Guillermo Villanueva, Dr. Rassul Karabalin, Derrick Chi, Professor Mehmet Selim Hanay, Dr. Matthew Matheny, Dr. Eric Sage, Professor Akshay Naik, and Dr. Scott Kelber. I also want to thank the many students whom I have had the pleasure of working with throughout the past few years. I will never forget the first summer in the Roukes Group when Professor Feng and I together mentored simultaneously three students: Josh Yoon- a freshman at the time and now graduate student at Stanford University Abraham Chien- a sophomore at the time and now graduate student at Princeton University, Derek Chou- a high school junior at the time and now a graduate student at the University of Illinois at Urbana-Champaign. Thanks to their different work schedules, I was able to work with each of them for part of the day on different graphene related projects, even if that meant we were often in the cleanroom until 4:00 AM. I am grateful for other students whom I have worked with: Marcus Bintz, Corwin Shiu, Max Jones, and two of my current officemates: Jarvis Li and Alex Place.

I have been very fortunate to have collaborated with some of the world's best theorists in my thesis work. I cannot thank Professors Michael Cross, Ron Lifshitz, and John Sader enough for working through calculation after calculation with me, especially since theory is not my strongest subject.

I want to thank my wonderful officemates Dr. Caryn Bullard, Jarvis Li, Alex Place, and Paula Popescu for their day to day support in the office and in the lab. They have provided moral support and technical support whenever there was a need for either. I especially want to thank Jarvis Li and Alex Place for continuing our research in the Roukes Group after they completed their summer fellowships. Much of the work in this thesis would not have been possible without their hard work. I also want to take this opportunity to wish Jarvis Li all the best now that he has started his own project as a graduate student in the Roukes Group.

I sincerely thank the rest of our research group and extended research group Su Naing, Loly Ekmekjian, Dr. Ed Myers, Dr. Jessica Arlett, Professor Erik Henriksen, Dr. Xinchang Zhang, Dr. Jean-Sebastien Moulet, and Dr. Sebastien Hentz.

There are also many individuals outside of the research group, without whom, this thesis would not be possible. Special thanks to my thesis committee members and my candidacy committee members: Professor Michael Cross, Professor Jim Eisenstein, Professor Oskar Painter, Professor Keith Schwab, and Professor Nai-Chang Yeh. I also want to thank the Kavli Nanoscience Institute (KNI), where all of the devices in this thesis were fabricated, and all the staff of the KNI who has made my research possible: Mary Sikora, Dr. Guy DeRose, Melissa Melendes, Nils Asplund, and Matt Sullivan.

I also want to thank Frank Rice for many hours of physics discussions, may it be a new way to understanding an old physics principle, the labs we teach in the Sophomore Physics Lab, my research, or the best method for analyzing particular sets of data. He is an amazing teacher and he does everything so that the teaching assistants in his course can be successful teachers as well. If it had not been Frank, I would not have received the Associated Students of California Institute of Technology (ASCIT) Teaching Award nor the inaugural R. Bruce Stewart Prize for Excellence in Teaching Physics.

I want to especially thank the Graduate Office and the Deans Office for their continuous support throughout my tenure here at Caltech. Vice President of Student Affairs, Professor Joseph Shepherd, Assistant Vice President for Equity, Accessibility, & Inclusion Initiatives, & Title IX Coordinator, Dr. Felicia Hunt, Interim Dean of Students, Dr. Barbara Green, and Office Manager in the Deans of Students office, Rosemary Beth Larranaga have been an integral part of my success at Caltech. Whenever there were any issues, they were always there to help me in every possible way.

I also want to thank the Student Faculty Program (SFP) Office for their support and guidance both through my undergraduate and my graduate career here at Caltech. Without the SFP Office, I would not have had the opportunity to work with so many amazing students. They have given me the skills I need to be an effective mentor. Last but not least, I want to thank them for their constant moral support over the past few months as I finish my thesis. They have always said that "it takes village to help Peter graduate" and they have truly provided the support of a whole village.

The Caltech Y has played a huge role in my development as a leader and a member of the community. They have consistently reminded me and many students that there is a whole world outside of Caltech that we live in. I have been fortunate to have had the opportunity to work with the Caltech Y Board, staff, and the Student Executive Committee and serve as their President during this past year.

There are many other offices and groups on campus that I need to thank: Thomas Mannion in the Student Activities and Programs Office, Joseph Lima from the Development Office, the Graduate Student Council, the Graduate Honor Council, The Gnome Club, the Center for Teaching, Learning, and Outreach, and last but not least, the many leaders over the years in the Science Olympiad club. They have all helped me balance the intense academic demands here at Caltech.

I want to thank the Aerospace Corporation for sponsoring my summer research and all of my summer students' research during the past years. I want to especially thank Dr. Gary Stupian, Dr. Martin Leung, Joe Cheng, and Dr. Maribeth Mason for their continuous support.

I thank all my friends and mentors who have been so supportive throughout the years. I want to especially thank my mentors outside of Caltech: Dr. Allen Leung, Jenny Leung, Kerry King, and Dr. Ed Rodevich. I also want to thank my friends who were during the tougher times: Joe Salamon, Rico Chiu, Alan Deng, Calvin Yu, Ye Pei, Chris Li, Alex Chao, Adam Jermyn, Lyra Cao, Tony Zhang, Joseph Berleant, Kristie Yu, and Phillip Liu.

Finally, I owe so many to my family and I cannot find the words to express how much I appreciate all that they have sacrificed for me. While neither of my parents finished middle school, they valued the importance of education and uplifted their roots so that I could have the top notch education available here.

ABSTRACT

Nanoelectromechanical systems (NEMS) have advanced the technologies in a wide spectrum of fields, including nonlinear dynamics, sensors for force detection, mass spectrometry, inertial imaging, calorimetry, and charge sensing. Due to their low power consumption, fast response time, large dynamic range, high quality factor, and low mass, NEMS have achieved unprecedented measurement sensitivity. For optimized system functionalization and design, precise characterization of material properties at the nanoscale is essential. In this thesis, we will discuss three applications of NEMS: mechanical switches, using anharmonic nonlinearity to measure device and material properties, and mass spectrometry and inertial imaging.

The first application of NEMS we discuss is NEMS switches, switches with physical moving parts. Conventional electronics, based largely on silicon transistors, is reaching a physical limit in both size and power consumption. Mechanical switches provide a promising solution to surpass this limit by forcing a jump between the on and off states. Graphene, which is a single sheet of carbon atoms arranged in a hexagonal structure, has high mechanical strength and strong planar bonding, making it an ideal candidate for nanoelectromechanical switches. In addition, graphene is conductive, which decreases resistive heating at the contact area, therefore reducing bonding issues and subsequently reducing degradation. We demonstrate using exfoliated graphene to fabricate suspended graphene NEMS switches with successful switching.

The second application of NEMS we discuss in this thesis is the use of mechanical nonlinearity to measure device and material properties. While the nonlinear dynamics of NEMS have been used previously to investigate the longitudinal speed of sound of materials

at nano- and micro-scales, we correct a previously attempted method that employs the anharmonicity of NEMS arising from deflection-dependent stress to interrogate the transport of RF acoustic phonons at nanometer scales. In contrast to existing approaches, this decouples intrinsic material properties, such as longitudinal speed of sound, from properties associated with linear dynamics, such as tension, of the structure. We demonstrate this approach through measurements of the longitudinal speed of sound in several NEMS devices composed of single crystal silicon along different crystal orientations. Good agreement with literature values is reported.

The third application of NEMS we discuss is mass spectrometry and inertial imaging. Currently, only doubly-clamped beams and cantilevers have been experimentally demonstrated for mass spectrometry. We extend the one-dimension model for mass spectrometry to a novel method for inertial imaging. We further extend the theory of mass spectrometry and inertial imaging to two dimensions by using a plate geometry. We show that the mode shape is critical in performing NEMS mass spectrometry and inertial imaging, and that the mode shapes in plates deviate from the ideal scenario with isotropic stress. We experiment with various non-ideal conditions to match non-ideal mode shape observed.

PUBLISHED CONTENT AND CONTRIBUTIONS

Hung, P., Feng, X. L., Roukes, M. L., *Graphene Nanoelectromechanical Devices and Systems*, Graphene Week 2010, Maryland, USA, April 19-23 (2010).

Hung, P., *et al.*, *In-Situ Longitudinal Speed of Sound and Stress Measurement in Nanoscale Single Crystals via Anharmonic Nonlinearity*. Submitted to Nano Letters, 2016.

P.H. participated in the conception of the project, designed the experiment, fabricated and measured the devices, analyzed the data, and participated in the writing of the manuscript.

Adapted with permission from Glish, G.L. and R.W. Vachet, *The basics of mass spectrometry in the twenty-first century*. Nat Rev Drug Discov, 2003. **2**(2): p. 140-150. Copyright 2016 Nature Publishing Group.

Reprinted with permission from Davidovikj, D., *et al.*, *Visualizing the Motion of Graphene Nanodrums*. Nano Letters, 2016. **16**(4): p. 2768-2773 Copyright 2016 American Chemical Society.

TABLE OF CONTENTS

Acknowledgements iii
Abstract vii
Published Content and Contributions ix
Table of Contents xi
List of Figures xiii
List of Tables xvii
Acronyms xix
Symbols xxiii
Chapter 1: Introduction and Overview 1
 1.1 Overview 2
 1.2 Nanoelectromechanical Systems (NEMS) 3
 1.3 Transistors and Switches 4
 1.4 Mass Spectrometry 7
 1.5 Bibliography 9
Chapter 2: NEMS Switches 13
 2.1 Motivation 13
 2.2 Operating Principle of NEMS Contact-Mode Switches 14
 2.3 State of the Art NEMS Switches Capabilities 18
 2.4 Mechanical and Electrical Properties 21
 2.5 Graphene NEMS Switch Fabrication Process 22
 2.6 Graphene NEMS Switch Experimental Setup 26
 2.7 Graphene NEMS Switch Measurement 28
 2.8 Optimization of Graphene 35
 2.9 NEMS Switches of Other Materials 44
 2.10 Summary 44
 2.11 Bibliography 51
Chapter 3: Speed of Sound Measurement via Anharmonic Nonlinearity in NEMS 57
 3.1 Motivation 57
 3.2 Beam Theory 59
 3.3 Doubly-clamped Beam Mode Shape 61
 3.4 Novel Representation of Resonant Frequency 65
 3.5 Experimental Determination of Resonant Frequency 69
 3.6 Novel Doubly-clamped Beam Fabrication 71

3.7 Experimental Setup for Measuring Anharmonic Nonlinearity 78
3.8 Measurement of Anharmonic Nonlinearity 79
3.9 Summary.. 85
3.10 Bibliography 85
Chapter 4: NEMS Mass Spectrometry and Inertial Imaging 89
4.1 Overview and Motivation 90
4.2 Operating Principal of NEMS-MS and 94
4.3 Devices and Analyte for 2D Inertial Imaging 103
4.4 Experimental Setup for 2D Inertial Imaging 110
4.5 Preliminary 2D NEMS-MS and NEMS-II Data 120
4.6 Ideal Mode Shape in 2D NEMS via Simulations and Calculations 133
4.7 Measured Mode Shape 138
4.8 Effect of Non-idealities on Mode Shape 146
4.9 Summary.. 154
4.10 Bibliography 159
Chapter 5: Conclusion and Perspectives 163
5.1 Summary.. 163
5.2 Perspectives and Future Topics... 165

LIST OF FIGURES

Figure 1-1 Diagram of a transistor. 5
Figure 1-2 Plot of semiconductor manufacturing process technology nodes. 6
Figure 2-1 Schematic of a three-terminal and two-terminal NEMS switch. 16
Figure 2-2 Raman spectrogram of the G and G' band for various thicknesses of graphene. ... 23
Figure 2-3 Fabrication process of graphene doubly-clamped switches. 25
Figure 2-4 Experimental setup for graphene device resistance measurement. 26
Figure 2-5 Frequency modulation mix down technique for measuring resonant frequency of the graphene device. 27
Figure 2-6 Resonant frequency plot as a function of gate voltage. 29
Figure 2-7 Scanning electron micrograph and performance of a graphene sample. 30
Figure 2-8 Multiple pull-in and pull-out cycles on a $900\ nm$ length graphene 31
Figure 2-9 Scanning electron micrograph of graphene switching devices 4 through 6. 34
Figure 2-10 CVD graphene transfer procedure. 37
Figure 2-11 The effect of PMMA quantity on quality of transferred graphene. 39
Figure 2-12 The effects of substrate preparation on the quality of transferred graphene. 41
Figure 2-13 Evolution of hole size as the graphene remains in acetone for various duration. . 42
Figure 2-14 Quality of graphene before and after transfer optimization. 43
Figure 2-15 AlN NEMS switch fabrication procedure. 46
Figure 2-16 Scanning electron micrograph and performance of AlN cantilever switches. 48
Figure 2-17 Scanning electron micrography of AlN doubly-clamped ladder switches. 49
Figure 3-1 The lowest three mode shapes of a doubly-clamped beam where the tension is negligible. 63
Figure 3-2 The lowest three mode shapes of a doubly-clamped beam where the bending moment is negligible. 64
Figure 3-3 Comparison of the effect of tension on the mode shape for the lowest two doubly-clamped beam modes. 65
Figure 3-4 Plot of the dimensionless functions $\alpha n \Omega n 2$ and $\alpha n - 1$ as a function of the dimensionless tension parameter β. 68
Figure 3-5 Phase of the resonator response to a sinusoidal driving force as a function of normalized frequency, $\omega/\omega 0$. 70
Figure 3-6 Phase of the resonator response to a sinusoidal driving force as a function of normalized frequency $\omega/\omega 0$. 71
Figure 3-7 Comparison of the traditional and new method of fabricating doubly-clamped beams. 72
Figure 3-8 Scanning electron microscopy images of silicon doubly-clamped beams as fabricated using traditional methods. 74
Figure 3-9 Novel process for fabricating doubly-clamped beams with no uncercuts. 75
Figure 3-10 Scanning electron micrographs of doubly-clamped silicon beams. 77
Figure 3-11 Acutation and detection scheme for the nonlinear beam measurement. 79
Figure 3-12 Mechanical response of the doubly-clamped silicon beam in the frequency domain as the actuation level increases from low to high 81

Figure 3-13 Plot of the frequency detuning as expressed by the square of the nonlinear response versus the oscillation amplitude. 82
Figure 3-14 Experimental longitudinal speeds of sound as a function of crystal orientation within the silicon 100 plane. 84
Figure 4-1 Time-of-flight measurement to perform mass spectrometry. 91
Figure 4-2 Magnetic sector mass analyzer. 92
Figure 4-3 Diagram of quadrupole used in traditional mass spectrometry. 93
Figure 4-4 A doubly-clamped beam resonator driven to its fundamental mode. 98
Figure 4-5 Scanning electron micrograph of a representative circular plate AlN device of $\sim 4.7\ \mu m$ in diameter. 104
Figure 4-6 Scanning electron micrograph of a representative square AlN plate device with $\sim 26\ \mu m$ sides. 106
Figure 4-7 Diagram of a representative square AlN plate device with $\sim 26\ \mu m$ sides. 107
Figure 4-8 Scanning electron micrograph of the effect of citrate buffer on the GNP solution. 109
Figure 4-9 Diagram showing desorption using MALDI and LIAD. 114
Figure 4-10 Actuation, detection, and deposition scheme in the MALDI setup. 116
Figure 4-11 Close up of the MALDI deposition system. 117
Figure 4-12 Photograph of our LIAD setup. 118
Figure 4-13 Schematic of the phase-locked-loop (PLL) employed to track three normal modes of the NEMS sensor (device under test). 120
Figure 4-14 Amplitude and phase responses of the first degenerate mode for the circular plate NEMS resonator. 122
Figure 4-15 Mass spectrometry data showing two mass loading events using a circular AlN plate with MALDI. 124
Figure 4-16 Optical image of the GNP on the MALDI slide before and after the mass deposition. 125
Figure 4-17 Verification of GNP deposition using scanning electron microscopy and energy dispersive x-ray spectroscopy (EDX). 126
Figure 4-18 Amplitude responses of the normal modes for the square NEMS resonator using piezoelectric actuation and detection. 128
Figure 4-19 Scanning electron micrograph of the AlN square plate after deposition with GNP. 129
Figure 4-20 Plots of the frequency downshifts of six simultaneous modes from five deposition events of $40\ nm$ GNP. 131
Figure 4-21 Plots of the frequency downshifts of six simultaneous modes from three deposition events of $80\ nm$ GNP. 132
Figure 4-22 Mode shapes for a circular plate from FEM. 136
Figure 4-23 Mode shapes for a circular plate from FEM. 137
Figure 4-24 Comparison of the lowest three measured and simulated mode shapes for a square plate resonator clamped at its edges. 140
Figure 4-25 Comparison of the ideal and measured normal mode frequencies for the first thirteen modes of a square plate with sides of $26\ \mu m$ long. 142
Figure 4-26 Frequency sweep of the device driven from the linear response regime to the nonlinear response regime. 143

Figure 4-27 Comparison of three lowest mode shapes obtained from measurements and simulations for ideal circular plates. 144
Figure 4-28 Comparison of the lowest eight measured and ideal circular membrane mode shapes using a graphene device. 145
Figure 4-29 Effect of actuation method and actuation power on the putative fundamental mode shape. 148
Figure 4-30 Effect of detection laser power on the mode shape of the lowest measured square plate mode. 150
Figure 4-31 FEM on the effect of anisotropic stress on mode shape. All six simulations have $300\ MPa$ of stress in the x direction. 152
Figure 4-32 Effect of reduction of stress on mode shape. 153
Figure 4-33 Effect of variation in optical cavity in the first mechanical mode. 155

LIST OF TABLES

Table 2-1 Comparison of the Young's modulus of NEMS switch materials. 21
Table 2-2 Summary of the graphene doubly-clamped devices and their switching performances. 33
Table 3-1 A table of the first six values of k which satisfy the boundary conditions for a doubly-clamped beam. 62
Table 3-2 A comparison of the measured speeds of sound along the 100 and 111 directions to the expected bulk material values. 85
Table 4-1 Number of normal modes needed for each mass moment for 1D and 2D inertial imaging. 103
Table 4-2 Mass and concentration of gold nanoparticles of various diameters as purchased from Sigma Aldrich, Inc. 108
Table 4-3 Summary of the frequency downshifts from the five $40\ nm$ diameter GNP deposition events. 131
Table 4-4 Summary of the frequency downshifts from the three $80\ nm$ diameter GNP deposition events. 132

ACRONYMS

1D	One-dimensional
2D	Two-dimensional
AFM	Atomic force microscopy
Al	Aluminum
AlN	Aluminum nitride
Au	Gold
BOE	Buffered oxide etch
CMOS	Complementary metal-oxide-semiconductor
CNT	Carbon nanotube
Cr	Chromium
CVD	Chemical vapor deposition
DC	Direct current
ECR	Electron cyclotron resonance plasma etching
EDX	Energy dispersive x-ray spectroscopy
$FeCl_3$	Iron (III) Chloride
FEM	Finite element method
FPGA	Field-programmable gate array
FWHM	Full width at half max
GNP	Gold nanoparticles
HeNe	Helium Neon
HOPG	Highly ordered pyrolytic graphite

IPA	Isopropyl alcohol
KOH	Potassium hydroxide
LIAD	Laser-induced acoustic desorption
MALDI	Matrix-assisted laser desorption/ionization
MEMS	Microelectromechanical systems
Mo	Molybdenum
MOS	Metal-oxide-semiconductor
MOSFET	Metal-oxide-semiconductor field-effect transistor
MS	Mass Spectrometry
Nd-YAG	Neodymium-doped yttrium aluminum garnet
NEMS	Nanoelectromechanical Systems
NEMS-II	Nanoelectromechanical systems inertial imaging
NEMS-MS	Nanoelectromechanical systems mass spectrometry
PLL	Phase-lock-loop
PMMA	Poly-methyl methacrylate
RF	Radio frequency
SEM	Scanning electron microscope
SHO	Simple harmonic oscillator
SiC	Silicon carbide
SOI	Silicon on insulator
SrF_2	Strontium fluoride
Ti	Titanium
TOF	Time-of-flight

UV	Ultraviolet

SYMBOLS

Symbol	Description
$\bar{\Omega}_n$	Normalized linear resonant frequency of the nth mode
$\langle z^p \rangle$	p^{th} mass moment of the analyte
$\bar{\omega}_n$	Dimensional linear frequency of the nth mode
Φ_{nm}	Mode shape of mode n, m of circular resonator
A_n	Amplitude of x_n under the (leading order) harmonic approximation
E_k	Young's modulus along (vector) crystallographic orientation k
F_0	Force on resonator
I_{DS}	Transistor drain-source current
I_n	Modified Bessel function of the first kind
I_{off}	Current flowing through NEMS switch in off-state
I_{on}	Current flowing through NEMS switch in on-state
J_n	Bessel function of the first kind
T_0	Tension in the non-deflected beam
V_{GS}	Transistor gate voltage
V_{PI}	NEMS switch pull-in voltage
V_{PO}	NEMS switch pull-out voltage
V_S	Voltage applied across NEMS switch
V_T	NEMS switch threshold voltage
g_0	NEMS switch vacuum air gap separation
k_{eff}	Effective spring constant

k_{nm}	Solutions of boundary value problem of circular resonator with clamped edges
m_{eff}	Effective mass
m_{geo}	Geometric mass
t_s	Switching time of NEMS switch
$v_{l,\hat{k}}$	Longitudinal speed of sound respective to the crystallographic orientation $\hat{k}$ in the (100) plane
$x_n(t)$	Time dependence of $X_n(z,t)$
$\bar{z}$	Mean position of analyte
$z_{particle}$	Location where particle has adsorbed to beam
α_n	Nonlinear coefficient
$\mu_{particle}(z)$	Linear mass density of the particle along the longitudinal direction of a doubly-clamped beam
ν_k	Longitudinal speed of sound
ρ_{xx}	Longitudinal sheet resistance
ω_0	Resonant frequency of doubly-clamped beam
ω_n	Nonlinear resonant frequency of the nth mode
$\phi_n(z)$	Normalized spatial dependence of the nth linear eigenmode of beam
h	Thickness of doubly-clamped beam
$\Delta\phi$	Change in phase
A	Effective area of capacitor used to model NEMS switch
E	Young's modulus
I	Areal moment of inertia
L	Length of doubly-clamped beam

Q	Quality factor
S	Swing per decade (voltage needed for a decade of change in current)
S	Cross sectional area of beam
T	Tension along the beam axis
$X(z,t)$	Deflection of an elastic beam normal to its axis
a	Slope of linear relation between ω_n^2 and A_n^2
b	Intercept of linear relation between ω_n^2 and A_n^2
f	Frequency
k	Transistor switch spring constant
m	Mass of resonator
t	Time
w	Width of doubly-clamped beam
z	Cartesian coordinate along the beam axis
β	Tension parameter
γ	Damping coefficient
θ	Angle between $\hat{k}$ and the $\langle 110 \rangle$ direction
ρ	Mass density
ω	Frequency of driving force
ϵ	Permittivity of free space

Chapter 1

INTRODUCTION AND OVERVIEW

This thesis focuses on three different applications of microelectromechanical systems (MEMS) and nanoelectromechanical systems (NEMS): mechanical switches, the use of anharmonic nonlinearity to measure *in-situ* device and material properties, and mass spectrometry. We will show how MEMS and NEMS are used as a new paradigm in these applications. In the first portion, we will discuss the challenges of scaling down the size of modern transistors and how the MEMS and NEMS switches we fabricated and measured resolve some of these challenges. In the second portion, we describe how to take advantage of mechanical anharmonic nonlinearity to determine device and material properties like tension and speed of sound in the material. In the last portion, we will describe how NEMS can improve mass spectrometry (MS), a technique to quantify and identify the amount of analyte in a solution, and inertial imaging, a technique to recover the high mass moments of the analyte. We will discuss the need for knowing the NEMS device mode shape in order to perform mass spectrometry and show that experimental mode shapes deviate from the ideal mode shapes and the sources that can cause these non-idealities.

1.1 Overview

In this chapter, we describe the history and the applications of MEMS and NEMS and provide the background and motivation for using NEMS switches as a new paradigm for scaling down transistors in size. Finally, we describe mass spectrometry and its many applications.

In Chapter 2, we discuss the operating principles of MEMS and NEMS switches and survey NEMS switches made of different materials and their state of the art capabilities. We then give an overview of graphene and how it is a suitable candidate for mechanical switches and discuss the fabrication process of these devices. Lastly, we demonstrate the performance of these graphene switches and preliminary data on the optimization of graphene switch performances.

In Chapter 3, we discuss a novel method of measuring the *in-situ* stress and speed of sound in a NEMS device by accessing the mechanical anharmonic nonlinearity via large displacement. We correct a previously attempted method of using anharmonic nonlinearity which does not take into consideration the effect of stress on the mode shape. Lastly, we demonstrate the measured value using this new methodology and show that the measured values match well with the bulk values from literature.

In Chapter 4, we begin our discussion of our last NEMS application of focus, mass spectrometry. We begin with providing an overview of NEMS mass

spectrometry (NEMS-MS). We demonstrate the shortcomings of one dimensional mass sensing and the need for actuating additional normal modes. In the process, we show the importance of knowing the mode shape of the NEMS device for mass spectrometry of analytes lacking symmetry. We also demonstrate that the measured mode shape deviates from the expected ideal mode shape from simulation and propose various non-ideal conditions which could account for the non-idealities.

1.2 Nanoelectromechanical Systems (NEMS)

Nanoelectromechanical systems (NEMS) [1] have advanced science and technology in a wide spectrum of fields, including nonlinear dynamics [2], sensors for force detection [3], mass spectrometry [4-6], inertial imaging [7], calorimetry [8], and charge sensing [9]. Due to their low power consumption, fast response time, large dynamic range, high quality factor, and low mass, NEMS can provide unprecedented measurement sensitivity. For optimized system functionalization and design, precise characterization of material properties at the nanoscale is essential.

Today, MEMS are ubiquitous in our daily lives. MEMS accelerometers are installed in cars to detect impacts so that air bags deploy to protect us. MEMS accelerometers are also installed on laptops so that if the laptop falls, the computer can detect the fall and turn off the hard drive in time to prevent damage upon impact. MEMS gyros are installed in most smart phones so that the orientation of the phone is detected to allow the display to be in the correct orientation. MEMS are also used as radio frequency switches which can be used in circuits as phase shifters, tunable

filters, and matching networks. Lastly, MEMS are used as oscillators and frequency sources because they have high resonant frequencies and good frequency stabilities, making them ideal clocks.

Compared to MEMS, NEMS are smaller so they are even lighter in weight, have smaller footprints when used for circuits, and it is easier to access their nonlinear behavior. These properties make NEMS sensors highly sensitive and interesting candidate systems for studying fundamental physics from quantum mechanics to nonlinear dynamics as we will discuss in Chapter 3.

1.3 Transistors and Switches

In this section, we provide a background of micro- and nano-mechanical switches and transistors. We will discuss some of the challenges as the size of transistors is downscaled. Lastly we will discuss using NEMS switches as a new paradigm to overcome some of the challenges of scaling down the size of transistors.

Transistors are used in every computer and most electronics today. As of 2009, about 10^{19} transistors have been shipped [10]. This translates to, on average, more than one billion transistors per person. Historically though, prior to the wide use of transistors, mechanical switches and logic gates were studied and, in fact, realized long before transistors and electronic logic gates [11]. And it was not until the past 50 years that transistors have replaced relays, mechanical logic, and vacuum tubes.

A metal-oxide-semiconductor (MOS) transistor has three major parts on or as part of the substrate: source, drain, and gate. For the transistor to be turned on, carriers (either electrons or holes) must flow from source to drain, forming a current. The gate is what determines the amount of carriers and current that flows through the transistor, varying the amount of current passing through based on the voltage applied to the gate. (Figure 1-1)

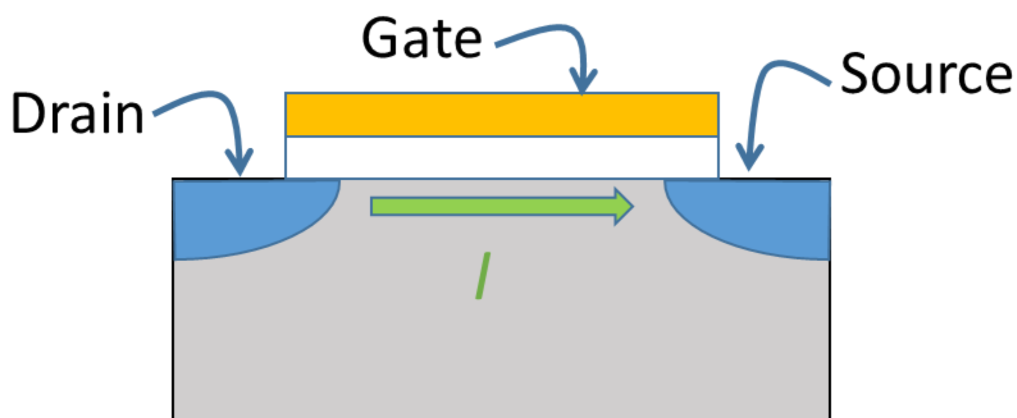

Figure 1-1 Diagram of a transistor. The drain and source (blue) have dopants of the opposite polarity compared to the substrate (gray). A small voltage is applied across the source and drain, but the amount of current that is able to flow from drain to source depends on the voltage applied to the gate.

Modern MOS technology has been following Moore's Law for device scaling for half a century for achieving density, speed, and power improvements. As the size of transistors decrease over time, the minimum feature size, or node, became one of the metrics for the scaling of devices. Figure 1-2 shows the scaling of devices over the past half century and the projection in the next few years.

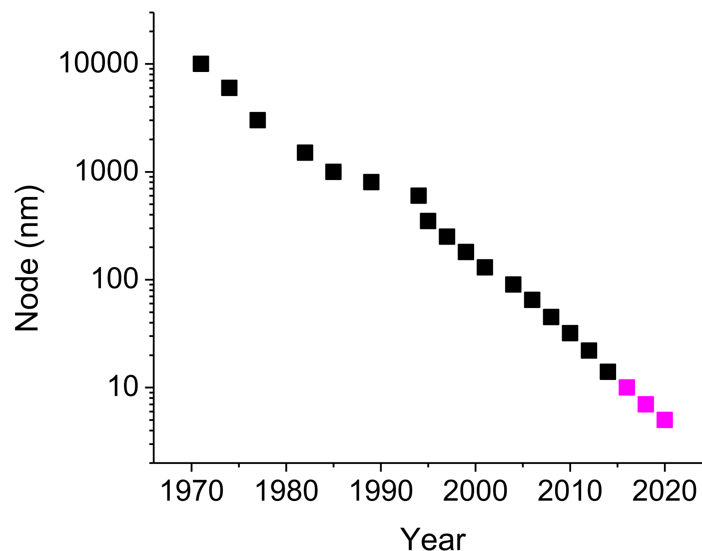

Figure 1-2 Plot of semiconductor manufacturing process technology nodes. The black dots are the years in which the nodes, or the gate length of transistors, was first manufactured. The magenta dots are projections of future nodes.

In the scaling of transistors, the distance between the various parts of the device as well as the voltage applied decrease. This causes leakage current in various parts of the transistor to increase. One of the major sources of leakage current is the subthreshold leakage, a non-zero current from source to drain even when the transistor is turned off. As the threshold voltage, the minimum voltage needed to turn on the transistor, decreases, the subthreshold leakage increases [12].

A new paradigm of using mechanical switches has been proposed as a solution to the subthreshold leakage issue. Since mechanical switches have to make physical contact for the current to flow, no current should be able to flow when the

switch is in the off state. This greatly reduces the off-state transistor power consumption and improves the on-state to off-state current ratio. Since the first MEMS switch was realized in 1979 [13], the advancements in MEMS and NEMS technology have made the realization of NEMS switches an interesting option that is worthy of consideration, among a member of post-complimentary MOS emerging logic devices, supplementing conventional transistors in various niche applications.

1.4 Mass Spectrometry

In the third section of this thesis, we will discuss NEMS-MS. In general, mass spectrometry is an analytical method in which the analyte is identified and quantified by using the mass-to-charge ratio of the analyte. Chapter 4 will provide some background into traditional mass spectrometry methods and provide details about NEMS-MS and NEMS inertial imaging (NEMS-II) in both one and two dimensions.

Mass spectrometry is used in a wide spectrum of fields: geology [14-16], environmental science [17-19], forensics analysis [20-22], and proteomics [23-25], the study of proteins in biological systems. In geology, mass spectrometry is used for carbon dating and measuring petroleum composition. In environmental science, mass spectrometry is used for testing water quality and food contamination. In clinical testing, mass spectrometry is often used to perform forensics analyses like confirming drug abuse and it is also used to detect disease biomarkers in newborns. In proteomics, mass spectrometry is used for determining protein structures, their functions, their folding patterns, and their interactions. Mass spectrometry can also

identify a protein from the mass of its peptide fragments and provide a method for monitoring enzyme reactions, chemical modifications, and even protein modifications.

1.5 Bibliography

1. Roukes, M., *Plenty of room indeed - There is plenty of room for practical innovation at the nanoscale. But first, scientists have to understand the unique physics that governs matter there.* Scientific American, 2001. **285**(3): p. 48-51.
2. Kacem, N., et al., *Nonlinear phenomena in nanomechanical resonators: mechanical behaviors and physical limitations.* Mechanics & Industry, 2010. **11**(06): p. 521-529.
3. Degen, C.L., et al., *Nanoscale magnetic resonance imaging.* Proceedings of the National Academy of Sciences, 2009. **106**(5): p. 1313-1317.
4. Chiu, H.-Y., et al., *Atomic-Scale Mass Sensing Using Carbon Nanotube Resonators.* Nano Letters, 2008. **8**(12): p. 4342-4346.
5. Naik, A.K., et al., *Towards single-molecule nanomechanical mass spectrometry.* Nat Nano, 2009. **4**(7): p. 445-450.
6. Chaste, J., et al., *A nanomechanical mass sensor with yoctogram resolution.* Nat Nano, 2012. **7**(5): p. 301-304.
7. Hanay, M.S., et al., *Inertial imaging with nanomechanical systems.* Nat Nano, 2015. **10**(4): p. 339-344.
8. Lee, W., et al., *High-sensitivity microfluidic calorimeters for biological and chemical applications.* Proceedings of the National Academy of Sciences of the United States of America, 2009. **106**(36): p. 15225-15230.
9. Cleland, A.N. and M.L. Roukes, *A nanometre-scale mechanical electrometer.* Nature, 1998. **392**(6672): p. 160-162.

10. Franssila, S., *Introduction to Microfabrication*. 2004: Wiley.

11. Price, D.S., *A History of Calculating Machines.* IEEE Micro, 1984. **4**(1): p. 22-52.

12. Yeo, K.S. and K. Roy, *Low Voltage, Low Power VLSI Subsystems*. 2005: McGraw-Hill.

13. Petersen, K.E., *Micromechanical Membrane Switches on Silicon.* IBM Journal of Research and Development, 1979. **23**(4): p. 376-385.

14. Potts, P.J., et al., *Microanalytical Methods in Mineralogy and GeochemistryInductively coupled plasma-mass spectrometric analysis of geological samples: A critical evaluation based on case studies.* Chemical Geology, 1990. **83**(1): p. 105-118.

15. Cohen, A.S. and F.G. Waters, *Separation of osmium from geological materials by solvent extraction for analysis by thermal ionisation mass spectrometry.* Analytica Chimica Acta, 1996. **332**(2–3): p. 269-275.

16. Eggins, S.M., et al., *A simple method for the precise determination of ≥ 40 trace elements in geological samples by ICPMS using enriched isotope internal standardisation.* Chemical Geology, 1997. **134**(4): p. 311-326.

17. Longbottom, J.E., et al., *Determination of Trace-Elements in Water by Inductively-Coupled Plasma-Mass Spectrometry - Collaborative Study.* Journal of Aoac International, 1994. **77**(4): p. 1004-1023.

18. Garbarino, J.R., *Methods of analysis by the U.S. Geological Survey National Water Quality Laboratory; determination of dissolved arsenic, boron,*

lithium, selenium, strontium, thallium, and vanadium using inductively coupled plasma-mass spectrometry, in *Open-File Report*. 1999.

19. Hirsch, R., et al., *Determination of antibiotics in different water compartments via liquid chromatography–electrospray tandem mass spectrometry.* Journal of Chromatography A, 1998. **815**(2): p. 213-223.

20. Nakahara, Y., et al., *Hair Analysis for Drug Abuse: I. Determination of Methamphetamine and Amphetamine in Hair by Stable Isotope Dilution Gas Chromatography/Mass Spectrometry Method.*

21. Dams, R., et al., *Urine drug testing for opioids, cocaine, and metabolites by direct injection liquid chromatography/tandem mass spectrometry.* Rapid Communications in Mass Spectrometry, 2003. **17**(14): p. 1665-1670.

22. Øiestad, E.L., U. Johansen, and A.S. Christophersen, *Drug Screening of Preserved Oral Fluid by Liquid Chromatography–Tandem Mass Spectrometry.* Clinical Chemistry, 2007. **53**(2): p. 300-309.

23. Aebersold, R. and M. Mann, *Mass spectrometry-based proteomics.* Nature, 2003. **422**(6928): p. 198-207.

24. Ong, S.-E. and M. Mann, *Mass spectrometry-based proteomics turns quantitative.* Nat Chem Biol, 2005. **1**(5): p. 252-262.

25. Bantscheff, M., et al., *Quantitative mass spectrometry in proteomics: a critical review.* Analytical and Bioanalytical Chemistry, 2007. **389**(4): p. 1017-1031.

Chapter 2

NEMS SWITCHES

In this chapter, we will discuss the operating principles of NEMS contact-mode switches, survey NEMS switches made of different materials, and examine their capabilities. We then give an overview of the properties of graphene and what makes it a great candidate for NEMS switches. We discuss the fabrication process for our prototype graphene NEMS switches and demonstrate their performance. Lastly, we describe our investigation on optimizing the graphene transfer process which can be used to enhance graphene NEMS switches.

2.1 Motivation

As described in Section 1.3 Transistors and Switches, the demand for continuous miniaturization of computing and memory technology has made power consumption a critical aspect of device engineering. In particular, even when the device is in the off state, there is leakage current between the drain and the source [1-3]. This leakage current scales up as the device is made smaller while maintaining the same voltage. While high-κ material has drastically reduced the tunneling current from the gate [4], the drain-source leakage current in the off state is still an issue. As devices continue to scale down, the on-current to off-current ratio, I_{on}/I_{off}, decreases exponentially. In a typical diffusion-dominated metal-oxide-

semiconductor field-effective transistor (MOSFET) at room temperature, the fundamental minimum of $60\ mV$ of change in gate voltage, V_{GS}, is needed per decade of increase of drain-source current, I_{DS}. Because of these issues, new paradigms offering promise for minimizing the leakage current are being explored so that further miniaturization of computer logic elements can continue.

2.2 Operating Principle of NEMS Contact-Mode Switches

NEMS switches offer an attractive solution to the leakage current issue caused by scaling down. Instead of a three-terminal device like a transistor, NEMS switches may have either two or three terminals. In a three-terminal device (Figure 2-1a), there is a separate source, drain, and gate, but for a simple two-terminal device (Figure 2-1b), the gate and the drain are one and the same. In the device off state, the source and drain terminals are physically and electrically separated by an air gap. These two terminals are often composed of one stationary part (e.g., the substrate or a side gate) and one moving part (e.g., a cantilever or a doubly-clamped beam).

To actuate the switch, a voltage potential is applied across its terminals. The minimum voltage needed to pull the moving part toward the stationary part is the pull-in voltage, V_{PI}. When the two parts touch, an ohmic contact is formed so that current flows from one terminal to the other, and the device is in the on state. Once the switch is closed, stiction due to van der Waals, Casimir forces, and other interfacial interactions can provide an additional force to keep the switch closed [5]. Because of stiction, the applied voltage has to be lowered by a non-zero amount to

the pull-out voltage, $V_{PO} < V_{PI}$, before the stiffness of the device (e.g., related to the flexural rigidity in a doubly-clamped beam or cantilever) causes the moving part to move back to its original position, returning the device to its off state. By taking advantage of this mechanical motion of the NEMS switch to completely disconnect source from drain with an air or vacuum gap, I_{on}/I_{off} is improved dramatically, as we will demonstrate later in this chapter.

In order to benchmark the performance of NEMS switches according those of transistors, the following four parameters are useful metrics: I_{on}/I_{off}, switch-on (pull-in) voltage, switching time, and the number of cycles before failure. We will describe each of these below.

As discussed in the previous section, the thermodynamic limit for I_{on}/I_{off} in a MOSFET transistor is at least $60\ mV$ of change in the V_{GS} for each decade of change of the current I_{DS}. Compared to MOSFET, NEMS switches have a clear advantage because the switch is always in one state until the voltage surpasses a threshold voltage, at which point, the switch is in the other state. The sudden, abrupt change from no contact to an ohmic contact between the two parts of the switch over an ideally zero change in voltage gives NEMS switches an ideal voltage swing in V_{GS} for each decade of change in drain current. This threshold voltage is called the switch-on voltage, and often is taken as the pull-in voltage at which the source is pulled to the drain (for three-terminal devices) or the source is pulled to contact the gate/drain (for two-terminal devices).

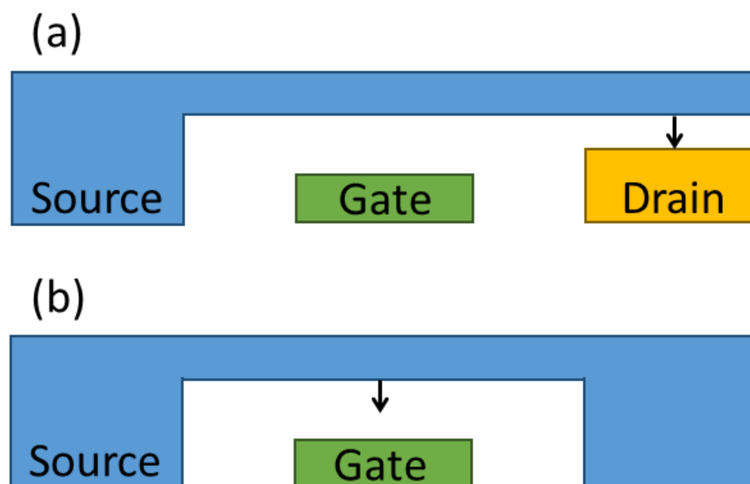

Figure 2-1 Schematic of a three-terminal and two-terminal NEMS switch. (a) In the three-terminal NEMS switch, a potential difference between the gate (green) and the source (blue) pulls the thinner part of the source toward the gate. Because the right side of the source is not fixed, it will be pull toward the drain (orange). When the source makes physical contact with the drain, current flows through and the switch is in the on state. (b) In the two-terminal NEMS switch, a potential difference between the gate (green) and the source (blue) again pulls the thinner part of the source toward the gate. When the source makes physical contact with the gate, current flows through and the switch is in the on state.

The switch-on voltage is the minimum DC gate voltage needed so that the two parts of the drain and source electrodes of switch come in physical contact. This is analogous to the threshold voltage, V_T, for a transistor. The switch-on voltage is an important metric for switches because it determines the overall power needed to operate the device. In general, the lower the voltage needed to actuate the switch, the lower the power consumption [6, 7]. In a two-terminal electrostatic switch, the electrostatic pull-in voltage is the switch-on voltage. The pull-in voltage is

determined by two forces: the capacitive force due to the applied potential and the restoring force due to rigidity. To simplify this calculation, the switch is modeled as a parallel plate capacitor with a vacuum air gap separation of g_0 when no potential is present. The minimum voltage needed for the two parts of the switch to contact, the pull-in voltage, is given by [8]

$$V_{PI} = \sqrt{\frac{8}{27}\frac{kg_0}{\epsilon A}}, \qquad \text{Eq. 2-1}$$

where k is the spring constant of the device, ϵ is the permittivity of free space or air, and A is the effective area of the capacitor. For a doubly-clamped beam with negligible tension, $k \propto hE/L^5 w$, where h is the thickness of the beam, E is the Young's modulus of the material, L is the length of the beam, and w is the width of the beam, Eq. 2-1 is rewritten as

$$V_{PI} = \sqrt{\frac{hEg_0}{\epsilon L^4}}, \qquad \text{Eq. 2-2}$$

In addition to the power consumption of the NEMS switch, the speed at which these switches are able to be turned on, or an equivalent measure, the inverse of the switching speed, the switching time, is also critical. This is analogous to the speed of a transistor with the fastest transistor realized to date operating at $765\ GHz$ at room temperature [9]. For a NEMS switch driven by capacitive actuation, if the applied voltage, V_S, is at least $2V_{PI}$, the switching time is given by [10]:

$$t_s = \frac{V_{PI}}{V_S \omega_0} \sqrt{\frac{27}{2}}, \quad \text{Eq. 2-3}$$

where $\omega_0 = \sqrt{k_{eff}/m_{eff}}$ is the resonant frequency of the device. Here k_{eff} is the effective spring constant and m_{eff} is the device effective mass. While the pull-in voltage is the minimum voltage needed to actuate the switch, higher voltages are often used to reduce the switching time as shown in Eq. 2-3. Similarly, a higher resonant device frequency corresponds to a lower switching time. Plugging Eq. 2-1 into Eq. 2-3 and assuming the switch is made of a doubly-clamped beam (e.g., $m_{eff} = 0.396\, \rho A h$ where ρ is the mass density and h is the beam thickness), the switching time is represented as:

$$t_s = \frac{0.793}{V_S} \sqrt{\frac{g_0 \rho h}{\epsilon}}. \quad \text{Eq. 2-4}$$

Lastly, the life-time of a switch is measured as the number of cycles the device is able to withstand before failure. In the next section, we will survey current state of the art NEMS switches.

2.3 State of the Art NEMS Switches Capabilities

The ideal NEMS switch would have an infinite or very high on-current to off-current ratio, low pull-in voltage, fast switching speed (short switching time), and high number of switching cycles before device failure. Unique properties of various materials are often exploited to optimize one of these metrics of NEMS switches. In

this section, we describe NEMS switches with some of the current state of the art pull-in voltage and switching times. Because NEMS switches can be switched from off-state to on-state by going from slightly below to slightly above the pull-in voltage, the minimum voltage swing to turn on a NEMS switch is always going to outperform the $60\ mV/dec$ swing/slope of transistors, and thus will not be discussed in this section.

In order to achieve a low pull-in voltage, piezoelectric actuation provides an interesting mechanism for use due to promise for low voltage operation. Instead of using electrostatic actuation by applying a voltage across both the moving part and the stationary part of the switch, the voltage is applied across a piezoelectric element. The applied voltage causes the material to expand or contract, and using asymmetric expansion and contraction, a piezoelectric doubly-clamped beam or cantilever deflects until it comes into contact with an electrode, thus closing the circuit. Using aluminum nitride (AlN), Piazza *et al.* have made doubly-clamped beams and cantilever NEMS switches with 520 mV as the minimum actuation voltage [11-13]. While the actuation voltage is small, the device has a large footprint of $\sim 60\mu m^2$, which is comparable to many piezoelectric NEMS switches demonstrated to date.

Compared to transistors, most MEMS switches demonstrated to date have tended to be slower, with switching times typically on the order of microseconds [14]. By contrast, Feng *et al.* has made in-plane NEMS switches using silicon on insulator (SOI) cantilevers with resonant frequencies between $1-10\ MHz$ or

switching speeds between $10 - 100\ ns$ [15-17]. One of the notable features of these Feng cantilever switches is the very small air gap between various parts of the switch: $50 - 100\ nm$ between the cantilever and the gate and $20 - 40\ nm$ between the source and drain. The small vacuum or air gap, as seen in Eq. 2-4, allows for faster switching times.

In addition to using AlN and SOI as materials for NEMS switches, several other materials are used because of their unique properties, e.g., silicon carbide (SiC) [18], single- and multi-wall carbon nanotube (CNT) [19, 20], and graphene [21]. Silicon carbide's advantage is its robustness to harsh conditions like high temperatures. Carbon-based material like CNT and graphene have been of interest given their light weight and stiffness. The attributes endow CNT and graphene based switches with faster switching times and lower pull-in voltages.

When considering only the pull-in voltage and the switching time, Eq. 2-2 and Eq. 2-4 are used to determine material properties ideal for fast switches with low power consumption. In order to minimize the pull-in voltage for a doubly-clamped beam NEMS switch with an air gap, the spring constant and air gap distance should be minimized while the area should be maximized. In order to minimize the switching time of this switch for a given applied voltage, a material with low mass density and architectures emphasizing thin movable elements are preferable.

In the next section, we will discuss graphene which has properties that may make it an ideal material for NEMS switches.

2.4 Mechanical and Electrical Properties of Graphene

Graphene, which is a single layer of carbon atoms arranged in a hexagonal structure, has many interesting properties that make it an attractive candidate for nanoelectromechanical switches. For example, as a single atomic layer, graphene can be defect-free [22]. Another advantage of graphene is that its mechanical strength is 200 times that of steel; this offers interesting prospects for building robust moving parts for a nanoelectromechanical switches. While graphene has a very high Young's modulus of $1\,TPa$ [23], the thinness of the material still allows for a low pull-in voltage (Eq. 2-2). Table 2-1 compares the Young's moduli of some common materials for making MEMS/NEMS switches [23-29].

Material	Young's Modulus (GPa)
Carbyne	32700
Graphene	1050
Single Wall Carbon Nanotube	1000
Silicon Carbide	350 – 450
Molybdenum	330
Silicon	130 – 188

Table 2-1 Comparison of the Young's modulus of NEMS switch materials.

In addition, graphene has a low longitudinal sheet resistance; $\rho_{xx} = 1125\,\Omega/\text{square}$; this can translate into high on-state conductance [30]. In the

following sections, we will discuss the graphene and other NEMS switches that we have fabricated and tested.

2.5 Graphene NEMS Switch Fabrication Process

In our first generation of graphene NEMS switches, graphene from highly ordered pyrolytic graphite (HOPG) was exfoliated onto a silicon wafer with a $285\ nm$ thermally grown silicon dioxide layer. HOPG is defined as "artificially grown graphite with an almost perfect alignment perpendicular to the carbon planes" [31]. It has many layers of graphene stacked on top of one another. The $285\ nm$ thick silicon dioxide was used because it is optimal for having the greatest contrast for observing graphene under an optical microscope [32].

Graphene was exfoliated using the Scotch® tape method. A small flake of HOPG was placed on a piece of Scotch® tape and the tape was folded on itself so that both sides of the HOPG were covered by different parts of the tape. After the tape was firmly pressed, the tape was peeled apart so that there is HOPG on both sides of the tape, reducing the number of layers of graphite at each location. This folding process was repeated many times until the HOPG on the tape was translucent. The tape was then pressed on the $285\ nm$ silicon dioxide substrate to transfer some of the HOPG to the substrate. The substrate was then inspected under the optical microscope to identify single-layer graphene to a few-layer graphene.

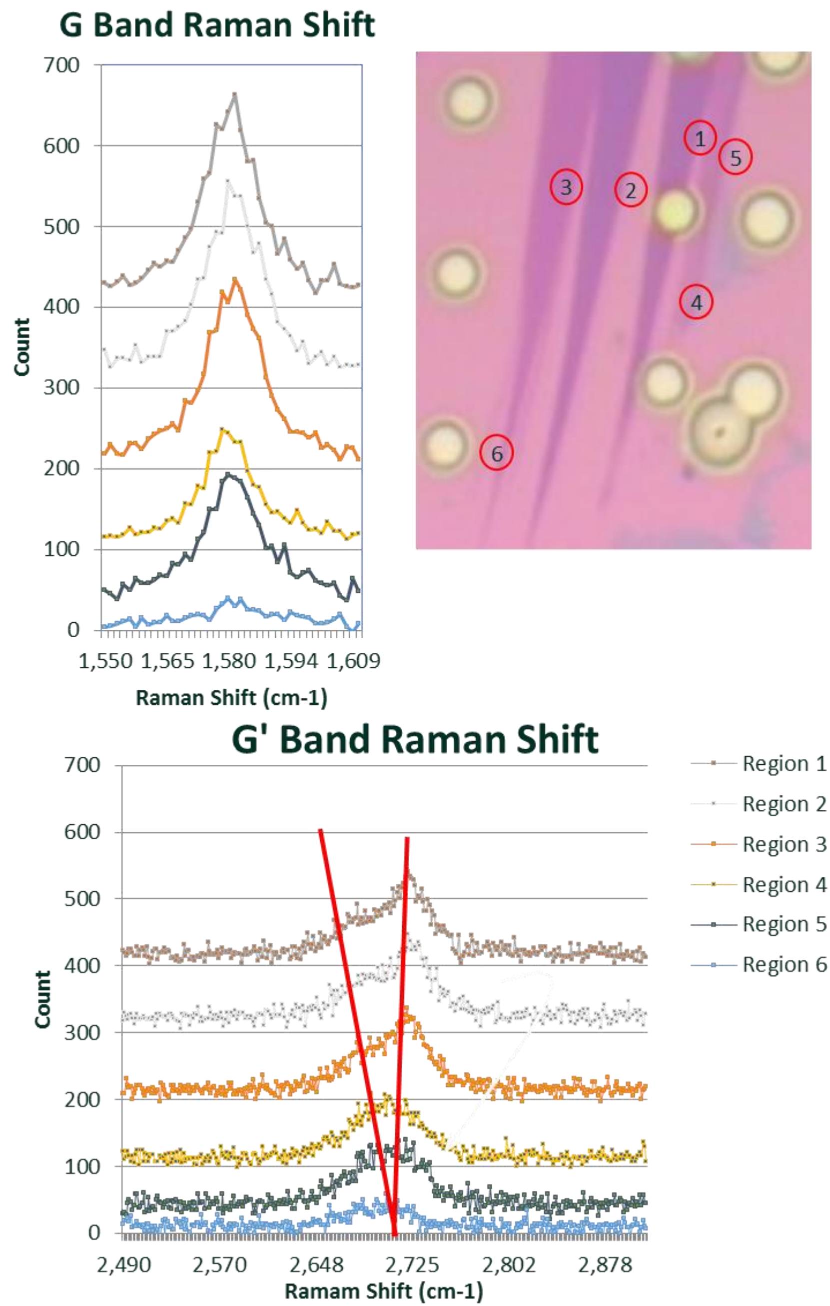

Figure 2-2 Raman spectrogram of the G and G' band for various thicknesses of graphene. The upper right is an optical image of the graphene sample of different thicknesses. The thickness is verified using AFM. Region 1 is single layer. Region 2 and 3 are bilayers. Region 4 has 4 layers. Region 5 and 6 have 7 to 8 layers.

In order to verify that the graphene is single-layer, Raman spectroscopy was performed with a $514\ nm$ laser. Based on the full width at half max (FWHM) and the relative amplitude of the various peaks on the Raman spectrograph, the number of layers of graphene was determined. Figure 2-2 shows the Raman spectrograms of various thicknesses of graphene, subsequently confirmed by atomic force microscopy (AFM). In verifying the number of layers of graphene, there are two key features: the G peak around $1580\ cm^{-1}$ and the G' peak around $2700\ cm^{-1}$ [33]. For one or two layers of graphene, the G' peak has a higher amplitude than the G peak. In particular, for a single-layer graphene, the intensity of the G' peak is about twice that of the G peak. In addition to the relative peak intensities, the FWHM of the G' peak goes from $\sim 30\ cm^{-1}$ for a single graphene layer to $\sim 50\ cm^{-1}$.

Once the graphene sample had been verified to be single-layer or bi-layer, alignment markers were patterned onto the chip using electron beam lithography. A bilayer of Poly-methyl methacrylate (PMMA) is used as the e-beam resist. 495PMMA A4 is spun at $4000\ RPM$ for 1 minute and baked for 5 minutes, followed by the same procedure with 950PMMA A2. After developing the resist and finding the location of the graphene with respect to the alignment markers, the electrodes were designed and patterned using e-beam lithography again. After developing the resist, $5\ nm$ chromium (Cr)/$300\ nm$ gold (Au) was evaporated using a thermal evaporator and was lifted off in an acetone bath overnight. Lastly, the device was submerged in 10:1 buffered oxide etch for 3 minutes to release the device, submerged

in de-ionized water, followed with filtered isopropyl alcohol (IPA), and then dried via critical point drying. (Figure 2-3)

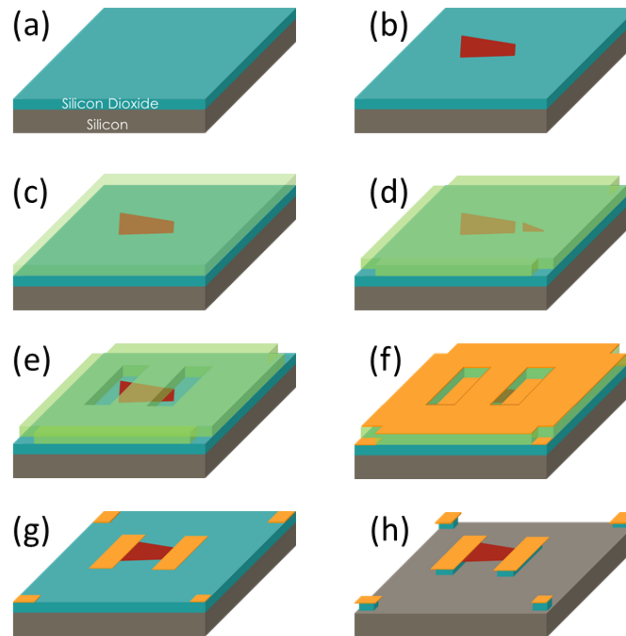

Figure 2-3 Fabrication process of graphene doubly-clamped switches. (a) Device fabrication is done on a silicon substrate with 285 nm silicon dioxide. (b) Graphene is exfoliated onto the substrate using the Scotch® tape method. The thickness of the graphene sample is then measured using Raman spectroscopy. (c) A PMMA bilayer is spun on the substrate, covering the graphene. (d) Alignment markers are patterned using electron beam lithography. (e) After locating the graphene with respect to the alignment markers, electrodes are designed and patterned using electron beam lithography. (f) 150 nm of gold is thermally evaporated onto the sample. (g) The sample is submerged in buffered oxide etch for 3 minutes. (h) The buffered oxide etch is then replaced with water, then isopropyl alcohol, and the sample is dried in the critical point dryer.

2.6 Graphene NEMS Switch Experimental Setup

In order to measure the performance of these graphene NEMS switches, they were placed in the chamber of a Lakeshore PTXX probe station. All measurements were performed at room temperature and at a pressure of $10^{-6}\ torr$. Resistance of each device was measured using an SR 830 lock-in amplifier with radio frequency (RF) of $38.25\ kHz$.

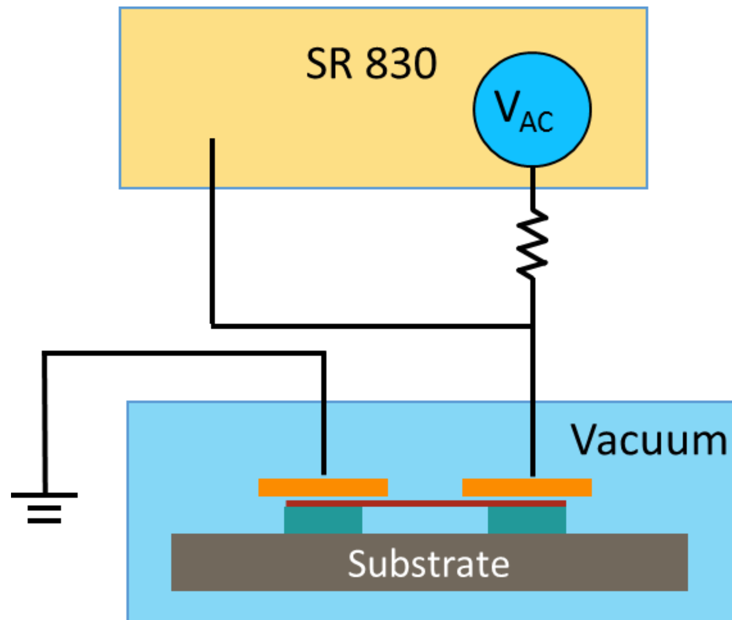

Figure 2-4 Experimental setup for graphene device resistance measurement. A resistance of $100\ k\Omega$ and V_{AC} at $38.25\ kHz$ was used while the device is in a vacuum $< 10^{-6}\ torr$.

The device resonance was also measured using a frequency modulation scheme [34]. An RF voltage at frequency $f + \Delta f$ was applied to the drain of the device while a DC and an RF voltage at f was applied to the substrate. The two RF

signals were mixed using an external commercial mixer (Mini-circuit ZFM-2+) and used as the reference for the SR 830 lock-in amplifier to detect the signal from the source of the device. (Figure 2-5)

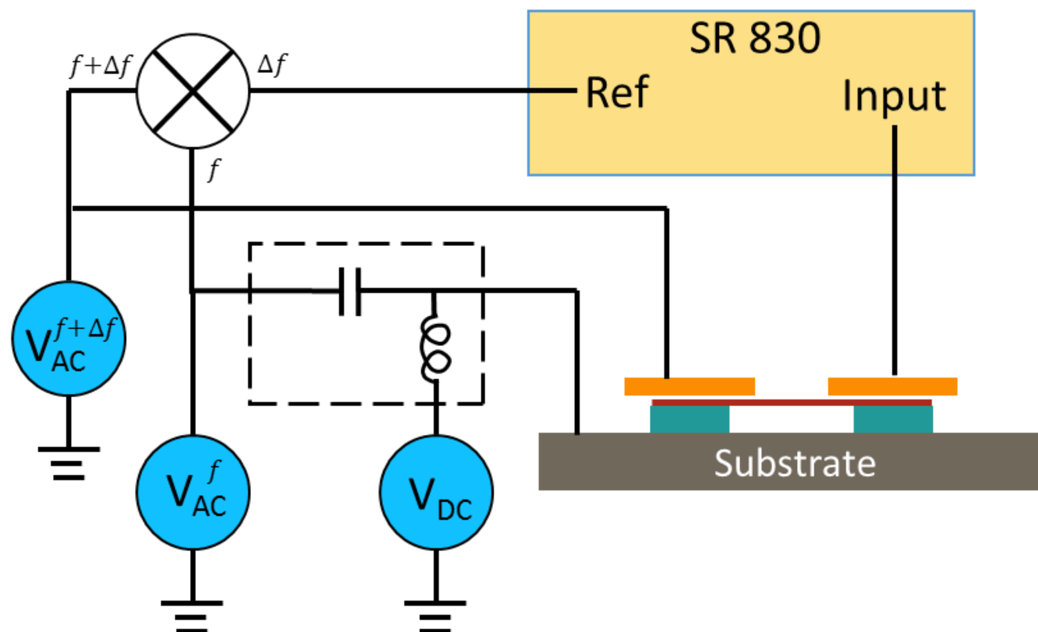

Figure 2-5 Frequency modulation mix down technique for measuring resonant frequency of the graphene device. An RF signal of frequency $f + \Delta f$ was applied to the source of the device while a DC signal with an RF signal at frequency f was applied to the gate of the device. A commercial mixer was used to mix down the sources and the mixed down frequency at Δf was used as the reference for the SR 830 lock-in amplifier. The signal from the drain was fed into the SR 830 for measurement.

After characterizing the devices, an HP 4145B semiconductor analyzer was used to measure the switching performance of the devices. The source of the device was grounded while the gate was swept using the HP 4145B source/measure unit

(SMU) starting from $0\,V$. The gate voltage upper sweep range was increased typically from $1\,V$, $2\,V$, $5V$, $10\,V$, then $20\,V$ to ensure the voltage applied was not too high such that it damages the device.

2.7 Graphene NEMS Switch Measurement

We evaluated the performance of seven devices of various dimensions using the techniques discussed in the above sections. This section summarizes the results of this study along with a tale of the devices' measured characteristics.

Device resonant frequency was measured as a function of DC voltage applied to the gate. Figure 2-6 shows a typical result. The device used for this measurement was $3.4\,\mu m$ long and $2.0\,\mu m$ wide. As the potential across the device and the substrate increases, electrostatic force also increases, causing the frequency to rise. The lowest frequency does not correspond to a gate voltage of $0\,V$ because residual charges on the graphene from the fabrication process require a nonzero gate voltage to balance their effect. The discontinuities at $17\,MHz$ most likely result from the resonance of the gold ledge used for clamping the graphene. This resonant frequency does not tune with the gate voltage, which is consistent with the expected behavior.

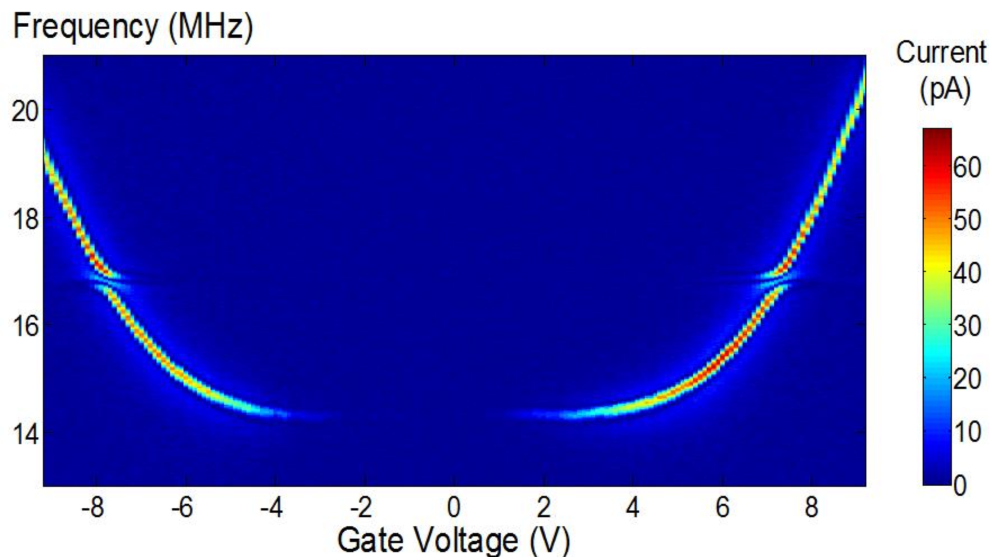

Figure 2-6 Resonant frequency plot as a function of gate voltage. The frequency increases as a function of gate tuning because the potential applied across the device and the substrate induces additional tension in the device, increasing the resonant frequency. The discontinuities at $17\,MHz$ most likely come from the resonance of the gold ledge used for clamping the graphene.

Figure 2-7 and Figure 2-8 show the measured voltage and current responses of two graphene NEMS switches. In our first bilayer graphene device of length $\sim 2.8\,\mu m$ and width $\sim 1\,\mu m$ (Figure 2-7), we see the typical behavior with $V_{PI} = 4\,V$ and $V_{PO} = 2\,V$. $I_{on}/I_{off} > 100$ and it took less than $10\,mV$of voltage change to increase the current by a decade (compared to the $60\,mV$ minimum for a decade in current for a transistor).

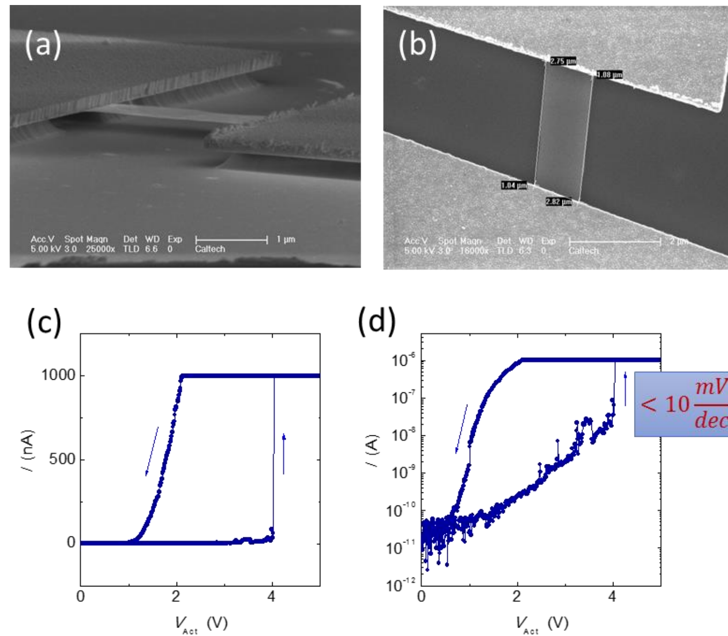

Figure 2-7 Scanning electron micrograph and performance of a graphene sample. (a) Scanning electron micrograph image of a suspended, doubly-clamped graphene ribbon/membrane structure that can enable a two-terminal vertical electrostatic switch (via coupling to the conductive Si substrate) and/or an out-of-plane graphene membrane resonator. (b) Top-view SEM image of the device showing the measured in-plane dimensions. (c) Two-terminal NEMS switching test data showing an abrupt switching at V_{on}~4V, with a very small swing, a high on/off ratio, and a ~2V hysteresis. (d) Same data as shown in panel (c) but with measured current in logarithmic scale.

In our second device, (Figure 2-8) the single layer graphene is shorter with length 900 nm, but it is not as well clamped. We show the response of the device over multiple pull-in and pull-out cycles. In this device, the pull-in voltage increased over time, most likely due to the poor clamping and deformation of the device from each pull-in cycle. After 18 cycles of pull-in and pull-out, the device finally failed.

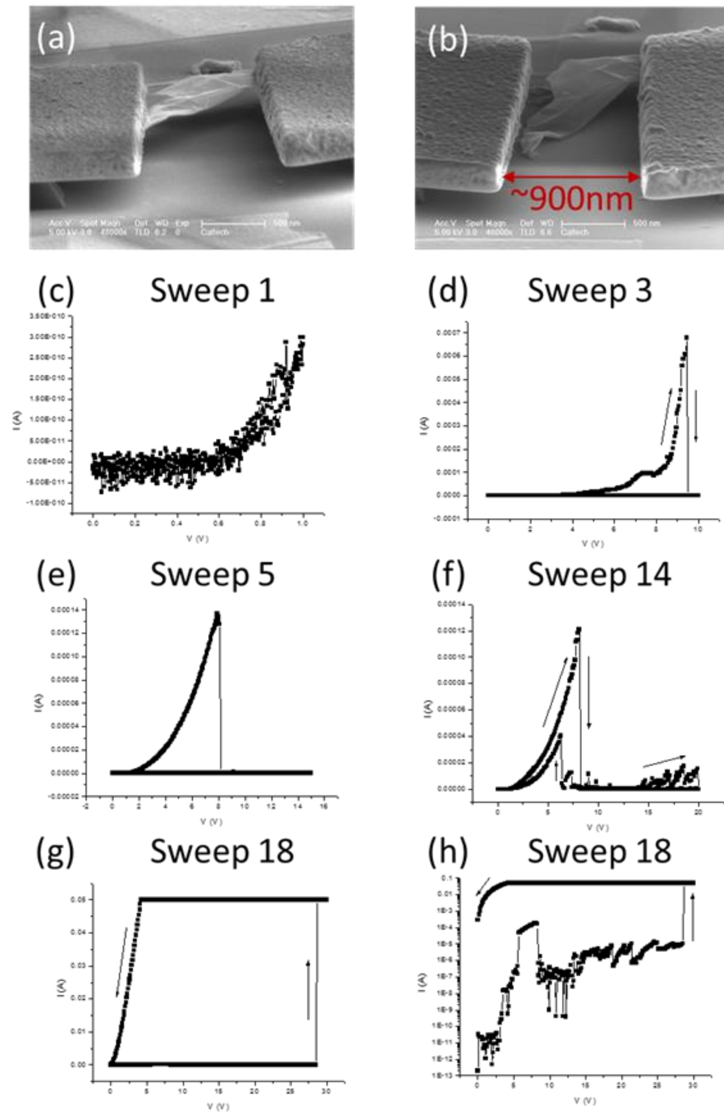

Figure 2-8 Multiple pull-in and pull-out cycles on a 900 nm length graphene NEMS switch. The pull-in voltage increased over time until failure after 18 cycles.

A total of seven devices, similar to those presented above, were successfully fabricated and measured. A summary of their performances is listed below in Table 2-2 with the devices mentioned above being device 1 and 2 in the table. All devices

were between one and four graphene layers thick. The swing per decade or the change in voltage needed for a decade of change in current, S, for all devices is less than 10 $mV/decade$. While the HP 4145B has a minimum voltage step size limit of 1 mV, most of our measurements were performed with a voltage step size of 20 mV to 50 mV. In addition, we limited the on-state current compliance to between 1 μA and 100 mA depending on the response of the device. The current limit minimizes excessive heating to the device which may alter the device performance. By performing the measurement with smaller voltage step sizes, a more precise swing per decade can be measured. In addition, while the switching time was not measured directly, we are able to deduce the switching time to be $< 100\ ns$ from the measured resonant frequencies of the devices using Eq. 2-3.

ID	Thickness $t\ (nm)$ [# layers]	2D-Dimensions $L_1, L_2, w_1, w_2\ (\mu m)$	Switch-On Voltage $V_{on}\ (V)$	Swing/Slope $S\ (mV/dec)$	I_{on}/I_{off}
1	0.68 [2]	2.75, 2.82, 1.08, 1.04	4.02	< 10	$\frac{10^{-6}}{1.03 \times 10^{-11}} = 9.7 \times 10^4$
2	0.34 [1]	0.9, 0.9, 2.2, 2.3	28.7	< 10	$\frac{0.05}{2 \times 10^{-13}} = 2.5 \times 10^{11}$
3	0.68 [2]	3.4, 3.4, 2.33, 1.4	2.4	< 10	$\frac{0.1}{1.13 \times 10^{-5}} = 2.36 \times 10^6$
4-6	0.68 [2]	1.7, 1.7, 1.0, 1.0 1.8, 1.8, 1.25, 1.25 1.9, 1.9, 1.75, 1.75	3.6	< 10	$\frac{0.1}{4.22 \times 10^{-8}} = 8.85 \times 10^3$
7	1.36 [4]	5.75, 5.7, 2.4, 2.6	23.6	< 10	$\frac{0.05}{9 \times 10^{-10}} = 5.6 \times 10^7$

Table 2-2 Summary of the graphene doubly-clamped devices and their switching performances. All devices were between 1 and 4 layers of graphene. The swing/slope are all below 10 mV/dec and these values are limited by the step size and the current limit set during the measurement. Similarly, I_{on}/I_{off} are limited by the maximum current set by the measurement and thus these values are expected to be orders of magnitude higher than reported.

A set of devices worth noting are devices 4 through 6 which is composed of three pieces of graphene sharing the same electrodes. The novelty of having graphene pieces of various sizes sharing an electrode is that they each have a slightly different pull-in voltage. By actuating only the graphene device with the smallest pull-in

voltage each time, even after this particular piece of graphene fails after multiple pull-in and pull-out cycles, the remaining graphene pieces can continue to make electrical connections by applying a higher voltage. This is a possibility in improving the longevity of the devices.

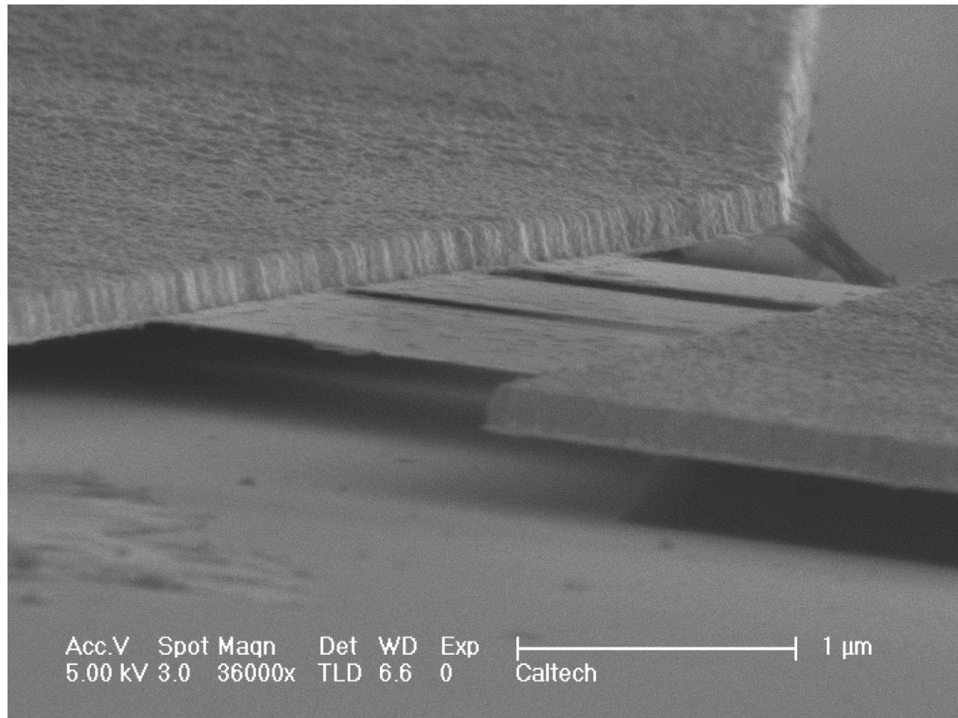

Figure 2-9 Scanning electron micrograph of graphene switching devices 4 through 6. This set of devices is composed of three pieces of graphene with slightly difference dimensions. Due to the different dimensions, each piece of graphene has a slightly different pull-in voltage. This allows the switch to continue to work even after one of the pieces of graphene fails due to testing over time.

In this section, we showed the results of our graphene NEMS switches. Compared to traditional transistors, our switches had a much smaller swing voltage,

$< 10\, mV/dec$. We also demonstrated that our devices have a switching time typically $< 100\, ns$. While these prototype devices are still not as fast as the state of the art transistor and cannot last 10^7 cycles like many current transistors, through engineering and optimization of the design and fabrication process, the performances of graphene NEMS switches will improve. The current method using the Scotch® tape method and HOPG requires each device geometry and location to change based on the graphene piece available. This prevents large scale engineering and testing of graphene device geometry and other parameters. In the next section, we will experiment with graphene grown on a copper foil to achieve large graphene areal coverage.

2.8 Optimization of Graphene for NEMS Switches

Our preliminary results from tests of graphene NEMS switches proved promising, so we conducted further experiments to optimize various aspects of their design and fabrication. This section discusses some of those follow-on investigations using chemical vapor deposition (CVD) graphene grown on copper foil instead of exfoliated graphene. While exfoliating graphene is simple to perform, the process is unreliable in depositing single layer graphene, size of samples are small, and the process is time consuming. Exfoliated graphene is unscalable for technological applications. CVD graphene, on the other hand, is a promising candidate for producing consistent single layer to arbitrary shapes and sizes.

We begin with our typical CVD graphene transfer process. For all of our experiments in this section, commercial CVD graphene grown on copper foil from Graphene Supermarket was used. Both sides of the copper foil have CVD graphene because of the growth method. For each sample, we started with a small piece, $\sim 1\ cm\ \times 1\ cm$, of CVD graphene on copper and applied a drop of 950PMMA C8 to cover one side of the CVD graphene. The PMMA/CVD graphene was then placed in a beaker of $1M$ iron (III) chloride ($FeCl_3$) for 30 minutes. The PMMA/CVD graphene flows due to the surface tension of water and the hydrophobic nature of PMMA. The $FeCl_3$ etched the copper causing graphene on the bottom side of the copper foil to sink to the bottom of the beaker. After 30 minutes, the PMMA/graphene sample then underwent successive de-ionized water baths to rinse away metal particles left from the etch. The sample was then collected on a clean, $285\ nm$ silicon dioxide on silicon substrate with alignment markers pre-patterned. The sample was then dried in the air for 4 hours. Another drop of 950PMMA C8 was placed on the graphene to reflow the preexisting PMMA to release any tension built up during the transfer process. The sample was then heated to $60°\mathrm{C}$ for 30 minutes. Finally, the PMMA was removed in an acetone bath.

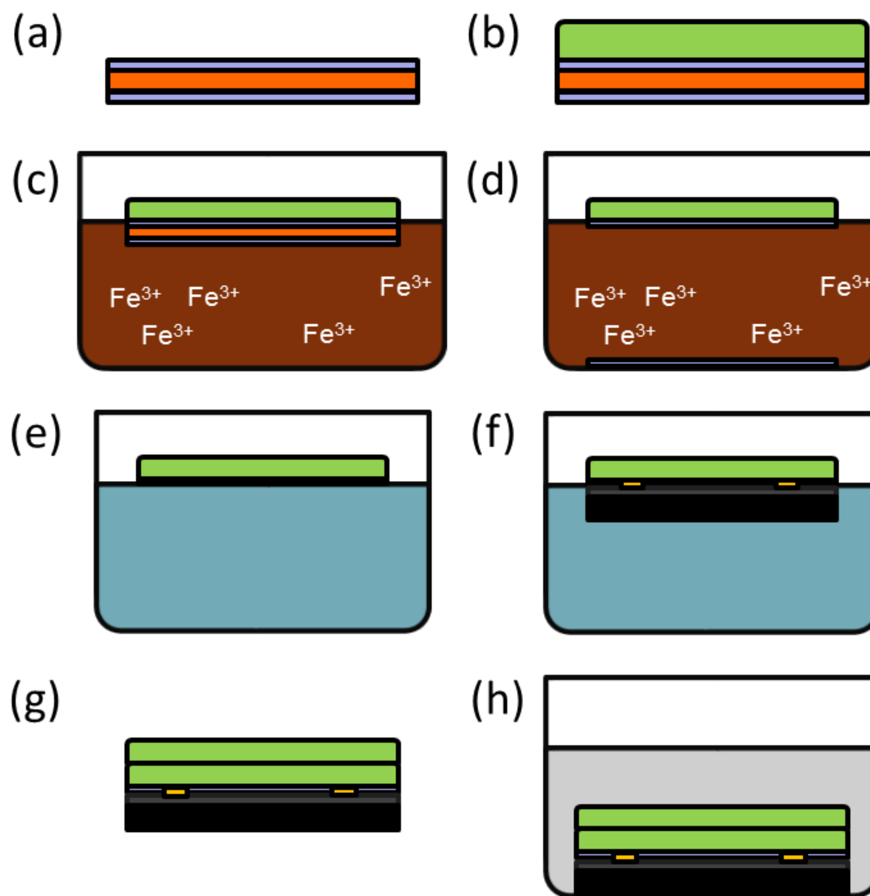

Figure 2-10 CVD graphene transfer procedure. (a) We began with commercially purchased CVD graphene. (b) 950PMMA C8 was applied to the CVD graphene. (c) The PMMA/graphene was etched in a $1M$ $FeCl_3$ solution. (d) With the copper etched, the bottom graphene layer sinks to the bottom of the beaker. (e) The $FeCl_3$ was then replaced with de-ionized water three times to remove leftover metal and etchant. (f) The PMMA/graphene was lifted from the water with a silicon/silicon-dioxide chip with pre-patterned alignment markers. (g) Another drop of PMMA was applied to the graphene to reflow the PMMA. Then the sample is heated for 30 minutes. (h) The PMMA was removed in an acetone bath.

The CVD transfer process resulted in continuous graphene for the most part but there are periodic tears in the graphene and residual PMMA in the resulting graphene. Every device fabricated using this transferred graphene still has to be designed individually depending on the location and size of the continuous graphene. We experimented with the following steps to minimize the number and size of the tears and the amount of residual PMMA: 1) the amount of PMMA applied in the first step, 2) functionalization of the silicon dioxide surface of the substrate, and 3) the duration of leaving the sample in acetone to remove the PMMA.

Figure 2-11 shows the results from using various amounts of PMMA to hold onto the top graphene layer while etching the copper foil. When a drop of PMMA was put on a piece $\sim 1\ cm\ \times 1\ cm$ of CVD graphene, large areas of graphene, $\sim 10\ \mu m\ \times 10\ \mu m$ or larger, rolled up. When excess PMMA was removed prior to the transfer process with a piece of Texwipe®, the transferred graphene is practically holes-free with the exception of a few small tears on the order of $\sim 2\ \mu m\ \times 2\ \mu m$. When these samples were placed in the etchant, the sample with the excess PMMA tends to curl upward like a bowl, most likely due to the surface tension, while the sample without the excess PMMA remains flat to the surface of the water. The extra stress from the excess PMMA is likely the cause of the holes in the graphene.

In order to be more precise than simply wiping the excess PMMA off, a spinner was used to spin the excess PMMA off at $500\ RPM$ and at $4000\ RPM$. In both of these cases, many micro-tears on the order of $\sim 1\ \mu m$ to $\sim 5\ \mu m$ were evenly

distributed across the entire sheet of graphene. In the case where the spin speed is higher, the micro-tears were bigger. The results here were representative of the three repeated trials we performed.

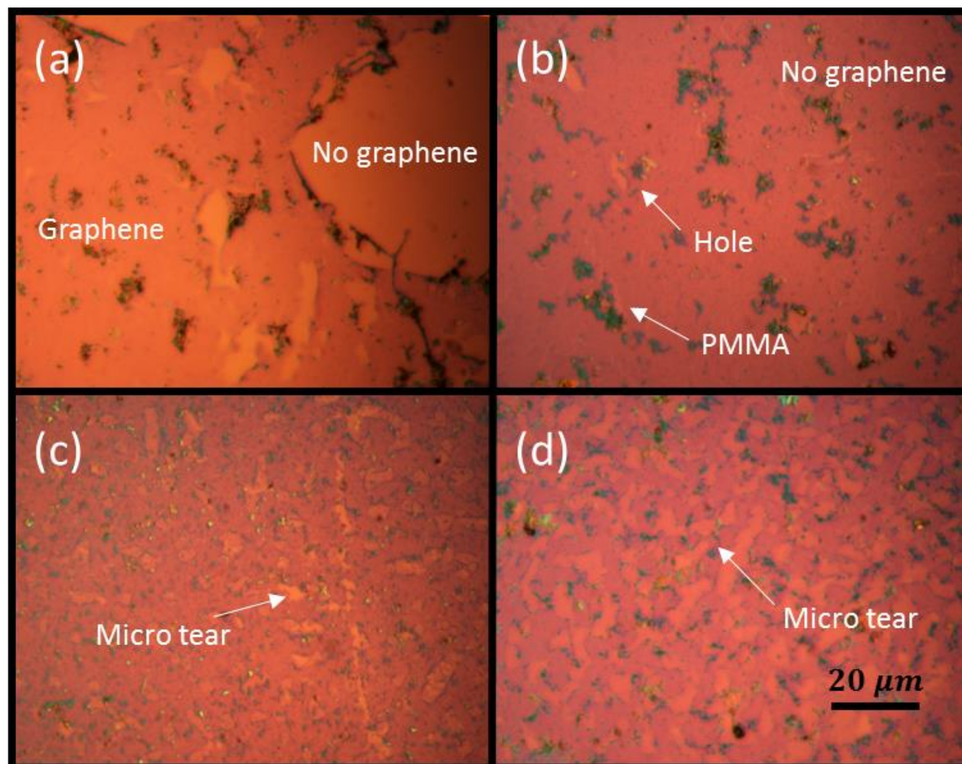

Figure 2-11 The effect of PMMA quantity on quality of transferred graphene. (a) A full drop of 950PMMA C8 is applied to a piece of CVD graphene $1\ cm \times 1\ cm$ and resulted in large holes. (b) Excess PMMA was removed with a Texwipe® and the transferred graphene is relatively holes free. (c) Excess PMMA was removed by spinning at $500\ RPM$ and transferred graphene has mirco-tears distributed throughout. (d) Excess PMMA was removed by spinning at $4000\ RPM$ and larger micro-tears resulted throughout.

Figure 2-12 shows the effects of the substrate preparation on the quality of transferred graphene. During the transfer process, after the copper foil was etched away from the CVD graphene and triple rinsed with de-ionized water, a substrate was used to lift the graphene out of the water. The substrate used is a silicon chip with a layer of $285\ nm$ silicon dioxide and $100\ nm$ gold alignment markers pre-patterned. Through trial and error, we discovered that by dipping the substrate into diluted solution of 1 part 10:1 buffered oxide etch (BOE) to 50 parts de-ionized water for 1 or 2 seconds prevents long tears in the transferred graphene. We note that the transfer of graphene must be performed soon after the diluted BOE treatment. Attempts at dipping all the substrate in the buffered oxide etch a few days in advance of transferring the graphene onto them did not prevent the long tears. We hypothesize that this is due to new hydrogen bonds being formed from the quick diluted BOE dip, which allowed the graphene to adhere better to the substrate for subsequent steps of the transfer process.

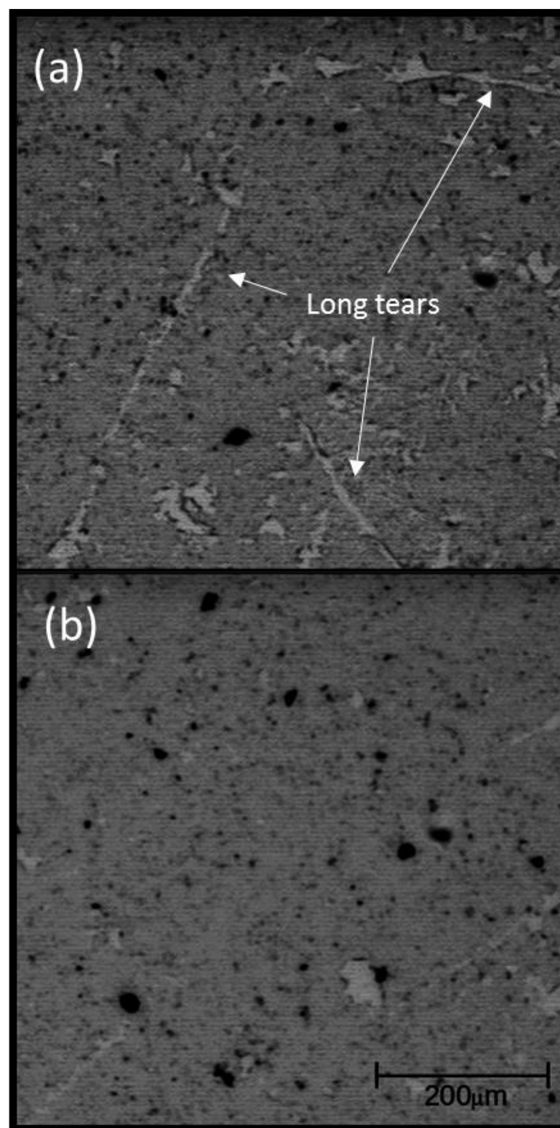

Figure 2-12 The effects of substrate preparation on the quality of transferred graphene. (a) CVD graphene transferred to a typical Si/SiO_2 chip. (b) CVD graphene transferred to the same chip that has been treated with 1 part 10:1 buffered oxide etch to 50 parts de-ionized water. There is a dramatic reduction in the number of long tears.

Figure 2-13 shows the effects of the duration of PMMA removal in acetone on the quality of transferred graphene. When the sample is left in the acetone for 2 hours and 4 hours, there is no significant amount of holes present. However, when the sample has been submerged in the acetone for 8 hours and 20 hours, tears of $100\ \mu m$ and bigger start forming. The longer the sample stays in the acetone, the bigger the holes become. We hypothesize that in a short period of time, the acetone removes the PMMA but over longer periods of time, the acetone removes the graphene as well since graphene is also organic.

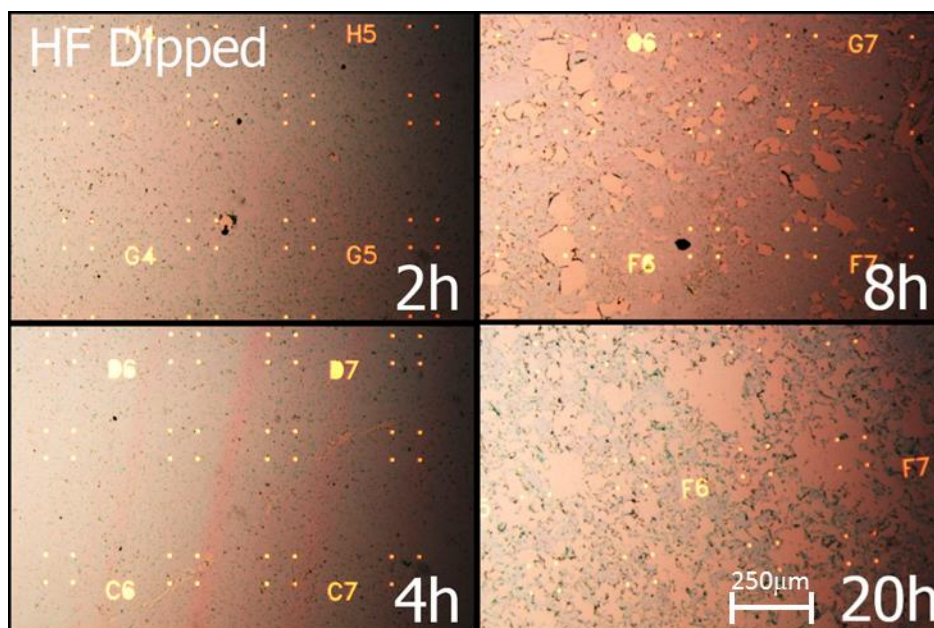

Figure 2-13 Evolution of hole size as the graphene remains in acetone for various duration. When the sample was submerged for 2 and 4 hrs, no noticeable holes were formed. When the sample was submerged for 8 hrs and longer, holes formed and grew with time.

Through the transfer optimization by minimizing the size and number of tears and holes, we were able use a standardized electrode pattern instead of individually designing the electrodes for each device. The yield also improved from $\sim 1-2\%$ yield to $\sim 30-40\%$ yield. Most importantly the quality of the graphene devices through visual inspection has also improved as shown in Figure 2-14.

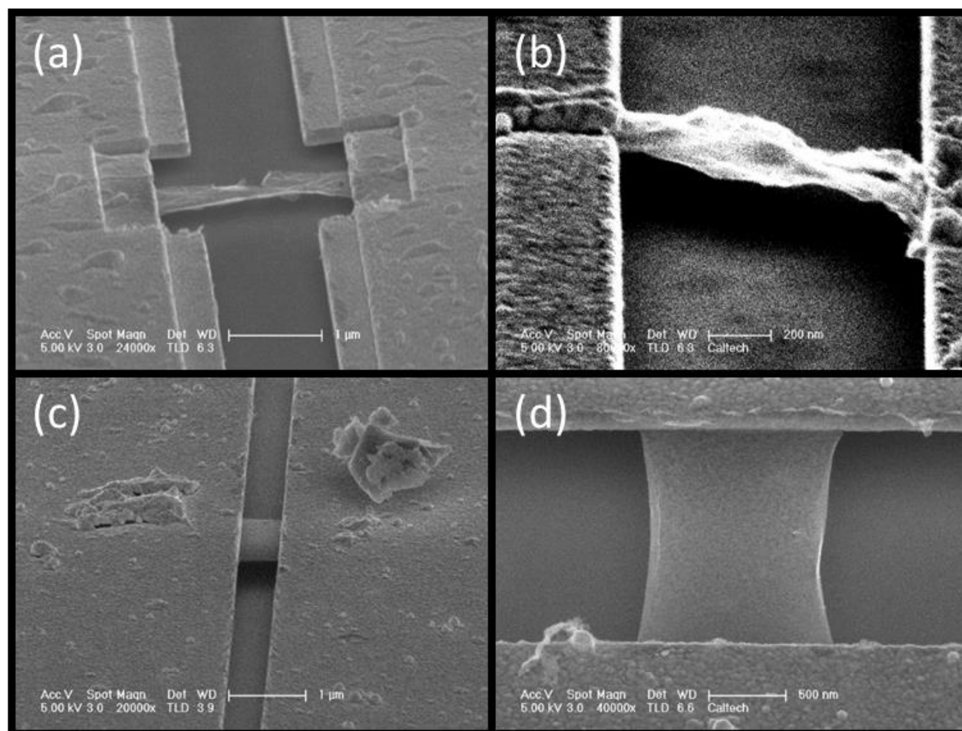

Figure 2-14 Quality of graphene before and after transfer optimization. (a, b) Scanning electron micrographs of suspended graphene devices with CVD graphene prior to the transfer process optimization. (c, d) Scanning electron micrographs of suspended graphene devices after the transfer process optimization.

2.9 NEMS Switches of Other Materials

In addition to demonstrating and optimizing graphene switches, we had also prototyped NEMS switches using aluminum nitride (AlN). As stated in Section 2.3 State of the Art NEMS Switches Capabilities, AlN is an interesting material because of its piezoelectric property. The expansion or contraction of AlN due to a small potential difference causes the NEMS to deflect. In this section, we describe our AlN cantilever switches fabrication process and performances as well as a prototype AlN doubly-clamped beam switch.

Our AlN cantilever switch fabrication process builds on a piezoelectric stack composed of bulk silicon as the substrate and on top of that $2\ \mu m$ of silicon dioxide, $20\ nm$ of AlN, $100\ nm$ of molybdenum (Mo), $50\ nm$ of AlN, $and\ 40\ nm$ of Mo on top (Figure 2-15a). Using electron beam lithography, a $200\ \mu m \times 400\ \mu m$ area was patterned for the evaporation of an $80\ nm$ layer of strontium fluoride (SrF_2). This SrF_2 layer serves as an etching mask for the following steps and defines the area where the cantilever will ultimately be located (Figure 2-15a). Using electron cyclotron resonance plasma etching (ECR), the top Mo layer not covered by the SrF_2 was removed (Figure 2-15c). Potassium hydroxide (KOH) was then used to etch the top AlN layer that is newly exposed (Figure 2-15d). The SrF_2 is then removed (Figure 2-15e) and electron beam lithography was used again to define the electrode locations where $5\ nm$ Cr/70 nm Au/80 nm SrF2 was thermally evaporated (Figure 2-15f). This is followed by another electron beam lithography step to define the profile of

the device which is to be covered by an additional layer of $80\ nm$ SrF_2 (Figure 2-15g). Using the Oxford etchers, areas not covered by the SrF_2 were then etched. In particular, an area is now electronically isolated from the device (Figure 2-15h, i). Through another electron beam lithography step, we patterned an area partially covering the cantilevers and electron beam evaporated SiO_2 as a sacrificial layer (Figure 2-15j). The SiO_2 sacrificial layer serves as a mechanical support and an electrical isolator for the next step. In this final electron beam lithography step, an area was patterned so that $5\ nm$ Cr/$70\ nm$ Au is evaporated (Figure 2-15k). This Cr/Au layer serves as the contact for the cantilever switch. Lastly, 10:1 buffered oxide etch was used to remove all of the SiO_2 (Figure 2-15l) and the device went through critical point drying.

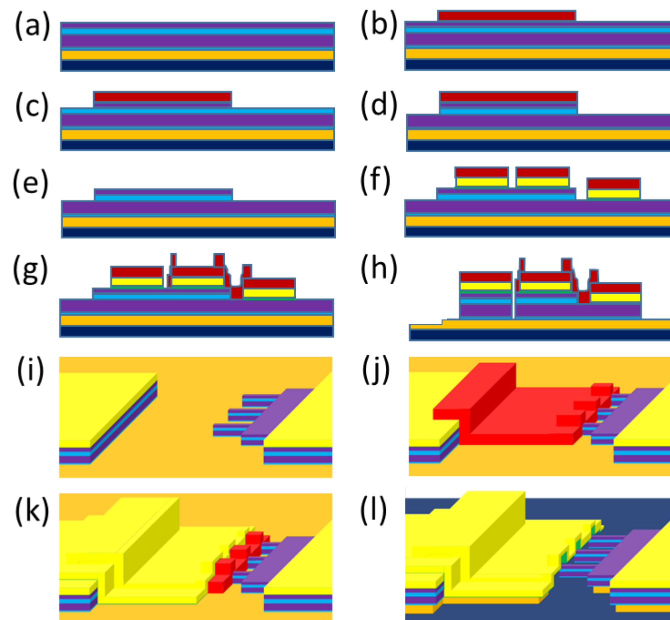

Figure 2-15 AlN NEMS switch fabrication procedure. (a-h) Cross section profile of the fabrication process. (i-l) 3D view of the final steps of the fabrication process. (a) We started with a piezoelectric stack of 40 nm top Mo, 50 nm AlN, 100 nm Mo, 20 nm bottom AlN, on top of a silicon wafer with 2 μm SiO_2. (b) An area of 200 μm $\times$ 400 μm was patterned for the thermal evaporation of 80 nm of SrF_2. (c) ECR etched away the top Mo layer not covered by SrF_2. (d) KOH etched away the newly exposed AlN. (e) SrF_2 was removed. (f) Area for electrodes are patterned and 5 nm Cr/70 nm Au/80 nm SrF_2 was thermally evaporated. (g) Additional area was patterned and SrF_2 was thermally evaporated. (h, i) The areas unprotected by SrF_2 were dry etched away. (j) An area covering part of the cantilever and the electrode was patterned for the electron beam evaporation of a sacrificial SiO_2 layer. (k) A similar area was patterned for the thermal evaporation of 5 nm Cr/70 nm Au. (l) The device was released by etching the SiO_2 away using 10:1 BOE then dried with a critical point dryer.

The AlN cantilever switches were tested using a setup similar to the graphene switches. Figure 2-16 shows a representative switching result from one of the AlN cantilevers that was $4\ \mu m$ long and $800\ nm$ wide. The major difference is with the actuation of the switch. With the AlN piezoelectric cantilever switches, instead of the voltage applied across the gate and the source as in the case with the graphene switches, the voltage is applied across the top and bottom layers of Mo. Since the two Mo layers sandwich the AlN layer, the potential difference on the top and bottom of the AlN layer causes the AlN cantilever to deflect until the cantilever makes contact with the gold overhang. Once there is physical contact between the cantilever and the gold, current flows through, thus turning on the switch.

The switching behavior of the AlN cantilever switches was similar to the graphene switches. The AlN switch shows high on-current to off-current ratio of $> 10^3$. The limiting factor was due to the maximum current we set. AlN cantilever switches also exhibit a low turn-on voltage of $1.9\ V$. However, there are no sharp jumps in the current as observed in the graphene switches because the AlN cantilever switches are actuated piezoelectrically.

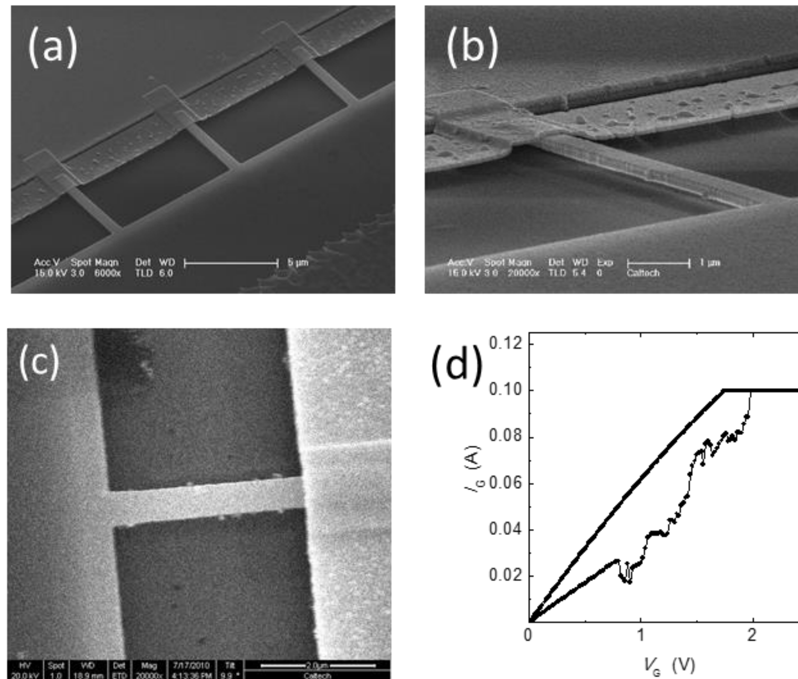

Figure 2-16 Scanning electron micrograph and performance of AlN cantilever switches. (a-c) Scanning electron micrograph of AlN cantilever switches. (a) Three cantilevers sharing electrical connections. (b) A close up view of one of the cantilevers. The gold overhang used as a contact is almost touching the AlN cantilever. (c) Top view of the AlN cantilever showing that the cantilever extends under the gold overhang. (d) Typical switching behavior of the AlN cantilever switch. Electrical contact was made at $\sim 1.9\ V$.

We also experimented with other AlN switch designs. Preliminary fabrication tests were performed to realize doubly-clamped AlN beams with a suspended gold bridge for contact. Figure 2-17 shows the result from the fabrication of a set of AlN doubly-clamped beams of various length for various actuation voltages. Unfortunately the suspended gold bridge for contact broke during fabrication.

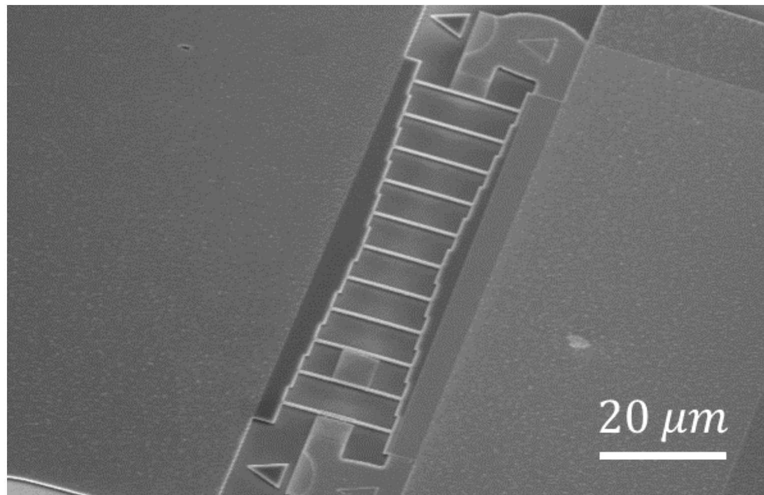

Figure 2-17 Scanning electron micrography of AlN doubly-clamped ladder switches. Eleven doubly-clamped beams sharing the same electrodes were fabricated. Because each of these beams have a different length, they all have a different actuation voltage. This image also shows the suspended gold contact bridge which is broken.

While the AlN switches have low actuation voltages, they lacked the small voltage swing of the graphene switches. Each of these materials has their unique properties which make them good candidates for NEMS switches. For the new generation of NEMS switches, we propose combining AlN and graphene for the fabrication to take advantages of their unique properties.

2.10 Summary

In summary, we explored NEMS switches as a possible paradigm to circumventing off-state leakage in transistor devices. We fabricated graphene doubly-clamped beam switches by exfoliated HOPG graphene and demonstrated that

these devices have a fast switching time of $< 100\ ns$ and low swing voltages of $< 10\ mV/decade$. While these devices usually fail after only $10 - 20$ cycles, we expect that with optimal engineering their performances could be greatly improved. CVD graphene grown on copper foil is used to replace HOPG graphene to allow for large scale engineering and testing. Experiments with various CVD graphene transfer steps has shown great improvement in the quality and the yield of graphene devices. Lastly, we prototyped AlN cantilever switches and demonstrated a modest pull-in voltage of $1.9\ V$. Further exploration and experimentation ongoing with these devices may enable the engineering of a new generation of NEMS switches that take advantage of the unique properties of these novel materials.

2.11 Bibliography

1. Kim, N.S., et al., *Leakage current: Moore's law meets static power.* Computer, 2003. **36**(12): p. 68-75.
2. Roy, K., S. Mukhopadhyay, and H. Mahmoodi-Meimand, *Leakage current mechanisms and leakage reduction techniques in deep-submicrometer CMOS circuits.* Proceedings of the IEEE, 2003. **91**(2): p. 305-327.
3. Narendra, S.G. and A.P. Chandrakasan, *Leakage in Nanometer CMOS Technologies*. 2006: Springer US.
4. Wilk, G.D., R.M. Wallace, and J.M. Anthony, *High-κ gate dielectrics: Current status and materials properties considerations.* Journal of Applied Physics, 2001. **89**(10): p. 5243-5275.
5. Yapu, Z., *Stiction and anti-stiction in MEMS and NEMS.* Acta Mechanica Sinica. **19**(1): p. 1-10.
6. Feng, P.X., et al., *Very low voltage, ultrafast nanoelectromechanical switches and resonant switches*. 2012, Google Patents.
7. Feng, X.L., et al., *Nano-electro-mechanical systems switches*. 2012, Google Patents.
8. Gupta, R.K. and S.D. Senturia. *Pull-in time dynamics as a measure of absolute pressure*. in *Tenth Annual International Workshop on Micro Electro Mechanical Systems, 1997. MEMS '97, Proceedings, IEEE.* 1997.
9. Snodgrass, W., et al. *Pseudomorphic InP/InGaAs Heterojunction Bipolar Transistors (PHBTs) Experimentally Demonstrating fT = 765 GHz at 25C*

Increasing to fT = 845 GHz at -55;C. in *2006 International Electron Devices Meeting*. 2006.

10. Muldavin, J.B. and G.M. Rebeiz. *Nonlinear electro-mechanical modeling of MEMS switches*. in *Microwave Symposium Digest, 2001 IEEE MTT-S International*. 2001.
11. Zaghloul, U. and G. Piazza. *10 - 25 nm piezoelectric nano-actuators and NEMS switches for millivolt computational logic*. in *2013 IEEE 26th International Conference on Micro Electro Mechanical Systems (MEMS)*. 2013.
12. Zaghloul, U. and G. Piazza, *Sub-1-volt Piezoelectric Nanoelectromechanical Relays With Millivolt Switching Capability*. IEEE Electron Device Letters, 2014. **35**(6): p. 669-671.
13. Piazza, G. *Alumimun nitride piezoelectric NEMS resonators and switches*. 2010.
14. Peschot, A., C. Qian, and T.-J. Liu, *Nanoelectromechanical Switches for Low-Power Digital Computing*. Micromachines, 2015. **6**(8): p. 1046.
15. Feng, P.X.L., *Nanoelectromechanical Switching Devices: Scaling Toward Ultimate Energy Efficiency and Longevity*. 2013 Third Berkeley Symposium on Energy Efficient Electronic Systems (E3s), 2013.
16. He, T., et al. *Dual-gate silicon carbide (SiC) lateral nanoelectromechanical switches*. in *Nano/Micro Engineered and Molecular Systems (NEMS), 2013 8th IEEE International Conference on*. 2013.

17. He, T., et al. *Time-domain AC characterization of silicon carbide (SiC) nanoelectromechanical switches toward high-speed operations*. in *2013 Transducers & Eurosensors XXVII: The 17th International Conference on Solid-State Sensors, Actuators and Microsystems (TRANSDUCERS & EUROSENSORS XXVII)*. 2013.

18. Feng, X.L., et al., *Low Voltage Nanoelectromechanical Switches Based on Silicon Carbide Nanowires.* Nano Letters, 2010. **10**(8): p. 2891-2896.

19. Dequesnes, M., Z. Tang, and N.R. Aluru, *Static and Dynamic Analysis of Carbon Nanotube-Based Switches.* Journal of Engineering Materials and Technology, 2004. **126**(3): p. 230-237.

20. Dujardin, E., et al., *Self-assembled switches based on electroactuated multiwalled nanotubes.* Applied Physics Letters, 2005. **87**(19): p. 193107.

21. Sharma, P., et al., *Electromagnetic Performance of RF NEMS Graphene Capacitive Switches.* IEEE Transactions on Nanotechnology, 2014. **13**(1): p. 70-79.

22. Hernandez, Y., et al., *High-yield production of graphene by liquid-phase exfoliation of graphite.* Nat Nano, 2008. **3**(9): p. 563-568.

23. Lee, C., et al., *Measurement of the Elastic Properties and Intrinsic Strength of Monolayer Graphene.* Science, 2008. **321**(5887): p. 385-388.

24. Liu, M., et al., *Carbyne from First Principles: Chain of C Atoms, a Nanorod or a Nanorope.* ACS Nano, 2013. **7**(11): p. 10075-10082.

25. Yang, Y.H. and W.Z. Li, *Radial elasticity of single-walled carbon nanotube measured by atomic force microscopy.* Applied Physics Letters, 2011. **98**(4): p. 041901.

26. Dresselhaus, M.S., et al., *Electronic, thermal and mechanical properties of carbon nanotubes.* Philosophical Transactions of the Royal Society of London A: Mathematical, Physical and Engineering Sciences, 2004. **362**(1823): p. 2065-2098.

27. Choyke, W.J., H. Matsunami, and G. Pensl, *Silicon Carbide: Recent Major Advances*. 2013: Springer Berlin Heidelberg.

28. Wachtman, J.B. and D.G. Lam, *Young's Modulus of Various Refractory Materials as a Function of Temperature.* Journal of the American Ceramic Society, 1959. **42**(5): p. 254-260.

29. Boyd, E.J. and D. Uttamchandani, *Measurement of the Anisotropy of Young's Modulus in Single-Crystal Silicon.* Journal of Microelectromechanical Systems, 2012. **21**(1): p. 243-249.

30. Berger, C., et al., *Electronic Confinement and Coherence in Patterned Epitaxial Graphene.* Science, 2006. **312**(5777): p. 1191-1196.

31. Reich, S. and C. Thomsen, *Raman spectroscopy of graphite.* Philosophical Transactions of the Royal Society of London A: Mathematical, Physical and Engineering Sciences, 2004. **362**(1824): p. 2271-2288.

32. Blake, P., et al., *Making graphene visible.* Applied Physics Letters, 2007. **91**(6): p. 063124.

33. Ferrari, A.C., et al., *Raman Spectrum of Graphene and Graphene Layers.* Physical Review Letters, 2006. **97**(18): p. 187401.

34. Chen, C., et al., *Performance of monolayer graphene nanomechanical resonators with electrical readout.* Nat Nano, 2009. **4**(12): p. 861-867.

Chapter 3

SPEED OF SOUND MEASUREMENT VIA ANHARMONIC NONLINEARITY IN NEMS

In this chapter we provide an overview of mechanical motion in NEMS resonators including the theory of anharmonic nonlinearity, and then describe experimental work that employs this nonlinearity to determine the speed of sound in NEMS. We begin by modeling a NEMS resonator as a simple harmonic oscillator (SHO) and determining the resonator's key properties, including mode shape and resonant frequency. We then discuss additional effects on the mechanical response using calculations employing secular perturbation theory. We conclude this chapter with an alternative method for solving the system using an action argument, and show that the square of the resonant frequency is a natural way of describing the system.

3.1 Motivation

A fundamental mechanical property of all NEMS and nanoscale devices is their longitudinal speed of sound $\nu_k = E_k/\rho$ for a one-dimensional material. Here, E_k is Young's modulus along (vector) crystallographic orientation $\boldsymbol{k}$, and ρ is the mass density of the material. In bulk material at macroscopic scales, longitudinal speeds of sound are often determined by time-of-flight (TOF) measurement of ultrasonic pulses [1] or stress-strain characterization [2]. For anisotropic single-crystal materials, the speed of sound along various crystallographic directions can

also be derived from the dispersion relations that can be obtained, for example, by X-ray scattering experiments [3]. Nevertheless, many conventional techniques apply only to bulk structures and cannot reveal properties within a NEMS device. For NEMS devices, the most common measurement method of the speed of sound is by probing localized vibrations (standing wave) across the nanostructure [4-6].

While *in-situ* measurements are necessary for local characterization of the NEMS devices, such measurements [7] generally convolve intrinsic material properties (e.g., bulk longitudinal speed of sound) [8], structural properties (e.g., intrinsic stress, clamping conditions, and defects), and external factors (e.g., induced stress). Previous experiments have only considered extreme cases of tension, which is often not applicable for most devices [7]. Furthermore, intrinsic stress and externally induced stress are typically not known *a priori* and can be hard to measure within nanoscale devices. As a result, researchers often employ bulk values or estimates of common material properties when analyzing data or performing simulations of the devices.

Previous approaches to sound speed measurement in doubly-clamped beams employ multiple modes to calculate the total stress and longitudinal speed of sound [9]. However, the tension of the beam is generally not known *a priori* and this can result in inaccurate mode shapes and, therefore, final results. In the extreme case of high tension, the longitudinal speed of sound has a less significant effect on the dynamics of the beam. Therefore, the uncertainty in the longitudinal speed of sound

is higher. In this chapter, we extend the characterization of local modes to the regime of nonlinear mechanical response, we are able to experimentally decouple the effects of stress and the longitudinal speed of sound of the beam and locally determine both of these material properties. This can be performed using just a single mode. We anticipate that these results will stimulate further improvement in material characterization, and likewise, accurate modeling and optimal engineering of NEMS.

3.2 Beam Theory

We begin our analysis with the Euler-Bernoulli equation to model the dynamics of an elastic beam. We draw on the analysis of Lifshitz and Cross [10], which we modify for our purposes. The deflection, $X(z,t)$, of an elastic beam normal to its axis is governed by the Euler-Bernoulli equation [11]:

$$EI\frac{\partial^4 X}{\partial z^4} - T\frac{\partial^2 X}{\partial z^2} + \rho S\frac{\partial^2 X}{\partial t^2} = 0, \qquad \text{Eq. 3-1}$$

where z is the Cartesian coordinate along the beam axis, t is the time, ρ is the beam's mass density, S is its cross sectional area, E its Young's modulus, I its areal moment of inertia, and T the tension along the beam axis. We consider the case of a doubly-clamped beam, which generally exhibits nonlinear response for deflections, X, that are comparable to or greater than the beam thickness. This nonlinearity is due to tension induced along the beam axis [9].

The beam deflection function of mode n is expressed as $X_n(z,t) = \phi_n(z)x_n(t)$, where $\phi_n(z)$ is the spatial dependence of the nth linear eigenmode and $x_n(t)$ is its time dependence; $\phi_n(z)$ is normalized by the maximum value nearest to the beam center. Substituting this expression into Eq. 3-1 and utilizing the orthogonality properties of $\phi_n(z)$ produces the required equation of motion for $x_n(t)$:

$$\ddot{x}_n + \omega_n^2 x_n \left(1 + \alpha_n \left[\frac{x_n}{h}\right]^2\right) = 0; \qquad \text{Eq. 3-2}$$

here in the limit of zero residual tension along the beam axis, the nonlinear coefficient, α_n, is defined

$$\alpha_n \equiv \frac{Sh^2}{2I} \frac{\left(\int_0^1 (\Phi_n')^2 dz\right)^2}{\int_0^1 \Phi_n''^2 dz}, \qquad \text{Eq. 3-3}$$

Here, the normalized coordinate z in Eq. 3-3 is scaled by the beam length L. Eq. 3-3 is recognizable as the Duffing equation, from which it follows that nonlinear response is exhibited only for deflections on the order of the beam thickness, as mentioned above. The dimensionless nonlinearity parameter, α_n, contains the factor $Sh^2/(2I)$ which equals 6 for a doubly-clamped beam with a rectangular cross section, in the limit of zero tension along the beam axis [10]. Here, we account for arbitrary residual beam tension and separate its contribution to the dynamics from that of the Young's modulus. In this situation, the eigenmodes ϕ_n in the presence of arbitrary (constant) tension, T_0, must be used in Eq. 3-3 to determine α_n. These

modes satisfy $\phi_n^{(\mathrm{iv})} - \beta\phi_n'' - \overline{\Omega}_n^2\phi_n = 0$, where $\beta = T_0L^2/(EI)$ and the normalized linear resonant frequency $\overline{\Omega}_n = \overline{\omega}_n(\beta)\sqrt{\rho S L^4/(EI)}$. Here, $\overline{\omega}_n$ is the dimensional linear frequency that depends on both the Young's modulus and the residual tension.

3.3 Doubly-clamped Beam Mode Shape

Since the mode shape directly affects the resonant frequency and the nonlinear coefficient, in this section, we will discuss the effects of stress on the mode shape. By assuming the temporal response to the Euler-Bernoulli equation to be sinusoidal, we can rewrite Eq. 3-1 to include only the spatial derivatives. This allows us to solve for the mode shape and the maximum displacement of the beam. In the limit where the tension is negligible and the bending moment is predominant (e.g., $T_0L^2 \gg EI$), the solution to the fourth-order differential equation has the form:

$$p(\cos cx - \cosh cx) - q(\sin cx - \sinh cx). \qquad \text{Eq. 3-4}$$

For a doubly-clamped beam, the boundary conditions are such that the displacement and the slope at the clamping points vanish (e.g., $\Phi_\mathrm{n}(0) = \Phi_\mathrm{n}(L) = \Phi_\mathrm{n}'(0) = \Phi_\mathrm{n}'(L) = 0$). By substituting the general form of the solution and the boundary conditions for a doubly-clamped beam back into Eq. 3-1, we see that the mode shape, Φ_n, is given by:

$$(\sin k_n - \sinh k_n)\left(\cos\frac{k_n x}{L} - \cosh\frac{k_n x}{L}\right) - (\cos k_n - \cosh k_n)\left(\sin\frac{k_n x}{a} - \sinh\frac{k_n x}{L}\right), \quad \text{Eq. 3-5}$$

where k_n are the solutions to

$$\cos(k_n L)\cosh(k_n L) = 1. \quad \text{Eq. 3-6}$$

The solution to Eq. 3-6 is not unique and each solution corresponds to a different resonant mode. Table 3-1 below gives the first six solutions for k_n.

Mode, n	k_n
1	4.73004
2	7.8532
3	10.9956
4	14.1372
5	17.2788
6	20.4204

Table 3-1 A table of the first six values of k which satisfy the boundary conditions for a doubly-clamped beam: solutions to $\cos(k_n L)\cosh(k_n L) = 1$.

The resulting mode shapes are shown below in Figure 3-1.

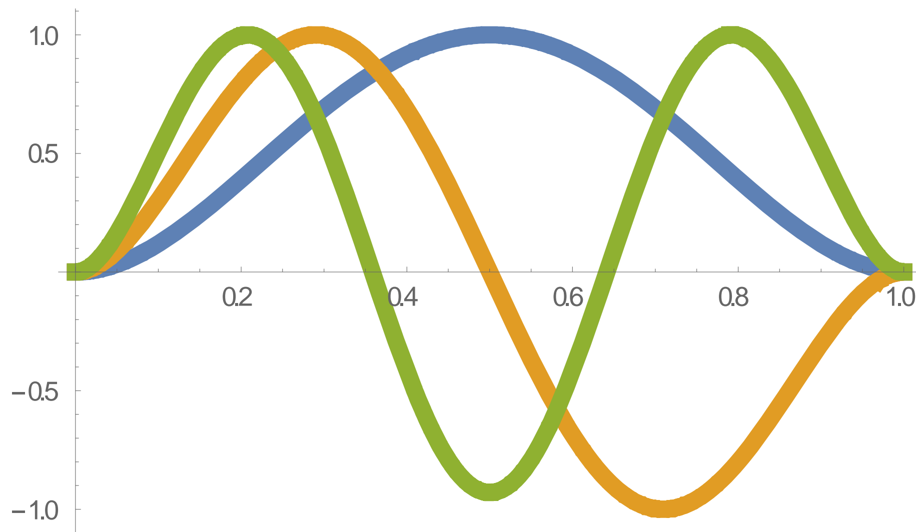

Figure 3-1 The lowest three mode shapes (blue: first mode, orange: second mode, green: third mode) of a doubly-clamped beam where the tension is negligible. The slope at the clamping points vanishes (e.g., $\Phi'(0) = \Phi'(1) = 0$). The mode shapes have been normalized so that the maximum for each mode is unity.

In the opposite limit, where the tension is predominant and the bending moment of the beam is negligible (e.g., $T_0L^2 \ll EI$), the fourth-order differential equation reduces to a second-order differential equation and the solution has the form $a(\cos bx) - c(\sin bx)$. In this case the mode shape resembles that of a string. The resulting mode shapes are shown below in Figure 3-2.

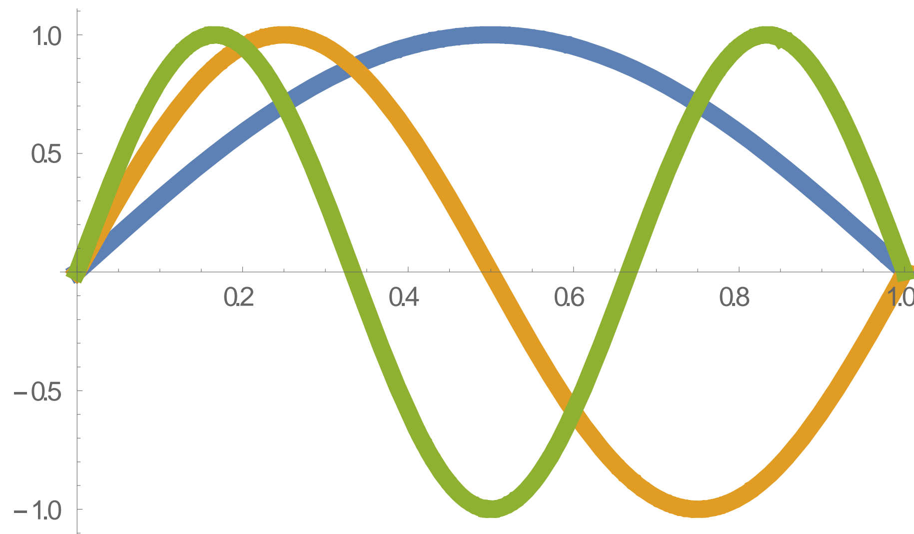

Figure 3-2 The lowest three mode shapes (blue: first mode, orange: second mode, green: third mode) of a doubly-clamped beam where the bending moment is negligible. The inflection at the clamping points vanishes (e.g., $\Phi''(0) = \Phi''(1) = 0$). The mode shapes have been normalized so that the maximum for each mode is unity.

While the general mode shapes for the two limiting cases look similar, the *exact* mode shapes are important, especially in the application of mass spectrometry and inertial imaging – as we will discuss in Chapter 4. These two limiting cases are plotted on the same graph for comparison for each of the first two modes in Figure 3-3.

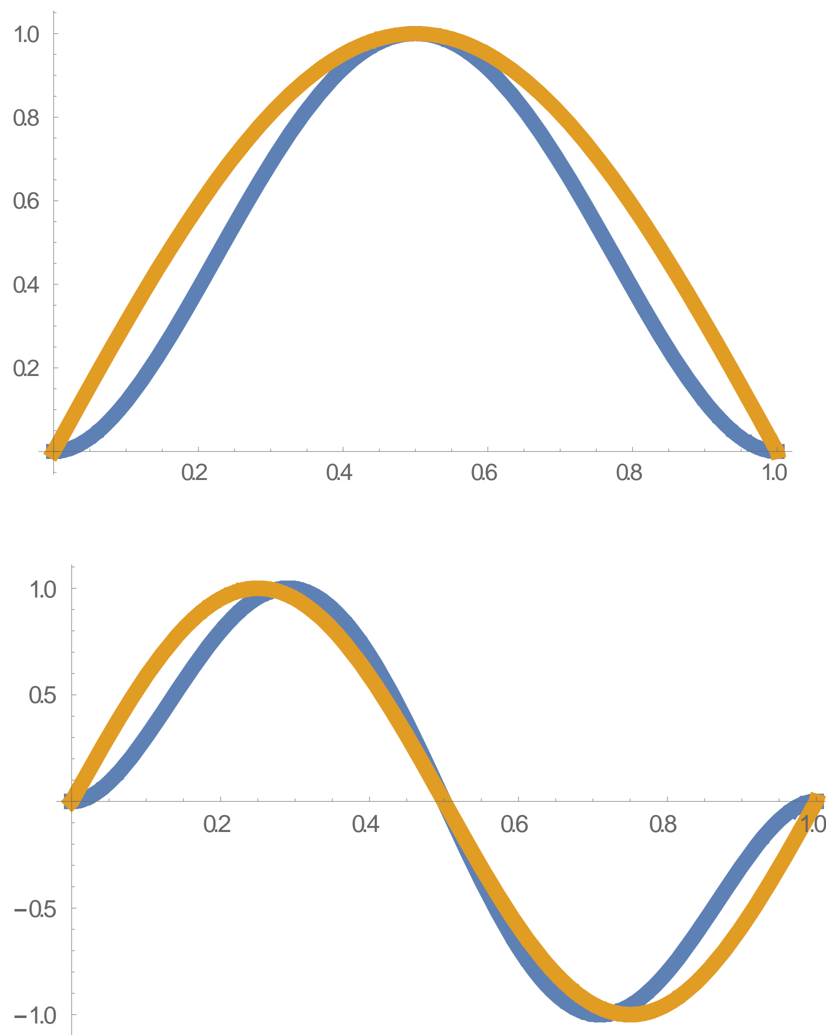

Figure 3-3 Comparison of the effect of tension on the mode shape for the lowest two doubly-clamped beam modes. The blue curve is where the bending moment is dominating and the orange curve is where the tension is dominating. The top plot is the first resonant mode and the bottom plot is the second resonant mode.

For the second and third modes, the location of maximum displacement depends on the tension. These differences, even if small, prove critical for NEMS-based mass spectrometry and inertial imaging.

3.4 Novel Representation of Resonant Frequency

We continue our analysis of beam theory by showing a novel representation of the resonant frequency. The nonlinear resonant frequency of the nth mode, ω_n, is related to that of the linear frequency, $\bar{\omega}_n$, by

$$\omega_n^2(\beta) = \bar{\omega}_n^2(\beta) + \frac{3\alpha_n(\beta)\bar{\omega}_n^2(\beta)}{4h^2} A_n^2, \qquad \text{Eq. 3-7}$$

where A_n is the amplitude of x_n under the (leading order) harmonic approximation, which depends on the tension parameter, β. We do not employ the usual formula reported by Lifshitz and Cross [10] that relates these frequencies directly, but instead employ the square of the frequency because the effects of bending rigidity and tension thereby become approximately decoupled.

Use of Eq. 3-7 enables determination of both the Young's modulus and the residual tension in the beam. Measuring the beam's resonant frequency as a function of amplitude in the nonlinear regime and plotting the square of this frequency as a function of the amplitude squared gives the linear relation: $\omega_n^2 = a + bA_n^2$. Accordingly, by measuring the vertical intercept, a, and slope of this line, b, the residual tension parameter, β, is determined as the solution to

$$\alpha_n(\beta) = \frac{4bh^2}{3a}. \qquad \text{Eq. 3-8}$$

This allows direct evaluation of the longitudinal speed of sound via

$$v_l = \left(\frac{E}{\rho}\right)^{1/2} = \left(\frac{16bL^4}{\alpha_n(\beta)\bar{\Omega}_n^2(\beta)}\right)^{1/2}. \quad \text{Eq. 3-9}$$

Importantly, the product $\alpha_n(\beta)\bar{\Omega}_n^2(\beta)$ – required in Eq. 3-9 – is a very weak function of β and decreases only slightly (~25%) as β is increased from zero to infinity; see Figure 3-4. The measurement therefore approximately decouples the influence of residual tension and bending rigidity, i.e., determination of longitudinal speed of sound is robust to uncertainty in the beam thickness and the tension, as specified by Eq. 3-8. This provides a tremendous advantage over other approaches that require accurate knowledge of the residual tension to determine the longitudinal speed of sound, e.g., by using the linear resonant frequencies of two modes [9].

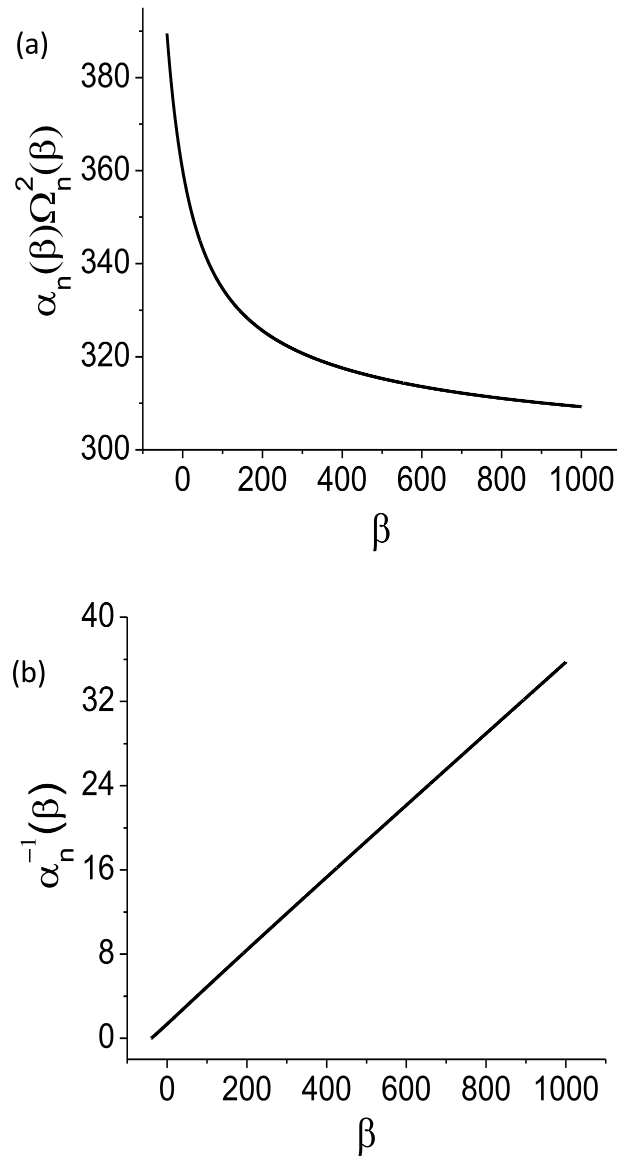

Figure 3-4 Plot of the dimensionless functions $\alpha_n\Omega_n^2$ and α_n^{-1} as a function of the dimensionless tension parameter β. (a) Plot of the dimensionless function $\alpha_n(\beta)\Omega_n^2(\beta)$ which relates the speed of sound to the dimensionless tension parameter, β. (b) Plot of dimensionless function $\alpha_n^{-1}(\beta)$ which allows us to determine β using Eq. 3-7. The function $\alpha_n^{-1}(\beta)$ can be approximated as $7.8478 \times 10^{-1} + \beta\ (1.80563\ \times 10^{-2})$.

3.5 Experimental Determination of Resonant Frequency

Earlier, as part of the discussion of the solution to the Euler-Bernoulli equation in section 3.2, we mentioned that the characteristic value of the solution is the resonant frequency, ω_0. In this section, we will discuss response of the resonator at the resonant frequency and, in particular, how to experimentally measure the resonant frequency with requisite care.

Up until now, we have neglected the exact temporal dependence of the solution and have instead assumed that the response is sinusoidal in time. In many experiments, the system is driven by a sinusoidal source. As the driving force frequency approaches the resonant frequency of the system, the response increases. This response is described by a Lorentzian function. The amplitude and the phase of the Lorentzian function are given by:

$$|x(\omega)| = \frac{F_0}{m}\frac{1}{\sqrt{(\omega_0^2 - \omega^2)^2 + \gamma^2\omega^2}}, \qquad \text{Eq. 3-10}$$

$$\tan\phi(\omega) = -\frac{\gamma\omega}{\omega_0^2 - \omega^2}. \qquad \text{Eq. 3-11}$$

Here F_0 is the force on the resonator, m is the mass of the resonator, ω is the frequency of the driving force, and γ is the damping coefficient.

Often the resonant frequency is defined by the phase response of the resonator. At very low frequencies ($\omega \ll \omega_0$), the resonator response is in phase with

the drive. At very high frequencies ($\omega \gg \omega_0$), the response of the resonator is out of phase with the drive by a factor of $-\pi$. At the resonant frequency ($\omega = \omega_0$), the resonator response is exactly $\frac{\pi}{2}$ out of phase with the drive.

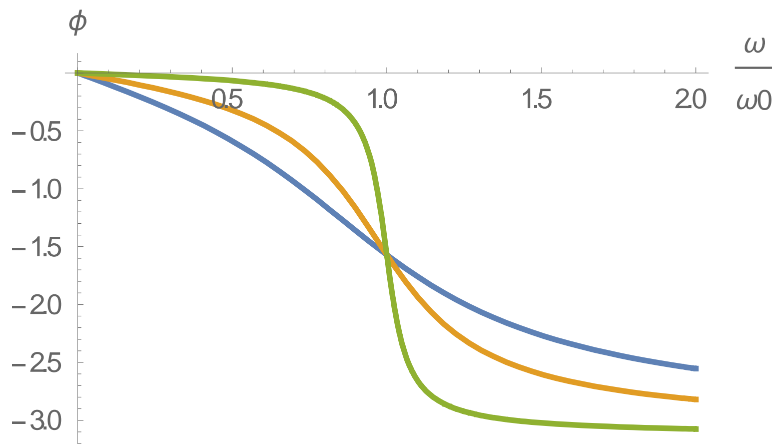

Figure 3-5 Phase of the resonator response to a sinusoidal driving force as a function of normalized frequency, ω/ω_0. Different curves correspond to different values of γ: blue: $\gamma/\omega_0 = 1$, orange: $\gamma/\omega_0 = 0.5$, green: $\gamma/\omega_0 = 0.1$. As γ/ω_0 decreases, the slope of the phase as resonance gets steeper.

Perhaps more commonly, the resonant frequency is approximately defined as the frequency where the magnitude of the Lorentzian response is maximal. However, more careful examination shows that this definition is not strictly correct except in the limit where $\frac{\gamma}{\omega_0} \gg 1$. In our experiment described here, $\frac{\gamma}{\omega_0}$ is on the order of 100 to 1000, so this latter approximation is sufficient. Accordingly, we use the frequency corresponding to the maximum amplitude as the resonant frequency.

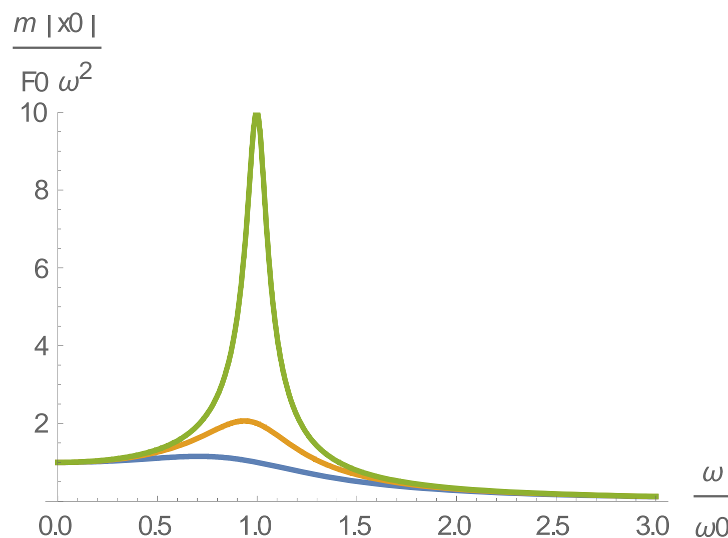

Figure 3-6 Phase of the resonator response to a sinusoidal driving force as a function of normalized frequency ω/ω_0. Different curves correspond to different values of γ: blue: $\gamma/\omega_0 = 1$, orange: $\gamma/\omega_0 = 0.5$, green: $\gamma/\omega_0 = 0.1$. As γ/ω_0 decreases the slope of the phase at resonance gets steeper.

3.6 Novel Doubly-clamped Beam Fabrication Procedure to Avoid Undercut

We demonstrate use of the anharmonic (Duffing) nonlinearity in doubly-clamped NEMS beams to determine the speed of sound *in-situ*. In this section, we describe the fabrication process employed to produce ideal silicon doubly-clamped beams for these investigations. As we describe, it proves essential to clamp the beam ends ideally, with no undercuts. We will begin with a discussion of how traditional methods of fabrication typically result in doubly-clamped beams with undercuts that introduce uncertainty into the effective device length. In this situation our analysis can fail. We will then show an optimized method of fabrication that avoid such issues and results in more ideal structures.

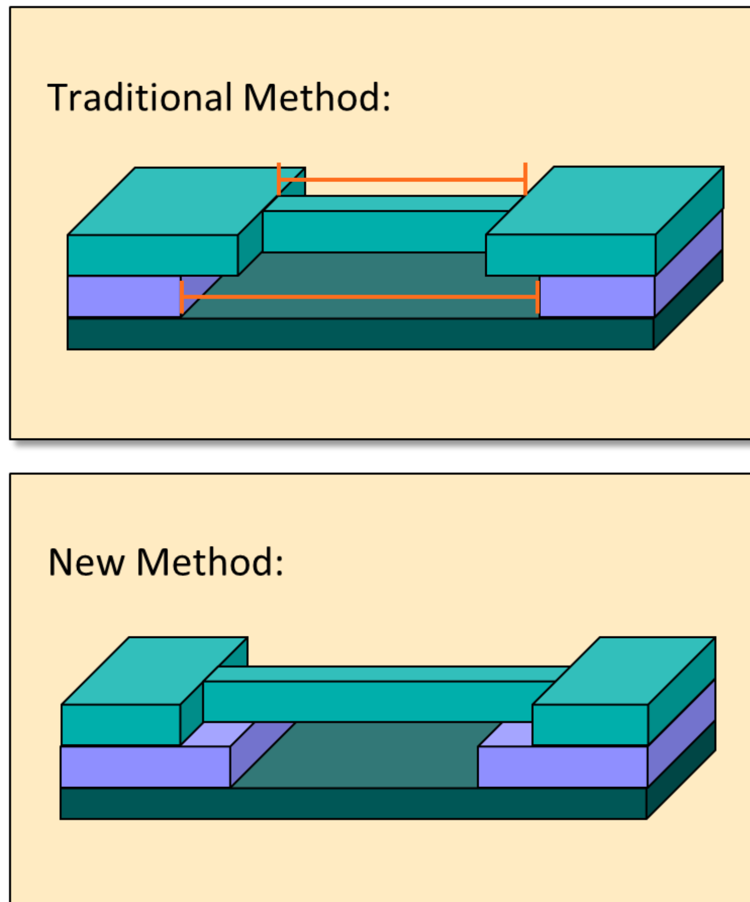

Figure 3-7 Comparison of the traditional and new method of fabricating doubly-clamped beams. In both diagrams the lighter green layer is the top silicon device layer, the purple is the silicon dioxide insulating layer, and the darker green layer is the substrate. In the traditional method, the length of the beam is not well defined. It is somewhere between where the beam is defined on the silicon device layer and where the silicon dioxide stops supporting the device layer. In the bottom diagram, the device length is well defined as where it is supported by the oxide layer.

Traditional methods for fabricating doubly-clamped silicon beams are a simple two-step process, yet they result in an undercut (Fig. 3.7). In the first

generation of devices we fabricated, we employed this common approach. We started with a silicon on insulator wafer with $285\ nm$ silicon device layer that is separated from the silicon substrate by a $400\ nm$ silicon dioxide (sacrificial) layer. Using with electron-beam lithography with a PMMA bilayer as the resist, we defined the beam profile by patterning two rectangular areas on either side of the beam. After developing the resist, we dry etch the wafer to remove silicon in these two rectangular areas. After removing the resist, the wafer is placed in a buffered oxide etch solution (1:10 hydrofluoric acid), which etches the sacrificial layer beneath the beam to suspend the device. The suspended device is then placed in an Automegasamdri®-915B critical point dryer to remove liquid without encountering liquid surfacing tension, which can often result in collapsing the device.

To avoid an undercut at the clamps, these aforementioned fabrication steps are reversed. The insulating layer is first etched to suspend the device layer. The steps are as follows (Fig. 3.9): a hole of diameter $100\ nm$ is first etched through the top silicon layer using a reactive ion etch so that the SiO_2 layer becomes exposed. Hydrofluoric acid (HF) was then used to isotopically etch the SiO_2 to create a suspended (approximately) circular membrane. This is followed by critical point drying to prevent the membrane from collapsing due to surface tension. Finally, the beams are then defined using a reactive ion etch of the entire structural layer above the cavity formed in the first step except for regions that define two parallel beams located approximately $5\ \mu m$ away from the original hole.

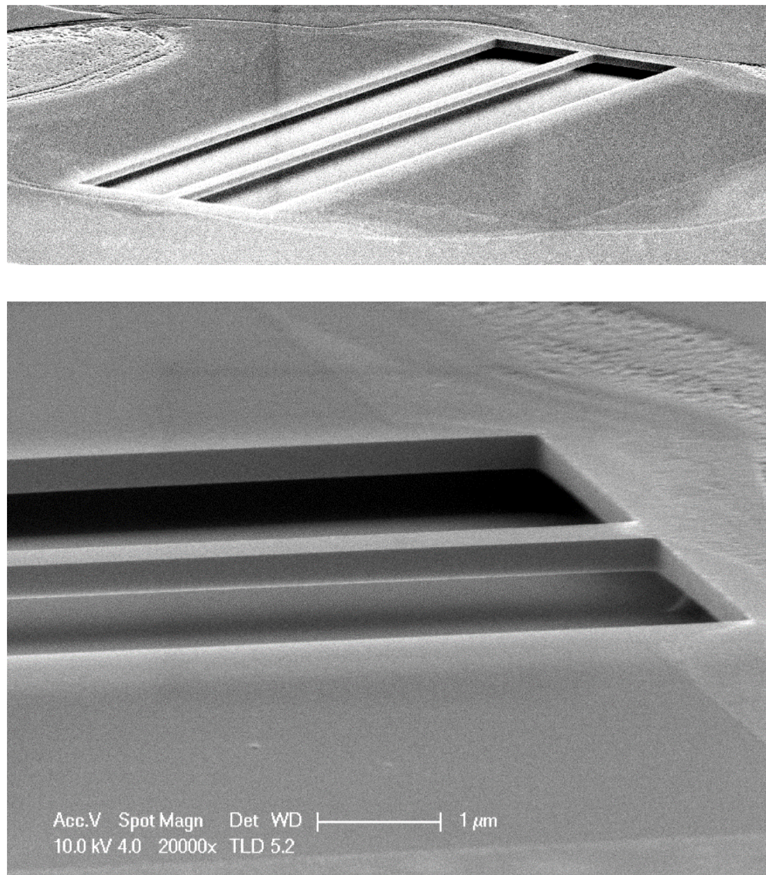

Figure 3-8 Scanning electron microscopy images of silicon doubly-clamped beams as fabricated using traditional methods. (Top) Overview of the entire doubly-clamped beam. (Bottom) A zoomed in view of the clamping area. The undercut in the silicon dioxide layer is very noticeable.

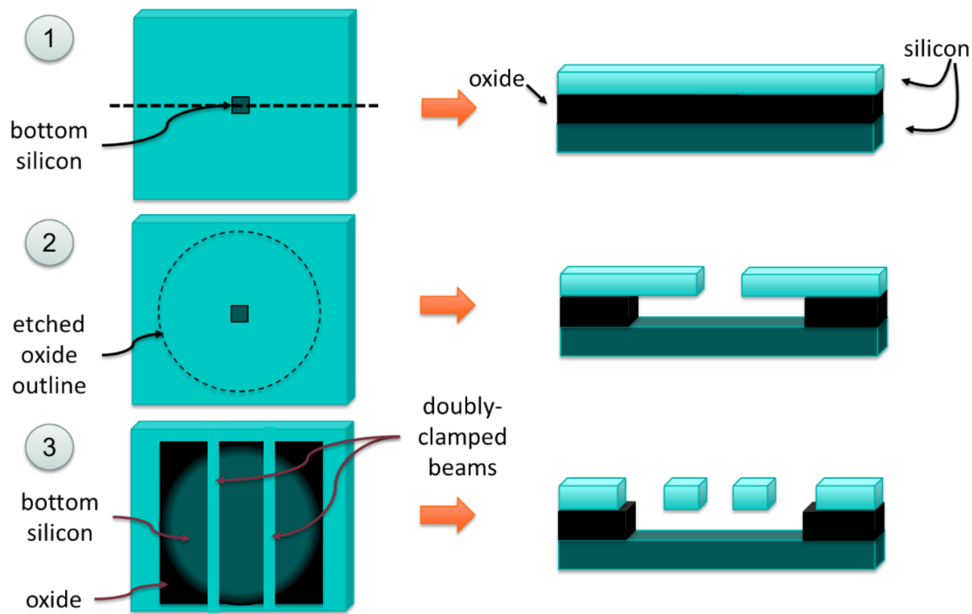

Figure 3-9 Novel process for fabricating doubly-clamped beams with no uncercuts. The left column is a top view of the fabrication process while the right column is the cross section view along the dotted line in the upper left figure for each corresponding step. In step 1, a small hole of $\sim 100\ nm$ is etched through the top silicon layer using dry etch. In step 2, 49% hydroflouric acid is used to remove the silicon dioxide under the silicon. Because hydrofluoric etch is isotropic, the resulting etched area is approximately circular. The dotted circle on the left shows approximately where the etch stops. In step 3, the beam profile is defined using another dry etch step, resulting in two suspended doubly-clamped beams.

The dimensions of the suspended circular membrane ultimately define the length of the beams. While the beam length at the clamping points varies slightly across its width because of the approximately circular geometry of the original undercut etch, this uncertainty in length is very small compared to the overhang is that present in beams fabricated by the original method. Using this new approach, single-crystal silicon beams of length $L = 25\ \mu m$, width $w = 1\mu m$, and thickness $t = \ 285\ nm$ were fabricated in the (100) plane. Each beam was fabricated such that the longitudinal direction of the beam was oriented with a predetermined angle with respect to the <110> crystallographic direction.

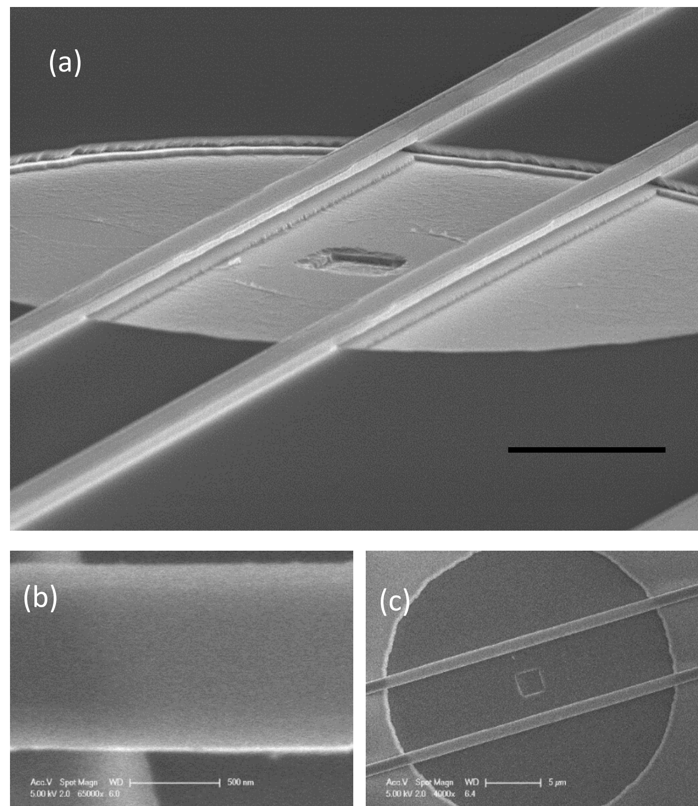

Figure 3-10 Scanning electron micrographs of doubly-clamped silicon beams of dimensions $[l, w, t] = 24.6\ \mu m, 1.07\ \mu m, 285\ nm$. (a) Top down view of the doubly-clamped silicon beams. The beams run from the bottom left to the upper right. The area within the circle has the entire thickness of the SiO_2 removed via a hydrofluoric acid wet etch. The beam within this area is suspended. The scale bar in (a) is $5\mu m$. (b) A zoomed in view of the clamped edge of the silicon beam. Undercut in the SiO_2 is not present due to the new fabrication procedure where the length of the beam is defined by suspending the silicon as a plate prior to defining the silicon beam. (c) A tilted view (75°) of the doubly-clamped silicon beam.

3.7 Experimental Setup for Measuring Anharmonic Nonlinearity

In this section, we describe the method of actuating and detecting the doubly-clamped beams fabricated using the procedure described in the previous section. Device actuation was achieved with a ceramic piezoelectric element (piezoshaker) that was affixed to the sample; it was driven by applying an AC voltage to metallic electrodes deposited on the piezoshaker surfaces. NEMS device motion was detected using optical interferometry [12] with a helium-neon (HeNe) laser (633 nm) at room temperature in a vacuum chamber with pressure $< 10^{-5}$ Torr. As the doubly-clamped beam vibrates, the path length difference between the light reflected from the device and the light reflected from the substrate creates observable interference. This time-dependent optical interference was then transduced into an electrical signal via a photoreceiver (New Focus model 1801) and detected using a network analyzer (Agilent model 33250).

To relate the detected electrical signal into NEMS beam displacement, the known magnitude of thermomechanical fluctuations was employed. The transduced optical signal from thermomechanical fluctuations, in absence of piezoshaker drive, was detected using a spectrum analyzer (Agilent model PXA 9030A). We followed the formulation of Hiebert *et al.* [12], which relates the displacement (power) spectral density to the voltage (power) spectral density to deduce the transduction responsivity, which relates NEMS displacement to photodetector output voltage.

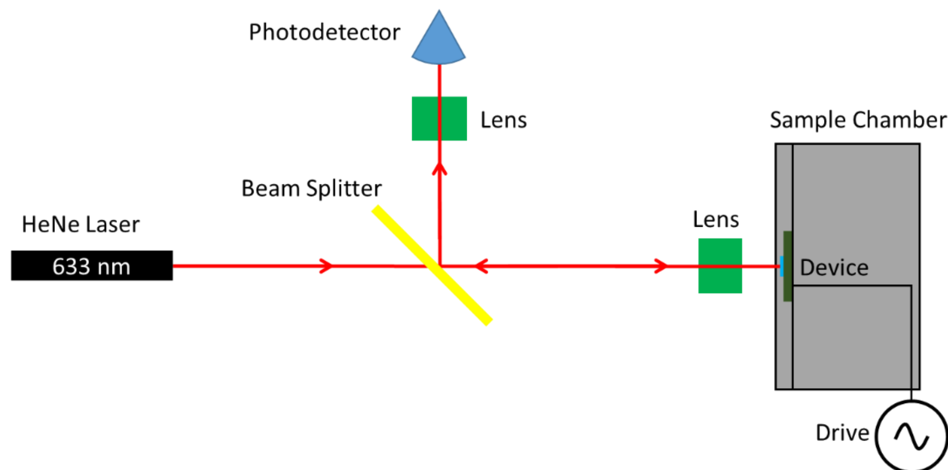

Figure 3-11 Acutation and detection scheme for the nonlinear beam measurement. The suspended device is mounted on a ceramic piezoelectric shaker. An AC voltage is applied to the shaker, providing a driving force for the device. The optical detection is performed using a 633 nm HeNe laser. The laser is aligned and reflects off of the doubly-clamped beam. The reflected photons are then sent to the photodetector using the beam splitter.

3.8 Measurement of Anharmonic Nonlinearity in NEMS Doubly-Clamped Beams

To probe the device's response in the nonlinear regime of mechanical response, each device was actuated with increasing strength from the linear regime until displacement ~25% beyond the onset of mechanical nonlinearity was achieved [13] (see Figure 3-12). Throughout, the optical interferometry measurements were performed in the near-linear regime. However, the interferometric response is intrinsically sinusoidal, so small residual deviations from linearity in the detected amplitude were carefully corrected [12]. For each drive strength, the mechanical

response was measured in the frequency domain. As previously mentioned, although the frequency corresponding to the maximum displacement amplitude is not precisely the nonlinear resonant frequency, in systems where the quality factor, Q, is large (e.g., $Q \gg 1$), the two frequencies are approximately the same. The frequency corresponding to the largest displacement amplitude was then recorded for each drive strength. The longitudinal speed of sound could then be deduced from the extracted displacement amplitudes and the resonant frequencies in the nonlinear regime using the method outlined above. (Figure 3-13) Formally, the regime of nonlinear response is delineated as the regime beyond the $1\ dB$ compression point, where the signal is more than $1\ dB$ lower than the expected signal from a purely linear response [14, 15].

The nonlinear resonant frequency measurement was corrected for any frequency drifts by measuring the linear mechanical response immediately prior to each nonlinear resonant frequency measurement. Due to frequency drifts, the linear resonant frequency changes over time, which is included in our measured frequency shift due to nonlinear effects. By subtracting out the drift in the linear resonant frequency, any measured frequency shift from the nonlinear measurement is purely due to the effects of the additional stress from large displacement.

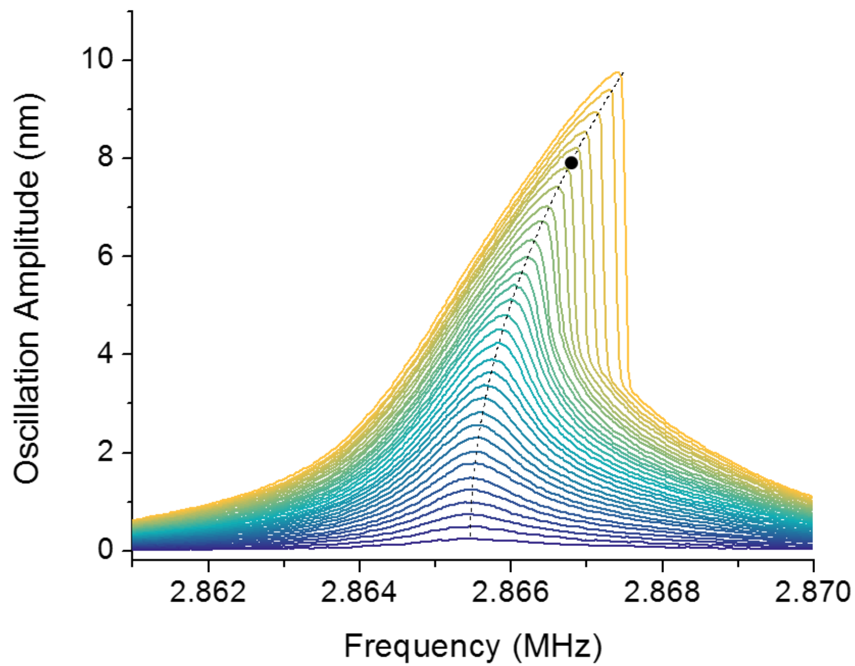

Figure 3-12 Mechanical response of the doubly-clamped silicon beam in the frequency domain as the actuation level increases from low (purple) to high (yellow). The black dot denotes the point formally defined as delineating the onset of the nonlinear regime (see text). At low actuation, the resonant response is simply a Lorentzian. As the actuation increases, the resonant frequency shifts upward due to nonlinear term in the equation of motion and the resonant frequency increases until the displacement reaches the critical amplitude, where the solution to the differential equation governing the system is multivalued. The dotted line is the fitted backbone curve of the resonant frequencies at the various actuation forces.

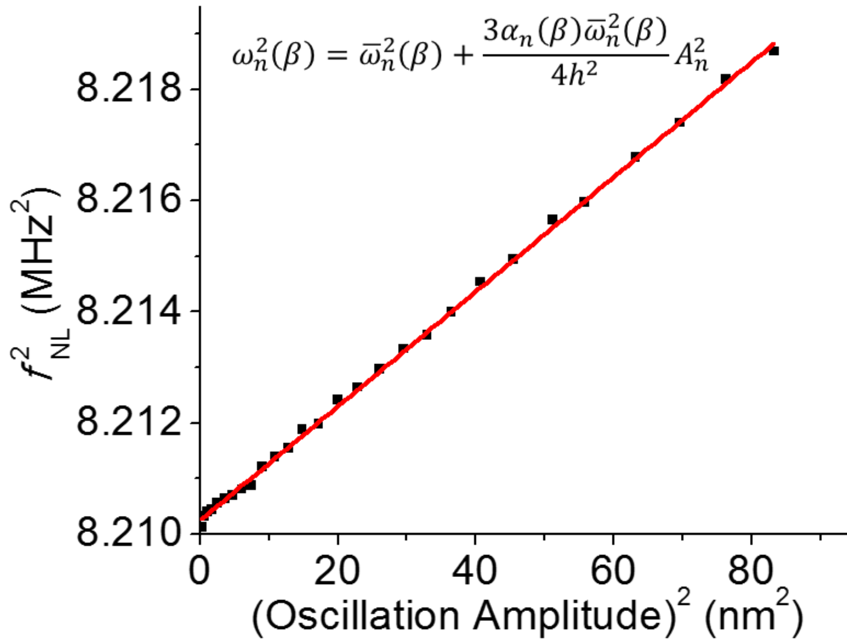

Figure 3-13 Plot of the frequency detuning as expressed by the square of the nonlinear response versus the oscillation amplitude. The linear least squared fit of Eq. 3-7 is denoted by the red line. The error bars are smaller than the size of the square used to represent each data point.

Silicon is an anisotropic crystal, hence the longitudinal speed of sound depends upon crystallographic orientation. Accordingly, the sound velocity within a single-crystal NEMS beam will depend upon its orientation with respect to the crystallographic axes. For a beam fabricated from (100) silicon wafer, we write the effective sound speed as $v_{l,\hat{k}}$, where

$$\frac{1}{v_{l,\hat{k}}^2} = \frac{1}{v_{l,\langle 100\rangle}^2} - 3\left(\frac{1}{v_{l,\langle 100\rangle}^2} - \frac{1}{v_{l,\langle 111\rangle}^2}\right)\sin^2 2\theta. \qquad \text{Eq. 3-12}$$

Here, the subscript $v_{l,\hat{k}}$ refers to the longitudinal speed of sound along the beams respective to crystallographic orientation; $\hat{k}$ is the direction in the (100) plane, and θ is the angle between $\hat{k}$ and the $\langle 110 \rangle$ direction. Within the (100) plane, the silicon bulk longitudinal speed of sound varies from $8516\ \mathrm{m/s}$ in the $\langle 110 \rangle$ direction to $7477\ \mathrm{m/s}$ in the $\langle 100 \rangle$ direction [1, 16-18]. To demonstrate the validity of the measurement paradigm presented in this paper, small changes in silicon's longitudinal speed of sound caused by the anisotropic nature of the silicon crystal were measured.

Figure 3-14 presents the key results of the proposed measurement technique, where the longitudinal sound speed as a function of crystal orientation is shown. Specifically, the longitudinal speed of sound was measured on 10 separate devices fabricated in the (100) plane. The devices were oriented along angles spaced apart by increments of $15°$. Measurement for each of these orientations was performed on most of the devices twice. Fitting the measured data to Eq. 3-12, the longitudinal speeds of sound were determined to be $v_{l_{\langle 100 \rangle}} = 6721 \pm 82$ m/s and $v_{l_{\langle 111 \rangle}} = 9148 \pm 225\ \mathrm{m/s}$. These results, measured directly from the nanodevices (that is, "*in-situ*"), compare favorably with values of $v_{l_{\langle 100 \rangle}} = 7477\ \mathrm{m/s}$ and $v_{l_{\langle 111 \rangle}} = 8973\ \mathrm{m/s}$ established in the literature for bulk silicon (Table 3-2). The data fit well to the theoretical curve of angular dependence and the measured speeds of sound agree with bulk literature values between 2% and 10%.

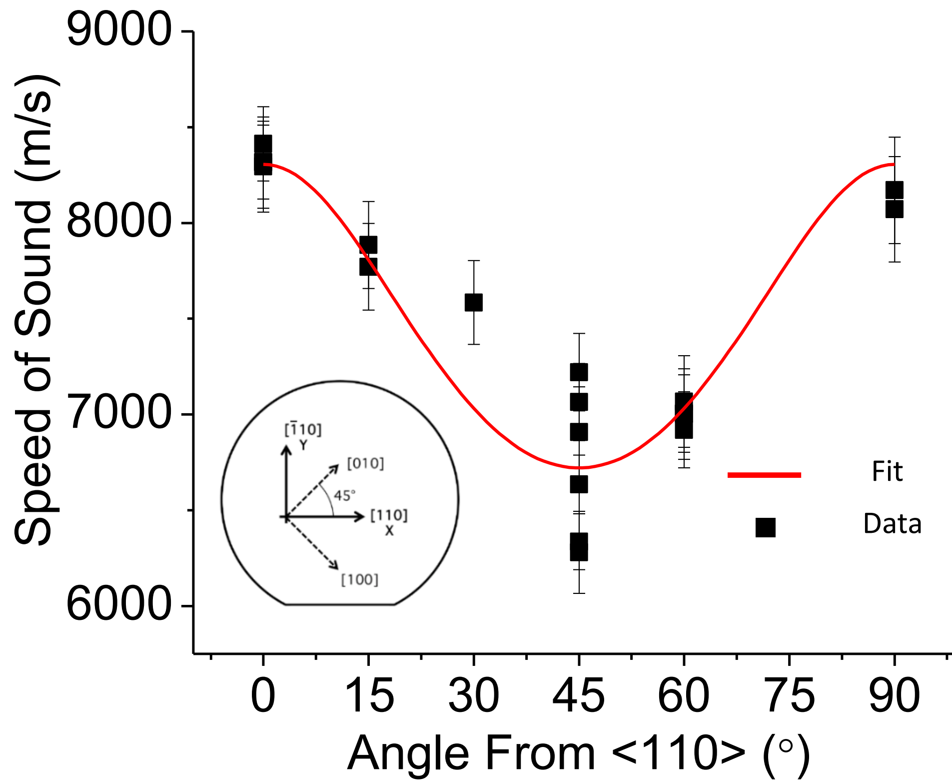

Figure 3-14 Experimental longitudinal speeds of sound as a function of crystal orientation within the silicon (100) plane. The x-axis shows the angle from the ⟨110⟩ direction within the (100) plane such that 0° corresponds to the ⟨110⟩ direction and 45° corresponds to the ⟨100⟩ direction. From the least squared fit (red), the speeds of sound for two independent crystal orientations are extracted; the two values are given in the inset table. From these two values, we can calculate the speed of sound for any crystal orientation.

	Measured	Bulk
$v_{l,100}$	$6721 \pm 82 \frac{m}{s}$	$7477 \frac{m}{s}$
$v_{l,111}$	$9147 \pm 225 \frac{m}{s}$	$8973 \frac{m}{s}$

Table 3-2 A comparison of the measured speeds of sound along the $\langle 100 \rangle$ and $\langle 111 \rangle$ directions to the expected bulk material values. The measured values are in good agreement with the bulk literature values to within 2% to 10%.

3.9 Summary

In this work we present a new methodology for extracting the longitudinal speed of sound and stress in a nanoelectromechanical beam *in-situ*, using the dynamics of doubly-clamped NEMS beams operating in the nonlinear regime. We have tested this new paradigm on identical silicon doubly-clamped beams fabricated along different crystal orientations, and have completely characterized the longitudinal speeds of sound in all orientations. The experimental values of the longitudinal speeds of sound were 6721 ± 82 m/s in the <100> direction and 9147 ± 225 m/s for the <111> direction, in close agreement with literature bulk values. While our demonstrations have solely employed doubly-clamped beams, the conceptual framework of this nonlinear analysis applies to all mechanical systems, e.g., cantilevers and membranes. We anticipate that this new methodology will facilitate nanodevice characterization and engineering.

3.10 Bibliography

1. McSkimin, H.J. and P. Andreatch, *Elastic Moduli of Silicon vs Hydrostatic Pressure at 25.0°C and −195.8°C.* Journal of Applied Physics, 1964. **35**(7): p. 2161-2165.

2. Allen, M.G., et al., *Microfabricated structures for the insitu measurement of residual stress, Young's modulus, and ultimate strain of thin films.* Applied Physics Letters, 1987. **51**(4): p. 241-243.

3. Diddens, I., et al., *Anisotropic Elastic Properties of Cellulose Measured Using Inelastic X-ray Scattering*. Macromolecules, 2008. **41**(24): p. 9755-9759.

4. Brand, O., et al., *Resonant MEMS: Fundamentals, Implementation, and Application*. 2015: Wiley.

5. Poncharal, P., et al., *Electrostatic Deflections and Electromechanical Resonances of Carbon Nanotubes.* Science, 1999. **283**(5407): p. 1513-1516.

6. Treacy, M.M.J., T.W. Ebbesen, and J.M. Gibson, *Exceptionally high Young's modulus observed for individual carbon nanotubes.* Nature, 1996. **381**(6584): p. 678-680.

7. Hocke, F., et al., *Determination of effective mechanical properties of a double-layer beam by means of a nano-electromechanical transducer.* Applied Physics Letters, 2014. **105**(13): p. 133102.

8. Haque, M.A. and M.T.A. Saif, *Deformation mechanisms in free-standing nanoscale thin films: A quantitative in situ transmission electron microscope*

study. Proceedings of the National Academy of Sciences of the United States of America, 2004. **101**(17): p. 6335-6340.

9. Bargatin, I., I. Kozinsky, and M.L. Roukes, *Efficient electrothermal actuation of multiple modes of high-frequency nanoelectromechanical resonators.* Applied Physics Letters, 2007. **90**(9): p. 093116.

10. Lifshitz, R. and M.C. Cross, *Nonlinear Dynamics of Nanomechanical and Micromechanical Resonators*, in *Reviews of Nonlinear Dynamics and Complexity*. 2009, Wiley-VCH Verlag GmbH & Co. KGaA. p. 1-52.

11. Timoshenko, S., *Theory of elasticity*. 2001: McGraw-Hill.

12. Hiebert, W.K., et al., *Optical interferometric displacement calibration and thermomechanical noise detection in bulk focused ion beam-fabricated nanoelectromechanical systems.* Journal of Micromechanics and Microengineering, 2010. **20**(11): p. 115038.

13. Kacem, N., et al., *Nonlinear phenomena in nanomechanical resonators: mechanical behaviors and physical limitations.* Mechanics & Industry, 2010. **11**(06): p. 521-529.

14. Postma, H.W.C., et al., *Dynamic range of nanotube- and nanowire-based electromechanical systems.* Applied Physics Letters, 2005. **86**(22).

15. Nayfeh, A.H. and D.T. Mook, *Nonlinear Oscillations*. 2008: Wiley.

16. Brantley, W.A., *Calculated elastic constants for stress problems associated with semiconductor devices.* Journal of Applied Physics, 1973. **44**(1): p. 534-535.

17. Kim, K.Y., R. Sribar, and W. Sachse, *Analytical and optimization procedures for determination of all elastic constants of anisotropic solids from group velocity data measured in symmetry planes.* Journal of Applied Physics, 1995. **77**(11): p. 5589-5600.

18. Wortman, J.J. and R.A. Evans, *Young's Modulus, Shear Modulus, and Poisson's Ratio in Silicon and Germanium.* Journal of Applied Physics, 1965. **36**(1): p. 153-156.

Chapter 4

EFFECT OF MODE SHAPES IN TWO-DIMENSIONAL MASS SPECTROMETRY AND INERTIAL IMAGING

In Chapter 1, we provided an overview of the many applications for mass spectrometry in geology [1-3], environmental science [4-6], forensics analysis [7-9], and proteomics [10-12]. In this chapter, we review the traditional methods of mass spectrometry and describe a new paradigm for performing mass spectrometry using NEMS that has been developed over the past decade at Caltech [13, 14]. We review the operating principles of NEMS mass spectrometry (NEMS-MS) and NEMS inertial imaging (NEMS-II) and their advantages over traditional mass spectrometry. We then describe the measurement setup used in this work, the devices employed, preliminary data, and current challenges encountered with the experiment that reflect on experimental complexities to be surmounted in the optimization of this method. In the last part of this chapter, we focus specifically on the mode shape of the NEMS and the critical role it plays in mass spectrometry and inertial imaging. We elucidate the deviation between the ideal mode shapes and the experimentally measured ones that arise with existing NEMS devices. We hypothesize the causes of these deviations and test possible sources of their origin. Lastly, we explore the effects of the mode shape deviation on the result of mass spectrometry and inertial imaging.

4.1 Overview and Motivation

In this section, we discuss some of the more common methods of mass spectrometry including time-of-flight measurement, magnetic sector mass analyzer, and a quadrupole [15], and the advantages and disadvantages of each.

One of the conceptually simplest methods for mass spectrometry is a time-of-flight measurement (Figure 4-1). The analyte is injected into a vacuum chamber from the fluid phase and ionized, typically using electrospray ionization [16, 17]. It then travels through a discrete acceleration region which results in different particles having different final velocities depending on the field and the charge-to-mass ratios of the various analytes. The separate species then travel at different velocities in the drift tube and arrive at the detector at different times [18, 19]. Given the duration of the particle in the tube and the length of the tube, the mass-to-charge ratio can be deduced.

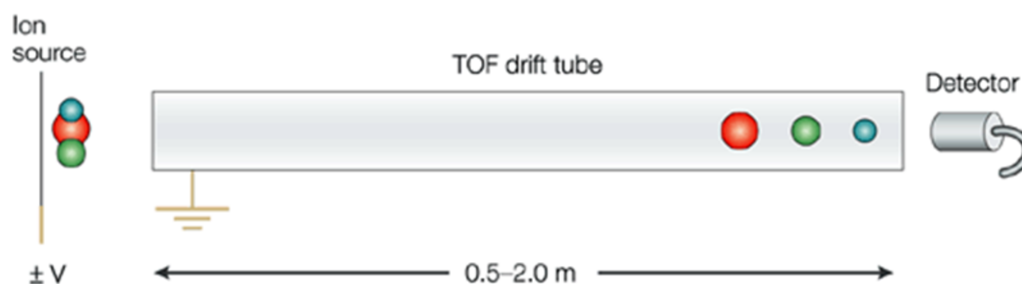

Figure 4-1 Time-of-flight measurement to perform mass spectrometry. The particles are charged and start on the left of the figure where they are accelerated through an electric field created by a DC voltage. The particle travels to the right and the duration of the particle in the tube is used to calculate the mass-to-charge ratio. Figure adapted from Glish, G.L. and R.W. Vachet, *The basics of mass spectrometry in the twenty-first century*. Nat Rev Drug Discov, 2003. **2**(2): p. 140-150. [15].

The magnetic sector mass analyzer provides another method of performing mass spectrometry (Figure 4-2). In this case the sample is also typically introduced by electrospray ionization and accelerated. In this case, the particle is accelerated in an electric field and a magnetic field is applied perpendicular to both the plane of analyte motion and the direction of the electric field. The Lorentz force, induced by analyte motion in the applied magnetic field, deflects the analyte according to its mass-to-charge ratio. The trajectories of the different analytes have different radii, depending upon the Lorentz force they experience. With a detector at a fixed position (Fig. 4.2), the magnetic field is swept to permit detection of species with different mass-to-charge ratios.

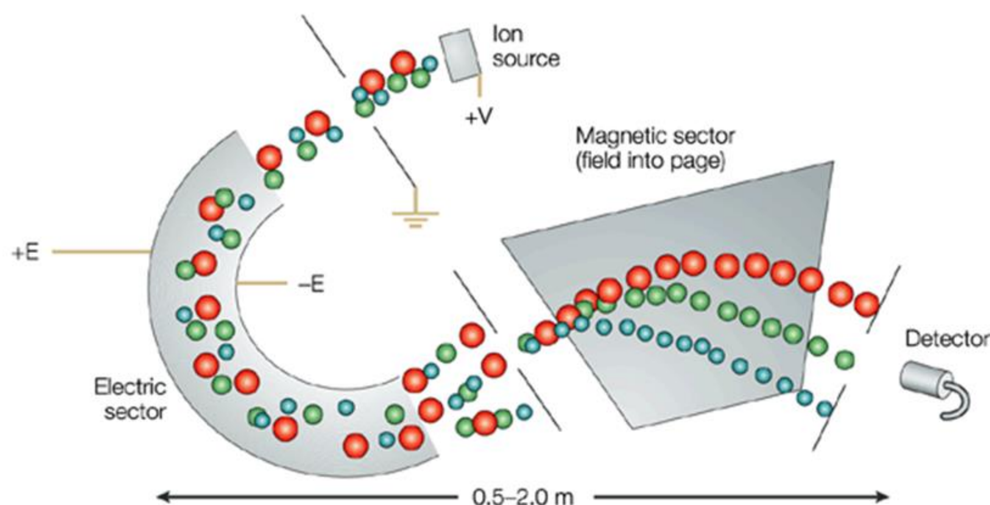

Figure 4-2 Magnetic sector mass analyzer. The particles are charged and start at the top of the figure where they are accelerated through an electric field created by a DC voltage. Due to the applied magnetic field, particles with different masses travel at a different velocity and thus have a different turn radius. By varying the strength of the magnetic field, samples of different mass-to-charge ratios are detected. Figure adapted from Glish, G.L. and R.W. Vachet, *The basics of mass spectrometry in the twenty-first century*. Nat Rev Drug Discov, 2003. **2**(2): p. 140-150. [15].

Typically, both the time-of-flight and the magnetic sector mass analyzers are large instruments, with dimensions usually between $0.5\ m$ and $2\ m$. This permits sufficient trajectory lengths to permit separation of species with sufficiently high resolution. To reduce the size of mass spectrometers, quadrupole spectrometry has been developed (Figure 4-3). A quadrupole consists of four parallel cylindrical metal electrodes. Each opposing electrode pair is connected electrically, and a radio frequency voltage with a DC offset is applied between each pair of rods; the rods being driven in antiphase. Ions travel down the quadrupole between the rods. Only

ions of a certain mass-to-charge ratio reach the detector for a given ratio of voltages; other ions have unstable trajectories and collide with the rods or are ejected from the interstitial space between them.

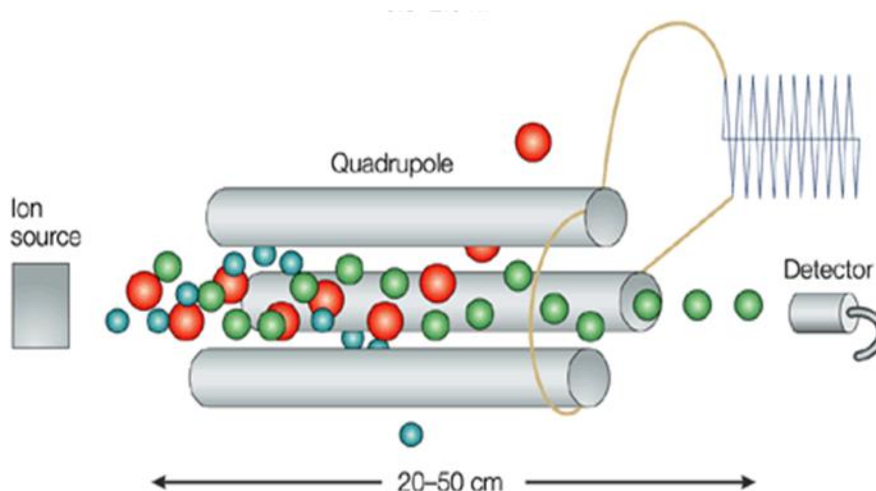

Figure 4-3 Diagram of quadrupole used in traditional mass spectrometry. The quadrupole is a set of four metal rods in parallel. In this figure, the fourth and the closest rod is not drawn so the ions are more easily seen. Opposing rods are connected electrically and the two pairs of rods have an RF and DC voltage offset. By tuning the frequency and amplitude of the voltage on the rods, only charged particles of a certain mass-to-charge ratio arrive at the detector. Charged particles of other mass-to-charge ratios collide with the rod or spin out of orbit and thus are eliminated. Figure adapted from Glish, G.L. and R.W. Vachet, *The basics of mass spectrometry in the twenty-first century*. Nat Rev Drug Discov, 2003. **2**(2): p. 140-150. [15].

These three mass spectrometry methods can provide excellent mass resolution; the best provide the ability to measure down to a small fraction of the

proton mass ($1.007\ amu \sim 1.007\ Da$). However, these methods typically lack sufficient dynamic range to measure large samples, exceeding several hundred kDa. Examples of species in this range are large protein complexes (membrane proteins, antibody isoforms, organelles, and viruses), which can range from $.05 - 100's$ of MDa. Existing forms of mass spectrometry also require charging (ionizing) the sample; for non-covalently bonded complexes this can compromise the integrity of the analytes and potentially induce their fragmentation.

NEMS-MS offers unique opportunities to overcome these limitations. NEMS-MS offers the ability of single molecule detection, and the analytes need not be ionized for analysis and detection. While there exists single ion detectors, the convolution of measuring the mass-to-charge ratio instead of a direct mass measurement makes it challenging to know accurately the mass of the single molecule for very large species that are in heterogeneous mixtures. NEMS-MS offers a large dynamic range (perhaps ~7 orders of magnitude or more), offering the ability to measure very large, as well as small, molecules. Current implementations of NEMS-MS permit measurement of molecules ranging in mass from $10^4\ Da$ to $10^9\ Da$. In the next section, we discuss the operating principal of how NEMS are employed for mass spectrometry.

4.2 Operating Principal of NEMS-MS and NEMS-II

In this section, we discuss how NEMS is used for mass spectrometry and inertial imaging. We begin our discussion with what is sometimes termed

"one-dimensional" (1D) NEMS mass sensing and mass spectrometry. We then generalize the theory of mass spectrometry to inertial imaging, the measurement of higher mass moments of an analyte. Lastly, we apply the theory of inertial imaging to 2D systems.

We begin by considering the case of mass sensing in one dimension. We treat a NEMS resonator – either a cantilever or a doubly-clamped beam – as a simple damped harmonic oscillator as described in Chapter 3. The resonant frequency of such a system, in the limit of low damping (high-Q), is given by:

$$\omega_0 = \sqrt{\frac{k_{eff}}{m_{eff}}}, \quad \text{Eq. 4-1}$$

where k_{eff} is the effective spring constant and m_{eff} is the effective mass for the mode under consideration. The effective spring constant takes into consideration the various mass-independent factors that we discussed in Chapter 3 (i.e. bending moment, compressive and tensile stress, effects of large deflections). The effective mass of the NEMS device is the scaling factor for determining the kinetic energy of the resonator when vibrating purely in the specific mode considered.

For the application of NEMS mass sensing, mass spectrometry, and inertial imaging, it is a good assumption that k_{eff} is constant since, for the most part, Young's modulus, stress, and oscillation amplitude of the device do not change during the experiment if the analyte is small compared to the dimensions of the

NEMS sensor. Following the analysis of Lifshitz and Cross [20], we determine m_{eff} by rewriting the equation of motion for a doubly-clamped beam resonator as:

$$\underbrace{\left(\rho S \int \Phi_n^2 dz\right)}_{m_{eff}} \underbrace{\frac{d^2 x}{dt^2}}_{\ddot{x}} + \underbrace{\left(EI \int \Phi_n''^2 dz\right)}_{k_{eff}} x = 0, \qquad \text{Eq. 4-2}$$

where $\rho S \int \phi_n^2 dz$ is the effective mass, m_{eff}, and $EI \int \phi_n''^2 dz$ is the effective spring constant, k_{eff}. Φ_n is the nth mode shape of the beam normalized such that the maximum amplitude of the beam is 1. One method of understanding the use of effective mass instead of the geometric mass, $m_{geo} = \rho S \int dz = \rho V$, is that we are treating the entire resonator vibrating in a specific pure mode as a point mass with a single displacement and a single velocity. In such a situation, not every part of the resonator contributes equally to the kinetic energy of the system. For example, the infinitesimal element at and near the nodes of a given mode provides a vanishing small contribution to the kinetic energy. This is consistent with the equation for m_{eff}, which is proportional to the square of the mode shape of the particular element along the length of the beam.

We now determine the effect of an increased effective mass due to the addition of an analyte on the resonant frequency. By Taylor expanding Eq. 4-1 to first order, assuming that k_{eff} is constant, and that the change in m_{eff} is small due to the analyte, we find

$$\frac{\Delta\omega}{\omega_0} = -\frac{1}{2}\frac{\Delta m_{eff}}{m_{eff}}. \qquad \text{Eq. 4-3}$$

By tracking the resonant frequency of the NEMS resonator, we can then determine that the fractional decrease in the resonant frequency is half the fractional increase in the mass of the device due to analyte accretion. If one monitors the resonant frequency in real time, mass accretion (adsorption events) are observed as sudden, discrete downshifts in resonant frequency. This simple equation above is the governing equation for NEMS mass sensing – at least in the limit of small analytes – and provides a conceptual foundation for NEMS-based mass spectrometry.

The above simple equation alone, however, is not sufficient for performing mass spectrometry, where we want to know the actual mass of the analyte. We use a doubly-clamped beam driven to its fundamental mode to illustrate this. A particle adsorbing at the center of the beam will have a significantly larger effect on the resonant frequency as compared to an identical particle that adsorbs near the clamping points or modal nodes of the resonator (Figure 4-4).

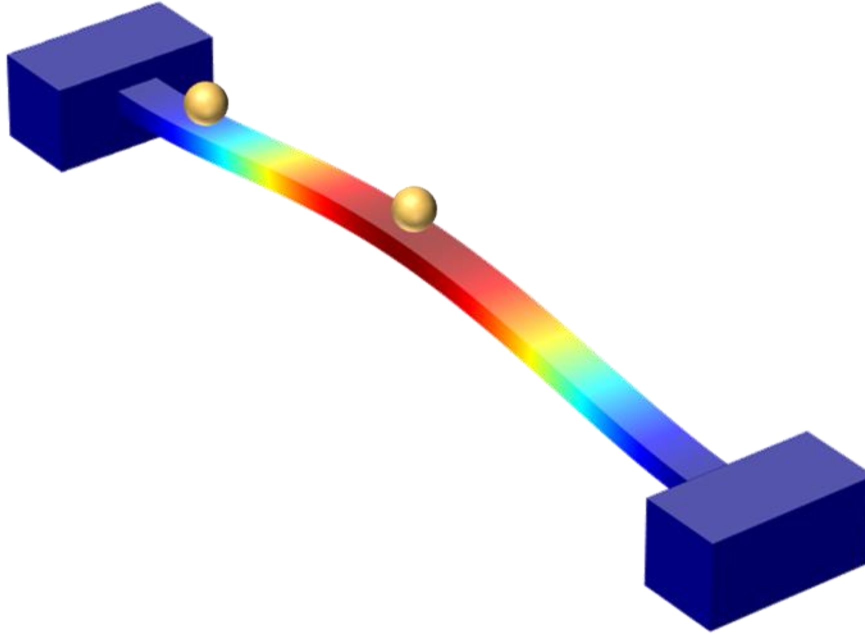

Figure 4-4 A doubly-clamped beam resonator driven to its fundamental mode. In this case particles adsorbing at the device center (modal antinode in this case) shift resonant frequency more than those adsorbing near the clamping points (or nodes in the case of higher mode resonances.) The color of the beam shows the relative amplitude of the beam with warmer colors (red) showing a larger displacement and cooler colors (blue) showing smaller displacement. A particle that lands near a red portion of the beam has a larger effect on the resonant frequency compared to a particle that lands near the blue portion of the beam.

Using the analogous formulation for the effective mass of the particle, we deduce that

$$\Delta m_{eff} = \int \mu_{particle}(z)\ \Phi_n^2 dz \qquad \text{Eq. 4-4}$$

$$\frac{\Delta\omega}{\omega_0} = -\frac{1}{2m_{eff}}\int \mu_{particle}(z)\ \Phi_n^2 dz, \qquad \text{Eq. 4-5}$$

where $\mu_{particle}(z)$ is linear mass density of the particle along the longitudinal direction of the beam. Since we are treating the particle as a point mass in this simple formalism, we can simplify Eq. 4-4 and Eq. 4-5 as

$$\Delta m_{eff} = m_{particle}\ \Phi_n^2(z_{particle}) \qquad \text{Eq. 4-6}$$

$$\frac{\Delta\omega}{\omega_0} = -\frac{1}{2}\frac{m_{particle}}{m_{eff}}\Phi_n^2\big(z_{particle}\big), \qquad \text{Eq. 4-7}$$

where $\phi_n(z_{particle})$ is the normalized displacement of the nth mode at the location, $z_{particle}$, along the beam at which the particle has adsorbed. The new governing equation has two unknowns, the mass of the particle and the location where the particle adsorbed. Since we cannot solve two unknowns with one equation, tracking only one resonant mode is insufficient to perform mass spectrometry in one dimension.

The first solution employed to surmount this challenge was to deposit analytes uniformly across the entirety of the NEMS device, and then deconvolve the response using the known position dependence (arising from mode shape) [21]. The major disadvantage of this method, however, is that it cannot be performed in real

time for individual particle adsorption events. In addition, this method of extracting the mass of the analyte involves fitting the data through a multidimensional minimization process that becomes very complex for multicomponent analyte mixtures.

Subsequently, a simpler solution to this challenge was developed that permits real time measurement of individual analytes. This approach involves tracking multiple normal modes of the NEMS resonator in real time [14]. By tracking the sudden fractional frequency change that occurs simultaneously in two normal modes for each adsorption event, we can solve the system of two equations comprised of Eq. 4-5 for each of the two normal modes, and deduce the precise location and mass of the analyte. This is the operating principal of 1D NEMS-MS.

Building upon 1D NEMS-MS by simultaneously tracking two normal modes, exact determination of the total mass and analyte absorption in real time can be deduced to first order [14, 22]. A natural question to ask is whether there is benefit to employing more than two normal modes. By Taylor expanding the mode shape squared about the mean position of the analyte, $\bar{z}$, we obtain:

$$\Phi_n^2(z)|_{z=\bar{z}} = \Phi_n^2(\bar{z}) + \left.\frac{\partial \Phi_n^2}{\partial z}\right|_{z=\bar{z}} (z-\bar{z}) + \left.\frac{\partial^2 \Phi_n^2}{\partial z^2}\right|_{z=\bar{z}} \frac{(z-\bar{z})^2}{2!} + \cdots. \quad \text{Eq. 4-8}$$

Substituting Eq. 4-8 into Eq. 4-5 and the definition of the mass of the particle, we find

$$\frac{\Delta\omega_n}{\omega_n} = -\frac{1}{2m_{eff}}\left\{\Phi_n^2(\bar{z})\int \mu_{particle}(z)\,dz + \left.\frac{\partial\Phi_n^2}{\partial z}\right|_{z=\bar{z}}\int \mu_{particle}(z)(z-\bar{z})dz + \left.\frac{\partial^2\Phi_n^2}{\partial z^2}\right|_{z=\bar{z}}\int \mu_{particle}(z)\frac{(z-\bar{z})^2}{2}dz + \cdots\right\} \quad \text{Eq. 4-9}$$

$$\frac{\Delta\omega_n}{\omega_n} = -\frac{m}{2m_{eff}}\left\{\Phi_n^2(\bar{z}) + \sum_{p=2}^{\infty}\frac{1}{p!}\left.\frac{\partial^p\Phi_n^2}{\partial z^p}\right|_{z=\bar{z}}\langle z^p\rangle\right\}, \quad \text{Eq. 4-10}$$

where $\langle z^p\rangle$ is the pth mass moment of the analyte. Following Eq. 4-10, by measuring the frequency shift for a multiplicity of normal modes provides the capability for measuring higher spatial moments of the analyte's mass density (in 1D); this is termed "inertial imaging" [13]. In the simplest case for $p = 2$, this set of equations reduces to

$$\begin{cases} \dfrac{\Delta\omega_1}{\omega_1} = -\dfrac{m}{2m_{eff}}\Phi_1^2(\bar{z}) \\ \dfrac{\Delta\omega_2}{\omega_2} = -\dfrac{m}{2m_{eff}}\Phi_2^2(\bar{z}) \end{cases}. \quad \text{Eq. 4-11}$$

Hence, using the change in the resonant frequencies in two normal modes permits the determination of the mass and location of the analyte. For $p = 3$, the set of equations becomes

$$\begin{cases} \frac{\Delta\omega_1}{\omega_1} = -\frac{m}{2m_{eff}}\left\{\phi_1^2(\bar{z}) + \left.\frac{\partial\Phi_1^2}{\partial z}\right|_{z=\bar{z}} \langle z\rangle\right\} \\ \frac{\Delta\omega_2}{\omega_2} = -\frac{m}{2m_{eff}}\left\{\phi_2^2(\bar{z}) + \left.\frac{\partial\Phi_2^2}{\partial z}\right|_{z=\bar{z}} \langle z\rangle\right\}, \\ \frac{\Delta\omega_3}{\omega_3} = -\frac{m}{2m_{eff}}\left\{\phi_3^2(\bar{z}) + \left.\frac{\partial\Phi_3^2}{\partial z}\right|_{z=\bar{z}} \langle z\rangle\right\} \end{cases} \quad \text{Eq. 4-12}$$

where z is the variance of the analyte, which represents its average length along the length of the beam. For each additional normal mode measured, successively higher mass moments (skewness, kurtosis, etc.) can be determined.

It is clearly interesting to inertially image the profile of each adsorbed analyte. To accomplish this a device with 2D modeshapes is required. To analyze this case, we extend the theory of 1D inertial imaging to 2D. Continuing in a spatial basis with Cartesian coordinates, Eq. 4-10 for 2D inertial imaging becomes:

$$\frac{\Delta\omega_n}{\omega_n} = -\frac{m}{2m_{eff}}\left\{\Phi_n^2(\bar{x},\bar{y}) + \sum_{p=2}^{\infty}\sum_{j=0}^{p}\frac{1}{(p-j)!\,j!}\left.\frac{\partial^p\Phi_n^2}{\partial x^{p-j}\partial y^j}\right|_{(x,y)=(\bar{x},\bar{y})}\langle x^{p-j}y^j\rangle\right\}. \quad \text{Eq. 4-13}$$

In direct analogy with the 1D case, the higher mass moments for absorbing analyte can be determined by measuring the sudden frequency shifts occurring (simultaneously) in additional 2D normal modes. Because of the presence of cross terms involving the transverse and longitudinal directions, determination of each additional mass moment requires an increased number of 2D normal modes.

Table 4-1 shows the number of normal modes required to calculate a particular mass moment in 1D and 2D inertial imaging.

Mass Moment	Relevance	Number of Normal Modes Needed in the 1D Case	Number of Normal Modes Needed in the 2D Case
Mean	analyte mass	2	3
Variance	adsorption position *(center-of-mass)*	3	6
Skewness	1st analyte shape moment	4	10
Kurtosis	2nd analyte shape moment	5	15

Table 4-1 Number of normal modes needed for each mass moment for 1D and 2D inertial imaging.

4.3 Devices and Analyte for 2D Inertial Imaging

In this section, we discuss the NEMS devices and the analyte for our 2D inertial imaging experiments. We begin with a discussion of the two different geometries of devices used in our experiments. Then we discuss the analytes employed and their preparation. Lastly, we discuss the tests performed on the analyte preparation process and analyze their results.

For the mass spectrometry and inertial imaging experiments discussed in this chapter, devices were fabricated from aluminum nitride (AlN) piezoelectric material similar to that employed for the AlN switches described in Chapter 2. However, the AlN piezoelectric stacks used in these experiments have slightly thinner device layers, with thicknesses, from top to bottom, of: $20\ nm\ Mo$, $50\ nm\ AlN$, $50\ nm\ Mo$, and $20\ nm\ AlN$. The fabrication process for these 2D plate devices that are clamped on all sides is similar to the one shown in Figure 2-15.

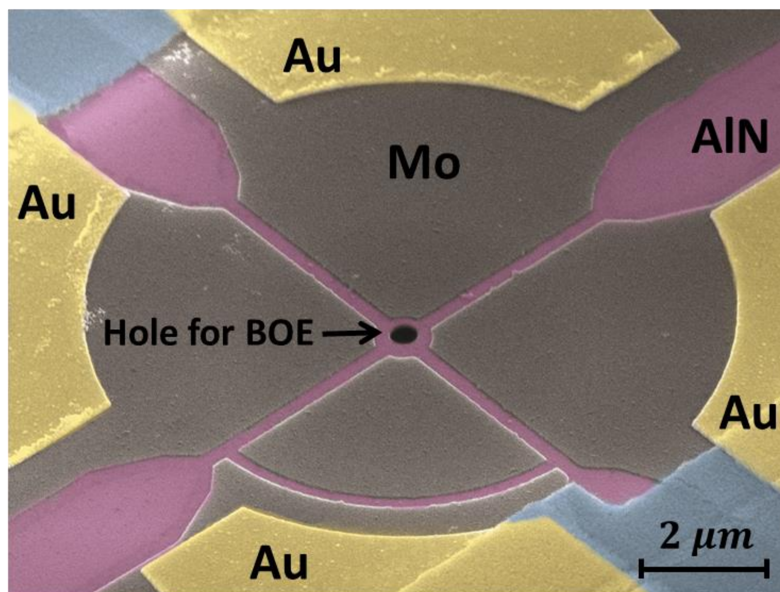

Figure 4-5 Scanning electron micrograph of a representative circular plate AlN device of ~4.7 μm in diameter. There are cuts at various locations on the top Mo layer to electrically isolate the various top electrodes. The hole in the center of the plate is for BOE to reach the silicon dioxide under the device layer to suspend the device. The devices are similar to those made in Matheny, *et al.* [23].

There are two major differences between these plate-like (membrane) devices and cantilever and doubly-clamped beam devices: 1) For the plates, parts of the top molybdenum layer are etched away to electrically isolate multiple areas from one another. 2) The plate devices we employ are clamped on all sides; no silicon dioxide is exposed to the etchant for suspending the device. Accordingly, an extra step is performed in the fabrication process: holes of $\sim 300\ nm$ were etched through the entire device layer to the silicon dioxide so that BOE could be used to suspend the device. (Figure 4-5)

The first device geometry we have employed is a circular plate, with a thickness of $140\ nm$ and diameter of approximately $4.7\ \mu m$. While the precise diameter is not known because it was not possible to determine where the etching of the silicon dioxide (the undercut) terminated, we estimated the diameter using the etch rate and duration, and then compared the modal frequencies obtained with finite element methods (FEM). Fitting a multiplicity of modes permits direct extraction of the residual stress in these devices. The geometric mass of the circular plate was determined to be $\sim 4.74\ \times 10^{-14}\ kg$, or $2.86\ \times 10^{13}\ Da$.

The second geometry of devices employed was $140\ nm$ thick plates with an approximately square geometry. The deduced length of each side is $26\ \mu m$, again comparing the resonator's measured modal frequencies to FEM simulations. To etch these devices, an array of holes separated by $\sim 2\ \mu m$ were etched through the structural layer of the device (that is, through the plate). Subsequently a circular area

of silicon dioxide was etched under each hole using a BOE. While this fabrication method results in the edges of the square plate being multiple connected arcs, with precise geometries that depend on the etching rates and duration, the sides of the square are approximately straight to within $300\ nm$. FEM simulations show that it is sufficient to treat this as a square plate for our analyses. The deduced geometric mass of the square plates employed is $\sim 6.38 \times 10^{-13}\ kg$, or $3.84 \times 10^{14}\ Da$. (Figure 4-7)

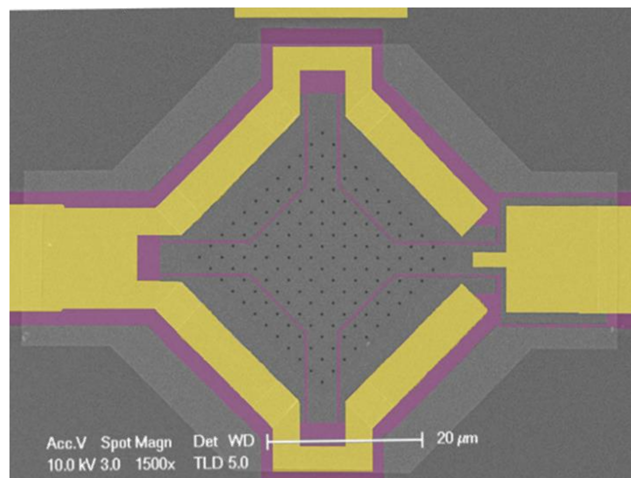

Figure 4-6 Scanning electron micrograph of a representative square AlN plate device with $\sim 26\ \mu m$ sides. The purple line on the device is the cut in the top Mo layer (light gray) so that there are two electrically isolated electrodes. An array of holes were etched through the device layer so that the BOE can etch the silicon dioxide in order to suspend the device. While this means that the clamping edge of the device was not perfectly straight, given the etch rate and the dimensions of the entire plate, we believe it is sufficient to approximate this as a square plate.

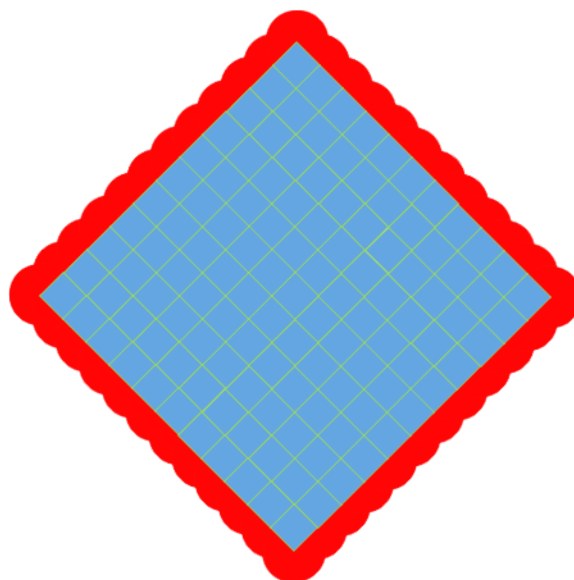

Figure 4-7 Diagram of a representative square AlN plate device with $\sim 26\ \mu m$ sides. Outline of a representative square plate. The intersection of the green lines represents the hole etched for the suspension of the device. The outer extent of the red area is where we think the etch stopped based on the etch rate and the etch duration. The maximum deviation in the sides' width is $300\ nm$.

For these experiments we employed gold nanoparticles (GNP) as analytes. These were purchased from Sigma Aldrich, Inc. with various diameters, ranging from $5\ nm - 80\ nm$. Table 4-2 shows the concentration and mass of the GNPs as a function of their diameters specified by the manufacturer. All GNP solutions were centrifuged to increase the as-purchased concentration by about 20 times. This did not result in observable aggregation of the nanoparticles.

GNP Diameter	GNP Mass		Concentration
5 nm	$1.264 \times 10^{-21}\ kg$	$0.7615\ MDa$	$5.47 \times 10^{13}\ mL^{-1}$
10 nm	$1.012 \times 10^{-20}\ kg$	$6.092\ MDa$	$5.98 \times 10^{12}\ mL^{-1}$
20 nm	$8.093 \times 10^{-20}\ kg$	$48.74\ MDa$	$6.54 \times 10^{11}\ mL^{-1}$
30 nm	$2.731 \times 10^{-19}\ kg$	$164.5\ MDa$	$1.79 \times 10^{11}\ mL^{-1}$
40 nm	$6.474 \times 10^{-19}\ kg$	$389.9\ MDa$	$7.15 \times 10^{10}\ mL^{-1}$
50 nm	$1.264 \times 10^{-18}\ kg$	$761.5\ MDa$	$3.51 \times 10^{10}\ mL^{-1}$
80 nm	$5.179 \times 10^{-18}\ kg$	$3.119\ GDa$	$7.82 \times 10^{9}\ mL^{-1}$

Table 4-2 Mass and concentration of gold nanoparticles of various diameters as purchased from Sigma Aldrich, Inc.

The GNP solutions are suspended in a proprietary salt listed as "citrate buffer", as purchased from Sigma Aldrich, Inc. The purpose of the buffer is to prevent the GNPs from aggregating. For our mass spectrometry and inertial imaging experiments, we performed buffer exchange where we added de-ionized water to the GNP solution to dilute the buffer solution, then centrifuged it to remove the supernatant. The filter used in the centrifugation process has holes that are large enough to allow salt particles in the buffer to pass through, but small enough to keep the GNPs in the solution. The buffer exchange allows us to measure the GNP without confounding effects of the salt. In our experiments, we performed this buffer exchange process multiple times, until the salt concentration was diluted by about 1000 times.

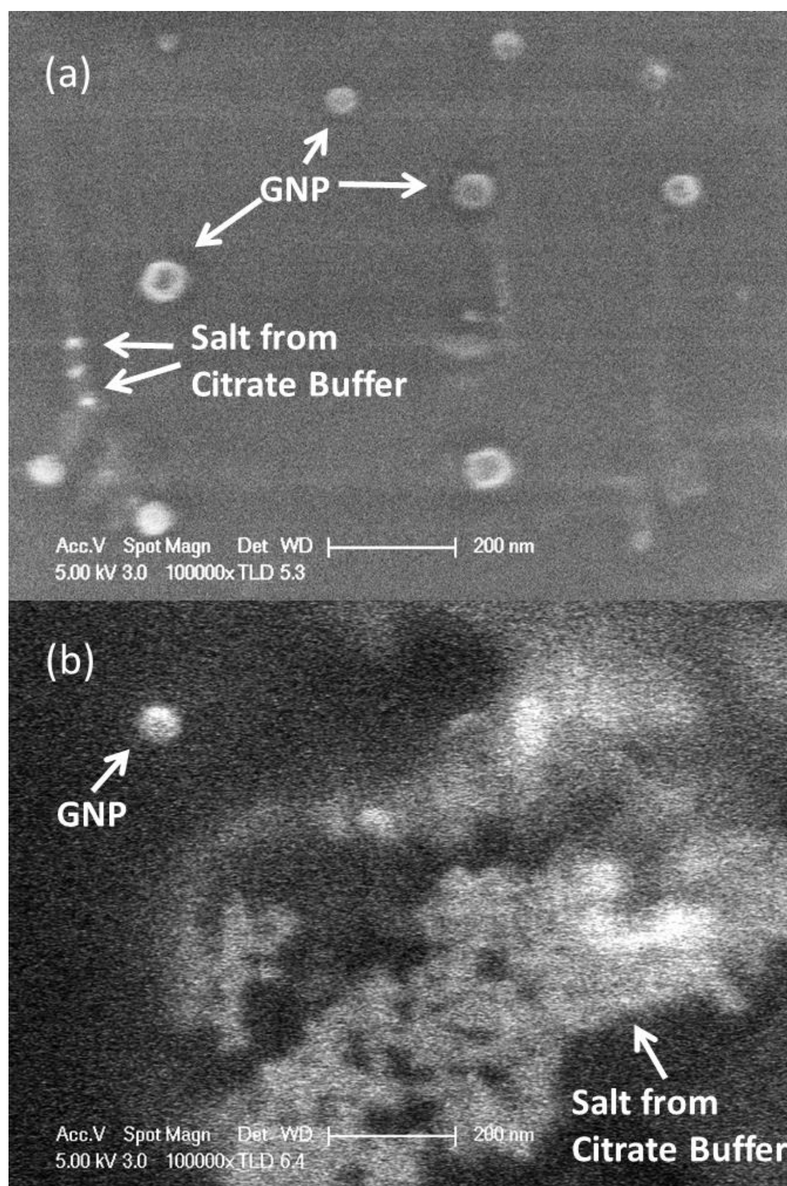

Figure 4-8 Scanning electron micrograph of the effect of citrate buffer on the GNP solution. (a) After buffer exchange, GNP does not aggregate and there are very few salt particles. (b) Without buffer exchange, GNP does not aggregate, but there are many salt particles.

To confirm that the GNPs did not aggregate after the buffer exchange procedure, a GNP solution after buffer exchange and concentration was pipetted onto a silicon wafer and imaged under the SEM. A control GNP solution, with the concentration step but without buffer exchange, was pipetted onto another silicon wafer. Figure 4-8 shows the comparison of the two samples of GNP with and without buffer exchange. In the sample where buffer exchange was performed, no signs of aggregating of the GNP were seen even after the solution was concentrated by 20 times. There are a few small particles that we believe is salt residue from the citrate buffer. In the sample where buffer exchange was not performed, while there was also no obvious aggregation of the GNPs, there appeared to be a much larger amount of small particles. These were similar to those seen in the sample with buffer exchange.

In our experiments, after the GNP solution had been concentrated and buffer was exchanged out, the resulting solution was pipetted onto either a glass slide or a titanium foil – depending on the type of analyte delivery method in NEMS-MS/II analysis. In both cases, the substrate was cleaned with acetone then isopropyl alcohol and dried using dry nitrogen. The substrate was placed on a hot plate of $80℃$ for the pipetting of the GNP solution. Drops with $2.5\ \mu L$ of the solution were pipetted onto the substrate, one drop at a time. After drying, the outer edges of the drop appear to have a darker coloration and contain higher concentrations of GNPs due to the "coffee ring effect" [24]. To ensure there was sufficient number of GNPs near the center of the substrate, we waited for each drop to dry on the hot plate, prior to

pipetting the following drop. Typically, a total of $250\ \mu L$ of GNP solution was pipetted onto an area of $\sim 2\ cm\ \times 2\ cm$ on the substrate.

4.4 Experimental Setup for 2D Inertial Imaging

In this section, we discuss the two different analyte delivery methods and the two setups used for our inertial imaging experiments. While our two analyte delivery methods are interchangeable between the two setups, we have used each setup with only one delivery method in our experiments. We will discuss the various methods of actuation and detections compatible with each setup and conclude with the advantages and disadvantages of each of these setups.

The two analyte delivery methods used in our experiments are matrix-assisted laser desorption/ionization (MALDI) [25] and laser-induced acoustic desorption (LIAD). For both of these delivery methods, the analyte – concentrated GNP in these experiment – was deposited onto a substrate and placed into the vacuum chamber along with the device.

For MALDI, the analyte is typically embedded in a matrix on a substrate, such as a glass slide in our experiment (Figure 4-9a). While there are a wide variety of methods of sample preparation and materials used for the matrix, the purpose of the matrix is for the absorption of radiation from an ultraviolet (UV) laser pulse. This laser pulse triggers ablation and desorption of the matrix with the analyte, in an emitted plume. During this ablation, the analyte and matrix both become ionized.

While GNPs have been themselves shown to be an effective matrix [26], we employed GNPs alone as both the matrix and the analyte in our experiment. A $2.5\ \mu m$, $377\ nm$ UV pulsed laser (SRS model NL100) was used to desorb the GNPs. Traditional MALDI uses a metal or glass plate as the substrate and the laser pulse is incident from the matrix side of the substrate. In our experiment, we used a glass slide as our substrate and the laser pulse traversed through the glass slide and was subsequently absorbed by the GNP. While the analyte does not change shape or fragment from the ionization, given that we used robust GNPs as our analytes, ionization of analyte in typical MALDI could compromise the integrity of more sensitive analytes such as biological molecules.

Our second method of analyte delivery, LIAD, however, is highly compatible with biological molecules because it does not require ionizing the analyte (Figure 4-9b), at least for subsequent NEMS analysis. (The low ionization yield for LIAD compromises its utility for conventional mass-to-charge detection.) Instead of having a matrix absorb the laser pulse energy, LIAD operates with a metal foil substrate, and the laser is incident from the backside (that is, the opposite side from the location of the analytes). When the laser pulse arrives at the metal foil, the energy is quickly absorbed by the foil and results in an acoustic wave that propagates through the thickness of the foil. When this pulse of acoustic energy reaches the other side of the foil, the resulting shock wave desorbs analytes from the foil. This results in a plume of analytes ejected from the front (analyte) surface of the foil. Since this method is purely acoustic, the analytes are largely unionized in this process. In our experiments,

we used a $12.7\ \mu m$ thick titanium (Ti) foil with $500\ nm$ aluminum (Al) sputtered on as the LIAD substrate. The Al side of the substrate is adhered to the glass slide using Emerson and Cuming Stycast 1266 A/B epoxy. A $355\ nm$ Minilite II Continuum Class 4, Q-switched neodymium-doped yttrium aluminum garnet (Nd-YAG) laser was used to desorb the GNP.

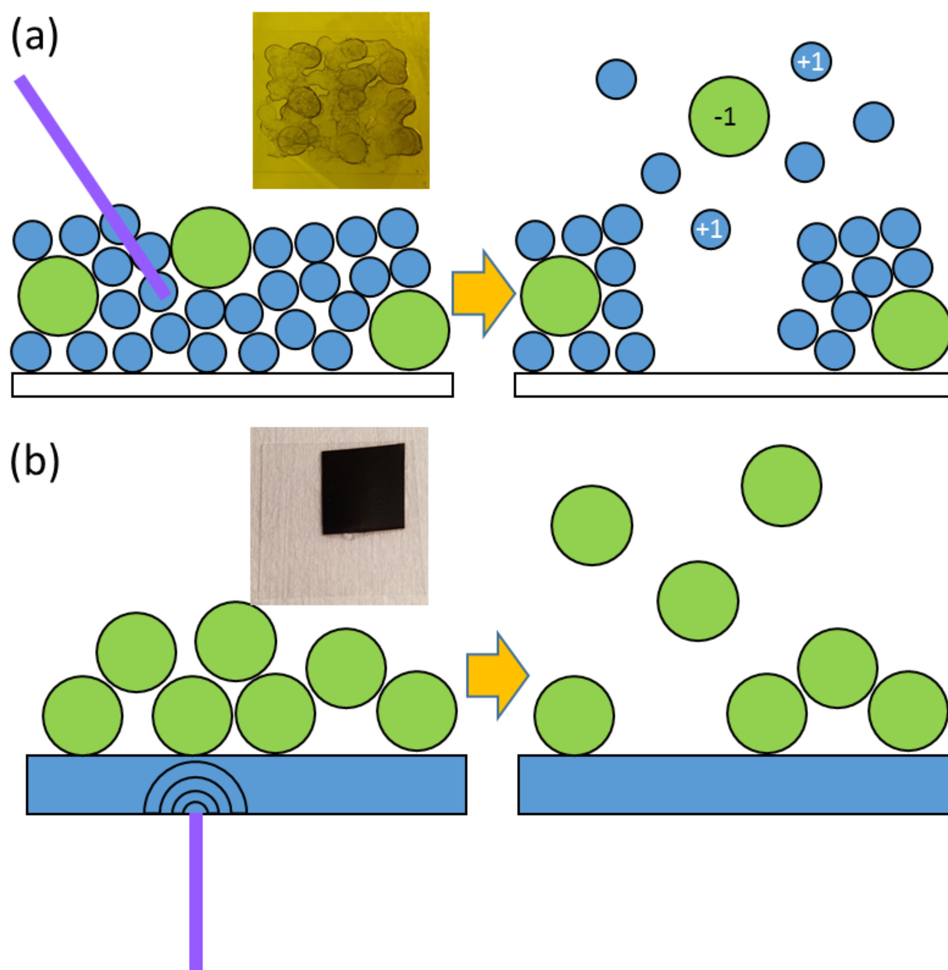

Figure 4-9 Diagram showing desorption using MALDI and LIAD. (a) In MALDI, the laser pulse ablates and desorbs the matrix and the analyte. The ablation causes some analyte and matrix to be ionized. (inset) Actual image of the GNP deposited onto the glass slide. The darker area is the result of the deposition of the GNP. (b) In LIAD, the laser pulse creates an acoustic pulse in the metal foil. When the acoustic wave reaches the other side of the foil, analytes are desorbed from the foil. (inset) Actual image of the Ti/Al foil glued onto the glass slide. The deposition on the GNP is not visible after the liquid has dried.

In our experiment, we used two different vacuum chamber setups. While both MALDI and LIAD can be used in either set up as long as the corresponding UV laser was used, we used each of the two set ups exclusively for each of the delivery methods. Thus, we will refer to the two setups as the MALDI setup and the LIAD setup.

For the MALDI setup, we designed and machined a vacuum chamber similar to that used in the nonlinear beam measurement in Chapter 3. Figure 4-10 shows an overview of the MALDI set up. Similar to the setup in Figure 3-11, a quartz window provides a direct line-of-sight optical path to the device that is used for NEMS displacement detection by laser interferometry. In addition, the apparatus includes a bracket for mounting the MALDI sample slide at a 30° angle to the device (Figure 4-11). The quartz window in the front of the sample chamber was also larger compared to that employed in the setup for the nonlinear experiment (Figure 3-11). This accommodated an additional optical path for the UV laser, permitting GNP desorption from the MALDI substrate. The UV laser spot on the MALDI substrate was moved by a focusing lens mounted on a three-dimensional motorized kinematic mount. While this allowed the UV laser to raster the entire MALDI substrate, only the irradiation of small area on the MALDI substrate by the UV laser (*i.e.*, the locations of the deposited spots) results in GNP to desorb.

The MALDI setup permits both electrical actuation and both electrical and optical detection of the NEMS sensor. Through its eight electrical ports, the AlN

device in the MALDI setup was either driven using piezoelectric actuation of the AlN device or mechanical actuation by mounting the NEMS device on a piezoelectric shaker. NEMS device motion was detected either by optical interferometry or by piezoelectric detection of the AlN device.

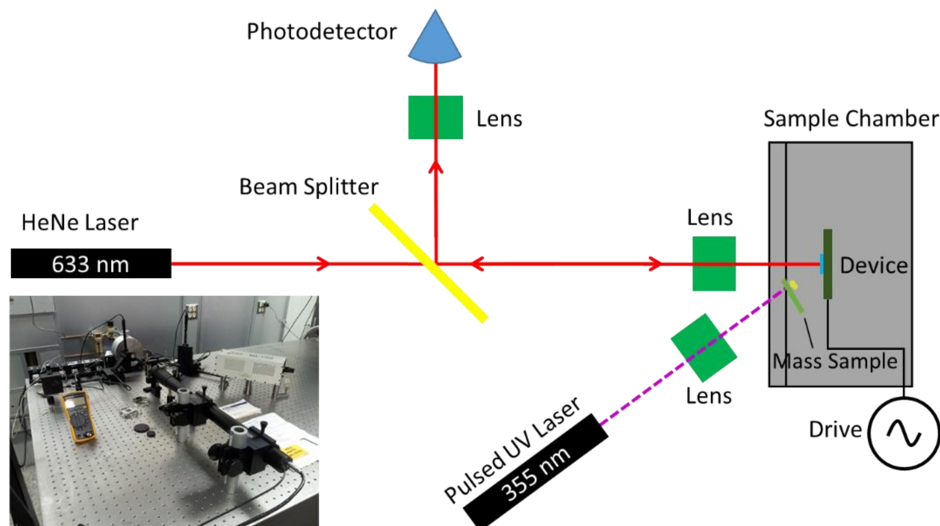

Figure 4-10 Actuation, detection, and deposition scheme in the MALDI setup. A 633 nm helium-neon (HeNe) laser is aligned with the device and the reflected signal is sent to the photodetector through a beam splitter. A 355 nm SRS NL100 UV pulsed laser is mounted at 30° to the HeNe laser to desorb the GNP from the MALDI slide. The MALDI slide is mounted also at 30° angle to the device. The focusing lenses for both the HeNe laser and the pulsed UV laser are mounted on three-dimensional kinematic mounts for steering the laser beams onto the device and MALDI substrate, respectively. (inset) Actual image of the MALDI setup.

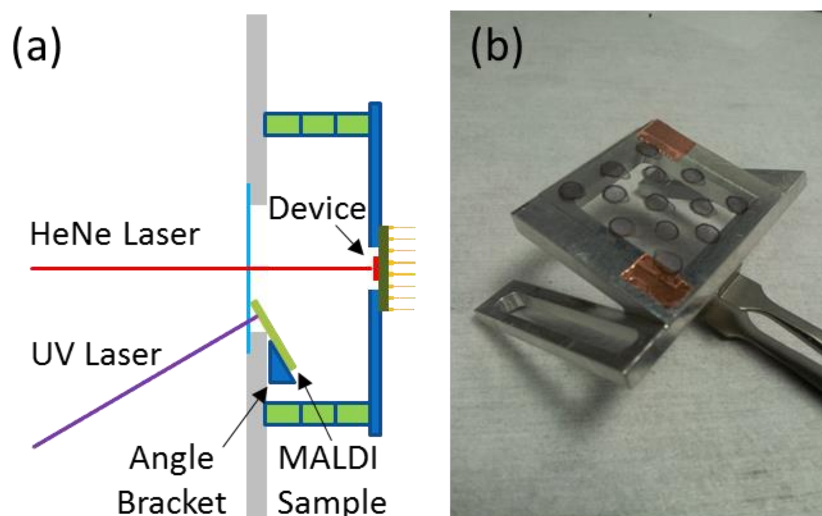

Figure 4-11 Close up of the MALDI deposition system. (a) A diagram of the front of the sample chamber (gray) with the quartz window (light blue). The quartz window allows a direct line-of-sight from the HeNe laser (red) to the device and the UV laser (purple) to the MALDI sample. The UV laser causes a plume of GNP to be desorbed from the MALDI sample and onto the device. (b) A MALDI sample with GNP mounted onto the angle bracket. The two brown rectangles are pieces of copper tape to adhere the MALDI glass slide onto the angle bracket. The dark circular spots are the deposited GNPs.

Compared to our MALDI setup, our LIAD set up was simpler but bigger. It was simpler because it did not have to accommodate a direct line-of-sight optical path for a detection laser (Figure 4-12). The only laser utilized in this setup was the UV pulsed laser. Unlike the MALDI setup where a lens was mounted on a motorized kinematic mount to steer the laser beam, our LIAD setup had a three-dimensional motorized stage inside the chamber to position the LIAD slide with respect to the

incoming laser and the device. This allows us to raster the entire LIAD slide. Similar to the MALDI setup, our LIAD setup also has eight electrical ports both for piezoelectric actuation and detection of the AlN device and for piezoshaker actuation.

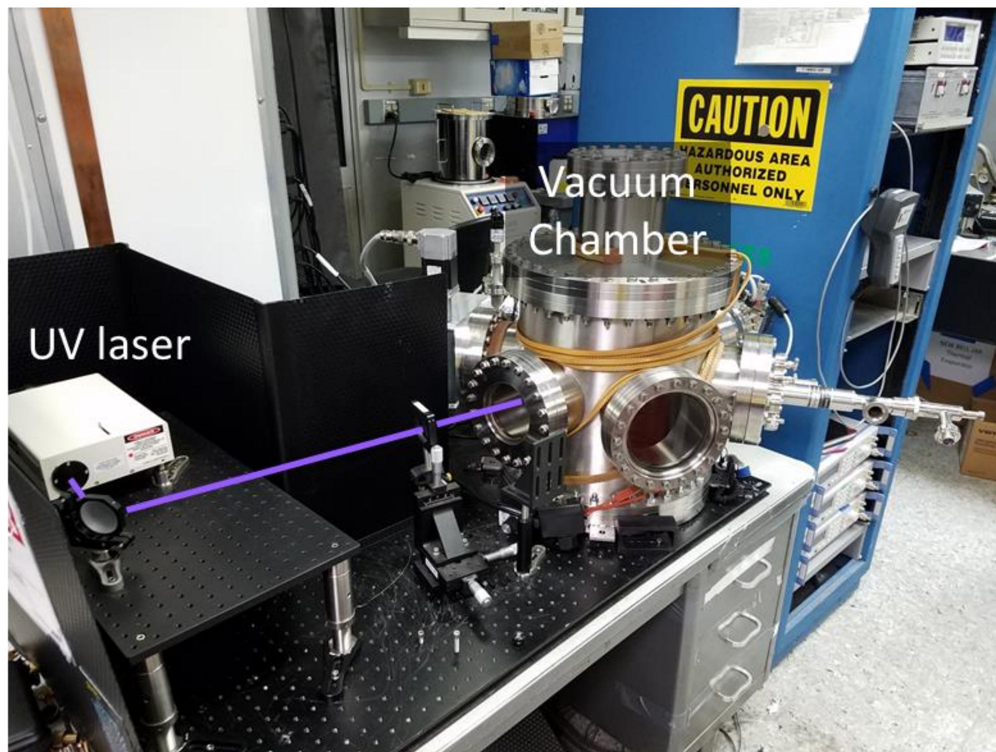

Figure 4-12 Photograph of our LIAD setup. A $355\ nm$ Minilite II Continuum Class 4, Q-switched Nd-YAG laser was used to deposit GNP from the LIAD substrate. Purple line is drawn into the photograph to represent the UV laser path.

In both of the MALDI and LIAD setups, the resonant frequency of the device is tracked using a phase-locked-loop (PLL). From Section 3.5 Experimental Determination of Resonant Frequency, we approximated the resonant frequency as the frequency with the maximum amplitude. With PLL detection, once the initial

resonant frequency, ω_0, and the quality factor of the device are measured, the post-deposition resonant frequency is approximated to first order by measuring the change in phase, $\Delta\phi$, of the resonator driven at ω_0:

$$\omega = \omega_0\left(1 + \frac{1}{2Q}\Delta\phi\right). \qquad \text{Eq. 4-14}$$

The system was then driven at the new resonant frequency.

In our experiment using the MALDI setup, each normal mode was driven by a signal generator (HP model 8648B). The optical interferometry signal from the photodetector was then sent to an RF lock-in amplifier (SRS model 844) with the reference signal coming from the signal generator. The measured change in phase from the lock-in amplifier was then employed to numerically calculate the new resonant frequency, which then was updated in the signal generator. When three modes were tracked, two-way power splitters/combiners (Mini-Circuits model ZFSC-2-1+) were used to combine the signal from the signal generator and to split the signal from the photodetector. When six modes were driven, six-way power splitters/combiners (Mini-Circuits model ZFSC-6-1+) were used. A low noise amplifier (Miteq model AU-1442) was connected to the output of the device. All communications between equipment and computer were through general purpose interface bus (GPIB) connections. Figure 4-13 shows a schematic of the PLL for three normal modes.

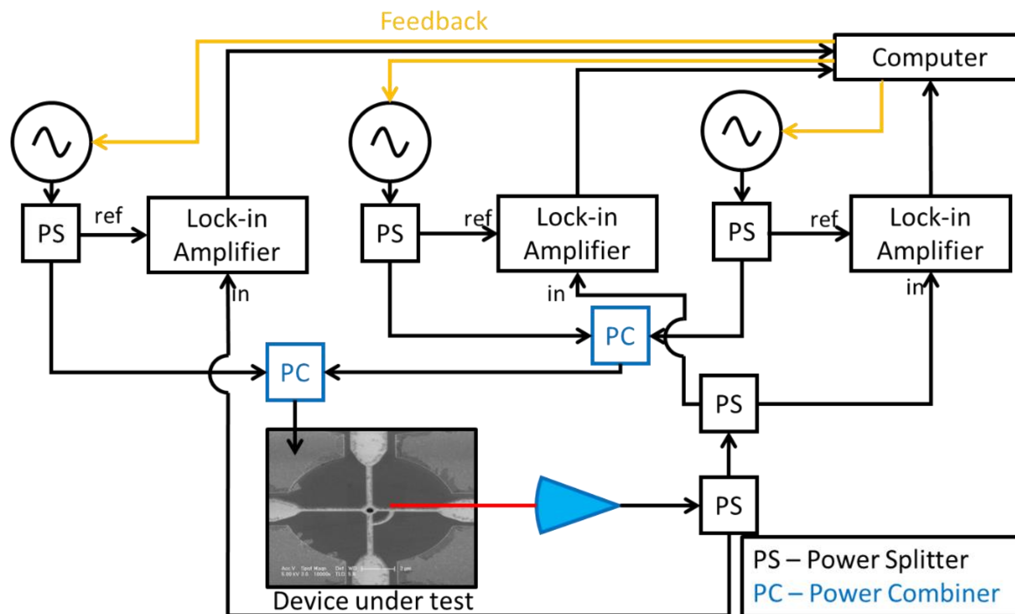

Figure 4-13 Schematic of the phase-locked-loop (PLL) employed to track three normal modes of the NEMS sensor (device under test). Three HP 8648B signal generators sent signals to the device through Mini-Circuits® ZFSC-2-1+ power combiners. The photodetector signal from the laser interferometer was split through Mini-Circuits® ZFSC-2-1+ power splitters to the SR844 RF lock-in amplifiers with the reference signal coming from the signal generators. The measured phase was then used to calculate the new resonant frequency for the signal generators.

Using independent microprocessor-controlled signal generators, lock-in amplifiers, and other instrumentation involves latency in communicate with the controlling computer. In order to minimize such delays, measurements performed with the LIAD setup were carried out with a custom data acquisition unit previously engineered by our group (ASYGN d-Box). The ASYGN d-Box is an integrated system with signal generator, lock-in amplifier, and PLL hard-wired using field-

programmable gate array (FPGA). Comparing the PLL loop time constant of ~ 5 seconds using our separate signal generators, lock-in amplifiers, and computer, the d-Box provides a small loop time constant of $\sim 100\ ms$.

4.5 Preliminary 2D NEMS-MS and NEMS-II Data

In this section, we present our preliminary 2D NEMS-MS and NEMS-II data from the circular and square plates, using both the MALDI and LIAD setups. We start with the results obtained with circular NEMS resonators using the MALDI system, then discuss the inertial imaging results from the square NEMS resonators using the LIAD system. We also discuss the challenges associated with each of these experiments.

We begin with the preliminary results from our mass spectrometry experiment with circular plate, $\sim 4.7\ \mu m$ in diameter, using the MALDI setup. We actuated the device using a piezoshaker mounted under the NEMS device and detected the signal optically. The lowest three resonant frequencies measured for this device were $94.2\ MHz$, $191.6\ MHz$, and $191.9\ MHz$. Based on FEM, the next lowest normal mode frequency expected would be $\sim 312.9\ MHz$. Since much of our equipment in this experiment was rated for up to $\sim 200\ MHz$, we used only the first three normal modes, which are sufficient to perform 2D NEMS-MS to solve for analyte mass and the two-dimensional coordinates of the position of adsorption. While the $191.6\ MHz$ and $191.9\ MHz$ resonant modes should have the same frequencies because they are degenerate, nonidealities in the fabrication process (e.g.,

one direction not etched as much as the other) broke the device symmetry and the mode degeneracy (Figure 4-14). These minor imperfections in the fabrication process, however, turned out to be advantageous in our experiments. While the two resonant frequencies are slightly different, their resonant peaks proved to be within a linewidth of each other. Accordingly, frequency tracking using PLL proved challenging because the tracked frequency would periodically jump to the nearby frequency because of random fluctuations in the system.

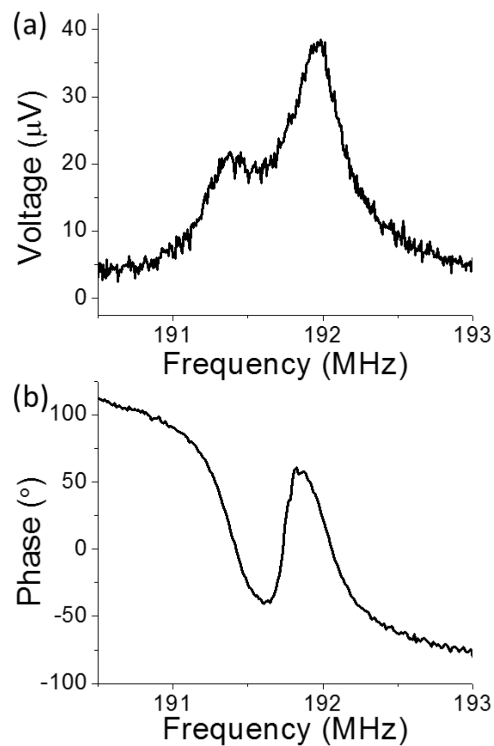

Figure 4-14 Amplitude and phase responses of the first degenerate mode for the circular plate NEMS resonator. The two resonant frequencies are within a linewidth of one another, making PLL challenging.

Due to the challenges in tracking the degenerate modes, in our MALDI experiment with circular NEMS resonators, we tracked only the fundamental mode and one of the degenerate modes. We recorded two simultaneous frequency jump events, one of which is more obvious than the other (Figure 4-15). For the first event, we recorded a frequency jump of $3.6\ kHz$ and $11.8\ kHz$ for the fundamental and higher mode, respectively. With this approach we cannot determine the exact location and mass of the particle because we solely track the frequency shift in two normal modes. With this information, we determine that the GNP was at least $18\ nm$ in diameter. The GNPs used in this experiment were $\sim 20\ nm$ and the diameters deduced from the data are consistent with this value.

For the second event observed in this device, the frequency shift in the fundamental mode was not as obvious. While it was possible that the frequency downshift in the higher mode came from the PLL losing lock with the higher mode and locking onto the other degenerate mode, it was not likely the case because upon zooming into the data, we saw a frequency downshift in the fundamental mode at the same time that the frequency jump takes place in the higher mode (Figure 4-15b). One of the reasons the second event was less obvious in the fundamental mode was because the frequency downshift was smaller (e.g., due to the particle landing close to a nodal feature). Another reason was the fundamental frequency happened to be drifting downward at the time of the second event.

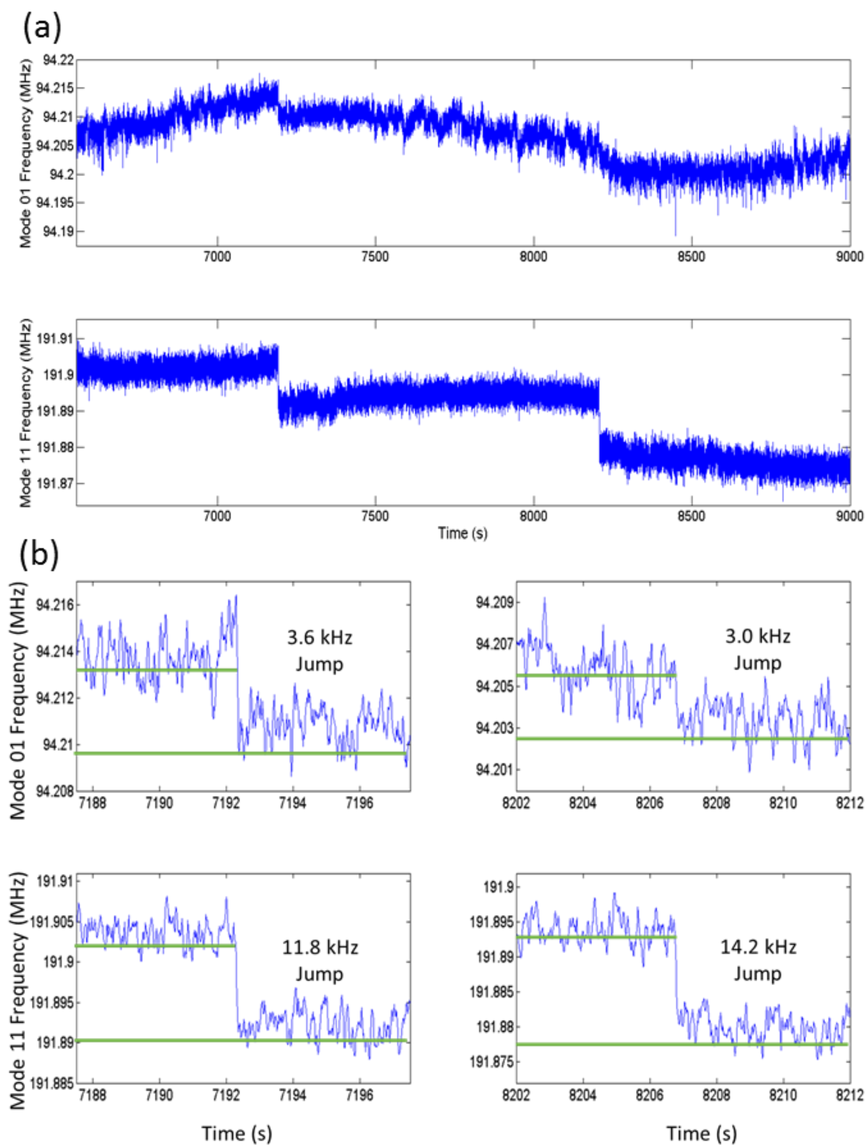

Figure 4-15 Mass spectrometry data showing two mass loading events using a circular AlN plate with MALDI. (a) We track two modes: fundamental mode at 94.2 MHz and one of the degenerate modes at 191.9 MHz and the two events took place at 7192 second and 8207 second. (b) Zoomed in plot of the frequency jumps.

To verify analyte desorption from the substrate and their subsequent deposition onto the device, we performed the following tests. First we observed the MALDI sample under the microscope (Figure 4-16). In dark areas we confirmed the presence of GNPs, which only appeared after depositing of drops of concentrated GNP solution and not after depositing drops of de-ionized water. After the experiment, the slide showed lines of lighter coloration. These lines arose where the UV laser desorbed GNPs from the substrate.

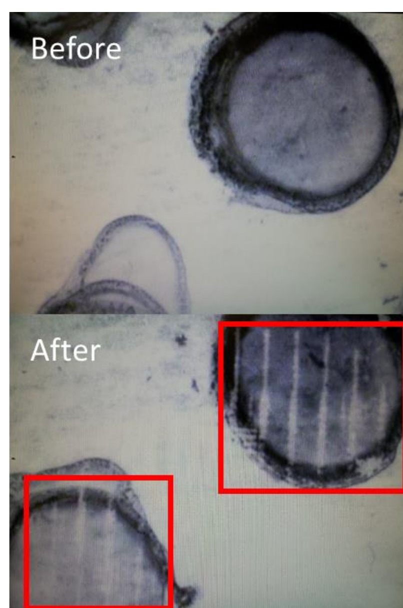

Figure 4-16 Optical image of the GNP on the MALDI slide before and after the mass deposition. The dark areas correspond to areas with GNP. A darker coloration means a higher concentration of GNP. After the deposition, lines of lighter coloration (within the red boxes) appear. These are areas where the UV laser desorbed the GNP.

In addition to imaging the MALDI substrate, we also imaged the device with a scanning electron microscope (SEM) to verify the GNP deposition. Comparing the SEM images before and after deposition (Figure 4-17a, b), there were additional bright spherical objects, consistent with our expectations for metallic objects. High resolution scans over these bright spots confirmed particle diameters of $\sim 22\ nm$, as expected (Figure 4-17c).

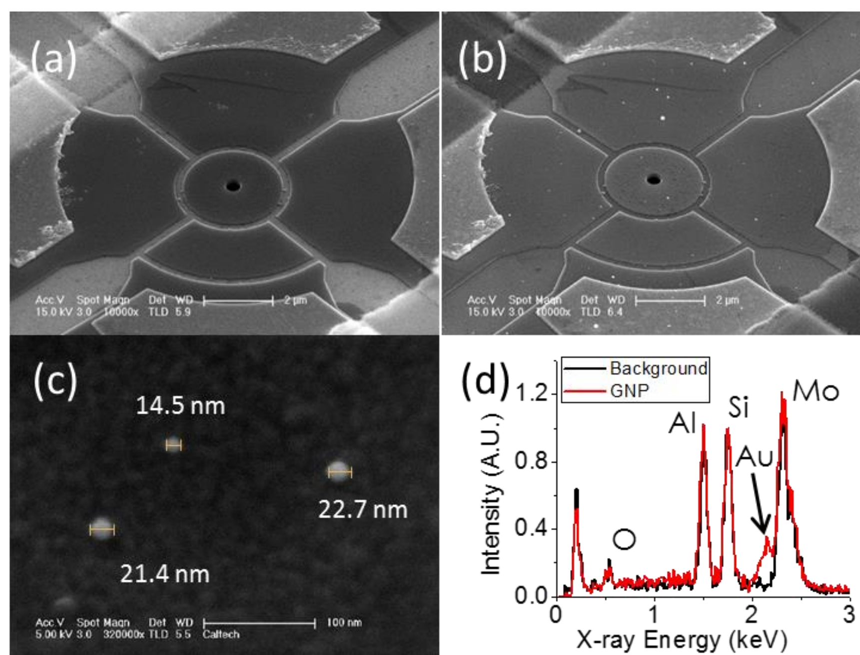

Figure 4-17 Verification of GNP deposition using scanning electron microscopy and energy dispersive x-ray spectroscopy (EDX). (a-b) Scanning electron micrographs (SEM) of the AlN circular device before (a) and after (b) GNP deposition. (c) SEM of the actual GNP to verify their sizes. (d) EDX of the device and on the GNP particles. The Au peak is only observed at the location of the adsorbed nanoparticles.

Utilizing energy dispersive x-ray spectroscopy (EDX) in the scanning electron microscope, two areas on the AlN device were analyzed: one with and one without these bright spherical particles. Figure 4-17d compares the results of the EDX analysis from these two areas. In both spectrograms, the energy peaks corresponding to oxygen, aluminum, silicon, and molybdenum were present. The sole difference between the two spectrograms was the additional energy peak at $2.2\ keV$ for the area with the spherical particles, which corresponds to emission from gold. The EDX analysis of the device, along with SEM of the device and optical imaging of the MALDI slide, provided conclusive evidence that GNPs were desorbed from the MALDI substrate onto the device.

While our circular resonator NEMS-MS measurements using MALDI showed promising results with GNPs deposited on the device, we only detected two events and were able to measure mass loading in only two modes. For NEMS-II, it is necessary to measure additional modes, preferably with many more events to allow statistical analysis. Because of this, we switched to the larger $26\ \mu m\ \times 26\ \mu m$ square plate NEMS resonators that permitted measurements of additional modes. With these larger devices, the fabrication process itself seemed to break the expected mode degeneracy, and non-degenerate resonances more than a linewidth apart were obtained. With these devices, we also employed the LIAD setup, which permitted more analyte desorption. In these experiments we employed the ASYGN d-Box readout that enabled tracking of additional modes at a reasonable speed with a smaller set of electronic instrumentation. Piezoelectric actuation and detection were

employed in these measurements. Piezoelectric actuation efficiencies for several of the modes we investigated were extremely small; we chose six resonant modes providing the largest signals and small backgrounds. Specifically, normal modes with the following resonant frequencies were employed: $6.95\,MHz$, $17.3\,MHz$, $17.4\,MHz$, $25.4\,MHz$, $32.6\,MHz$, and $53.2\,MHz$.

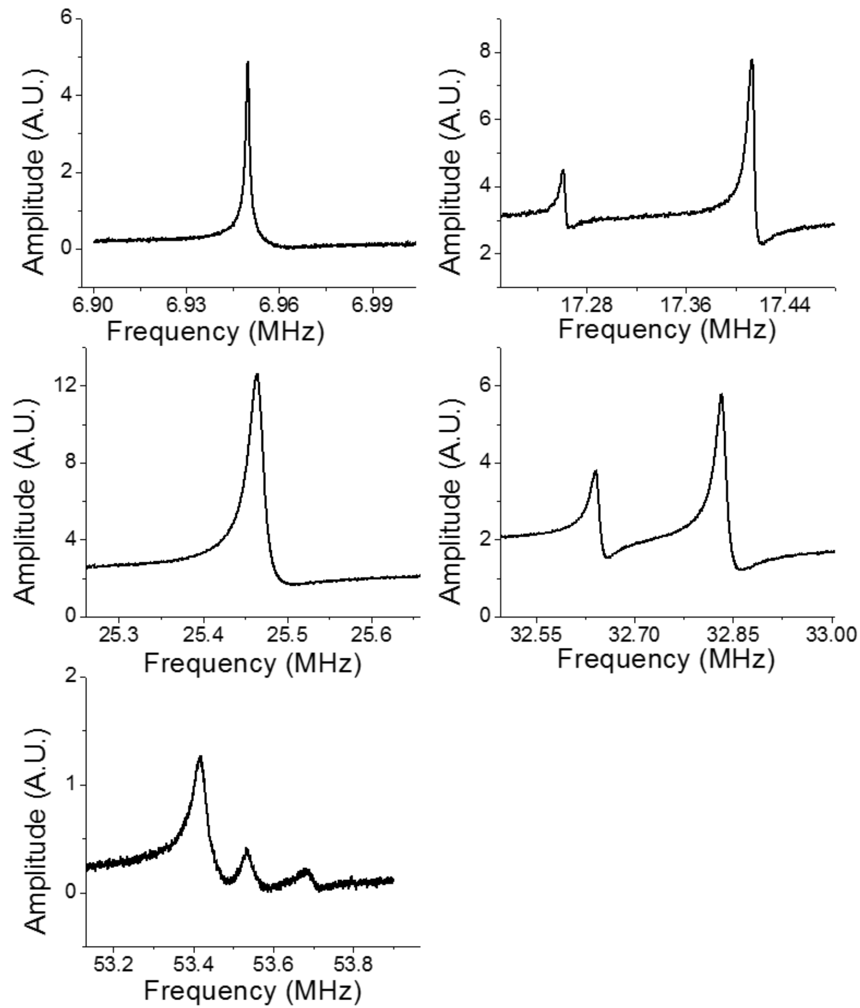

Figure 4-18 Amplitude responses of the normal modes for the square NEMS resonator using piezoelectric actuation and detection.

Two different sizes of GNPs, $40\,nm$ and $80\,nm$ in diameter, were deposited using LIAD. The base system pressure was $10^{-9}\,torr$ before the start of experimentation. Using the ASYGN d-Box to measure and track each of the modes, we followed six normal modes simultaneously using a PLL loop time constant of $100\,ms$. After deposition of both types of particles, the device was imaged using an SEM and the presence of GNPs of $\sim 40\,nm$ and $\sim 80\,nm$ in diameter was confirmed (Fig. 4-18).

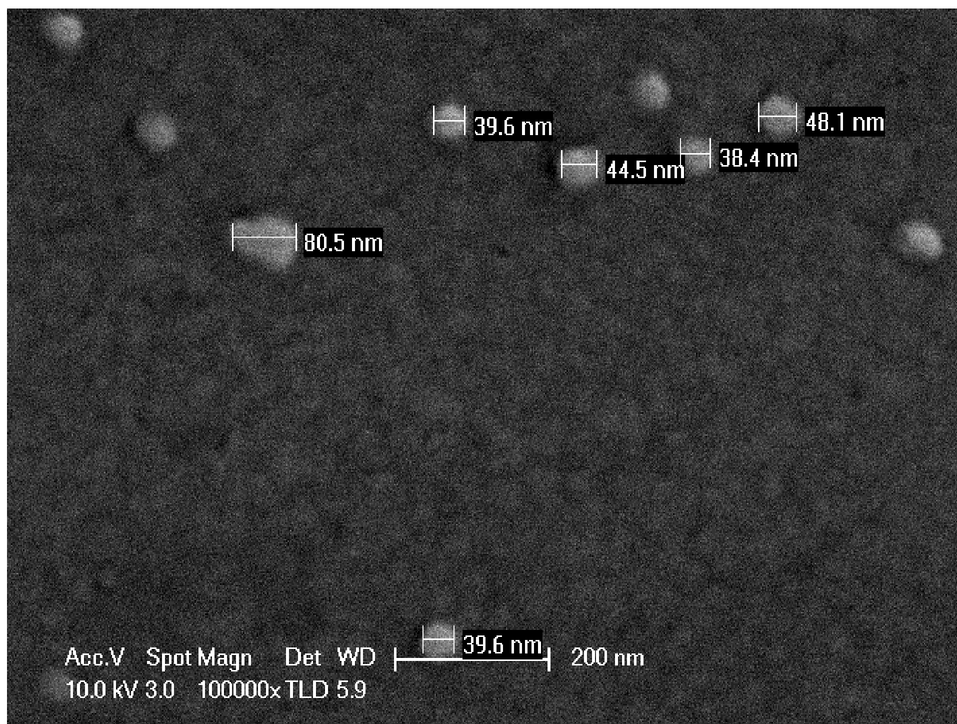

Figure 4-19 Scanning electron micrograph of the AlN square plate after deposition with GNP.

In the first experiment, we used the $40\,nm$ diameter GNPs and sent five laser pulses, one second apart, to the LIAD sample. This corresponded to the three clear

frequency downshifts in Figure 4-20. The frequency downshifts in each of the six modes occurred simultaneously, signifying that this resulted from the mass loading of the device. The frequency shifts from the lower $17\ MHz$ modes were not as obvious due to high frequency fluctuations. The discreteness of the jumps shows that the frequency changes arose from adsorption induced by the laser pulses.

Similarly, in the second experiment, we used $80\ nm$ diameter GNPs and delivered five laser pulses to the GNP-laden LIAD substrate, again one second apart. Figure 4-21 presents the frequency downshifts observed in this experiment. Similar results from three frequency downshifts were observed, corresponding to mass deposition from the three laser pulses. Table 4-3 and Table 4-4 summarize the results from the two experiments. Using the method in Section 4.2 Operating Principal of NEMS-MS and NEMS-II, the calculated diameters of the GNP were $\sim 40 - 50\ nm$ and $\sim 80 - 120\ nm$ and are in good agreement with our expected sizes.

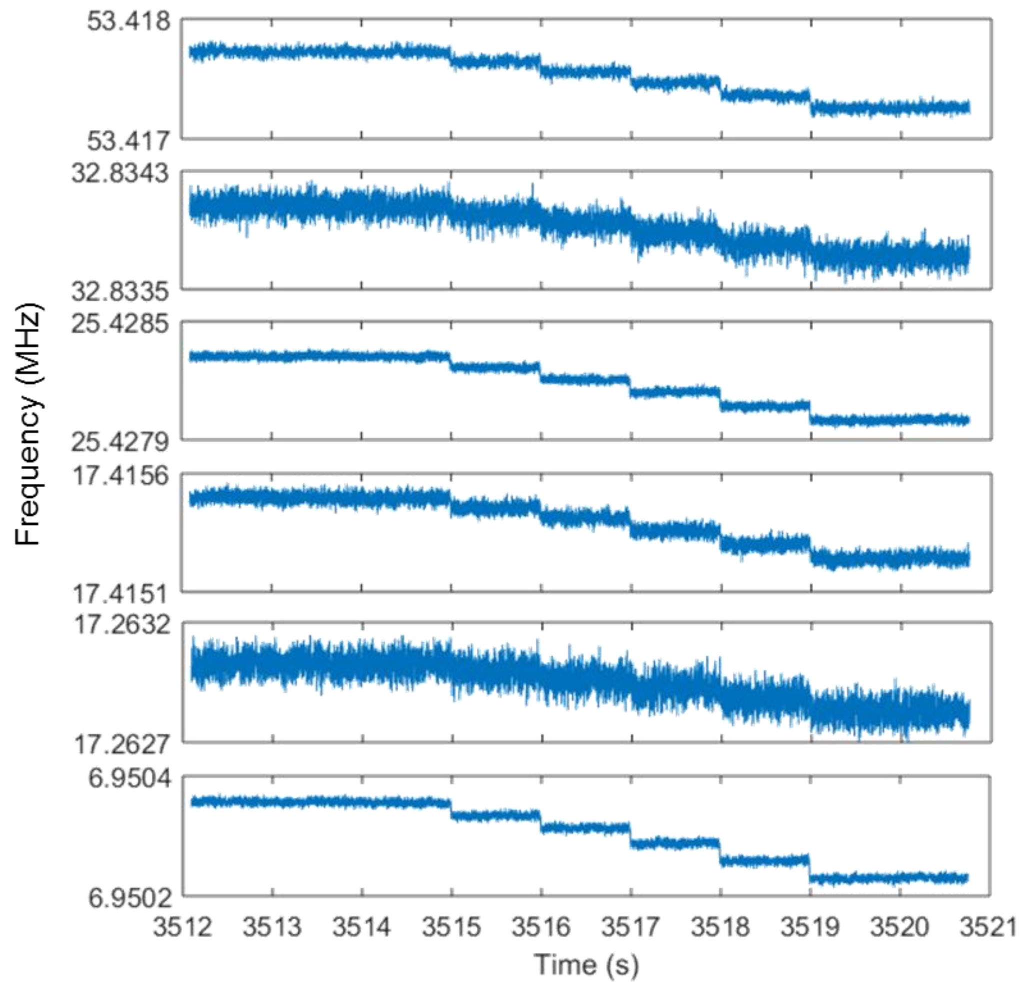

Figure 4-20 Plots of the frequency downshifts of six simultaneous modes from five deposition events of 40 nm GNP.

Starting Freq.	Event 1	Event 2	Event 3	Event 4	Event 5
$6.95\ MHz$	$20.6\ Hz$	$20.9\ Hz$	$26.2\ Hz$	$30.5\ Hz$	$30.0\ Hz$
$17.26\ MHz$	$31.0\ Hz$	$32.9\ Hz$	$44.0\ Hz$	$43.7\ Hz$	$50.4\ Hz$
$17.41\ MHz$	$38.8\ Hz$	$42.6\ Hz$	$48.8\ Hz$	$57.7\ Hz$	$60.5\ Hz$
$25.42\ MHz$	$54.5\ Hz$	$57.7\ Hz$	$65.2\ Hz$	$73.4\ Hz$	$72.5\ Hz$
$32.83\ MHz$	$57.7\ Hz$	$59.2\ Hz$	$83.8\ Hz$	$81.1\ Hz$	$71.3\ Hz$
$53.41\ MHz$	$75.0\ Hz$	$83.0\ Hz$	$92.9\ Hz$	$108.6\ Hz$	$94.6\ Hz$

Table 4-3 Summary of the frequency downshifts from the five 40 nm diameter GNP deposition events.

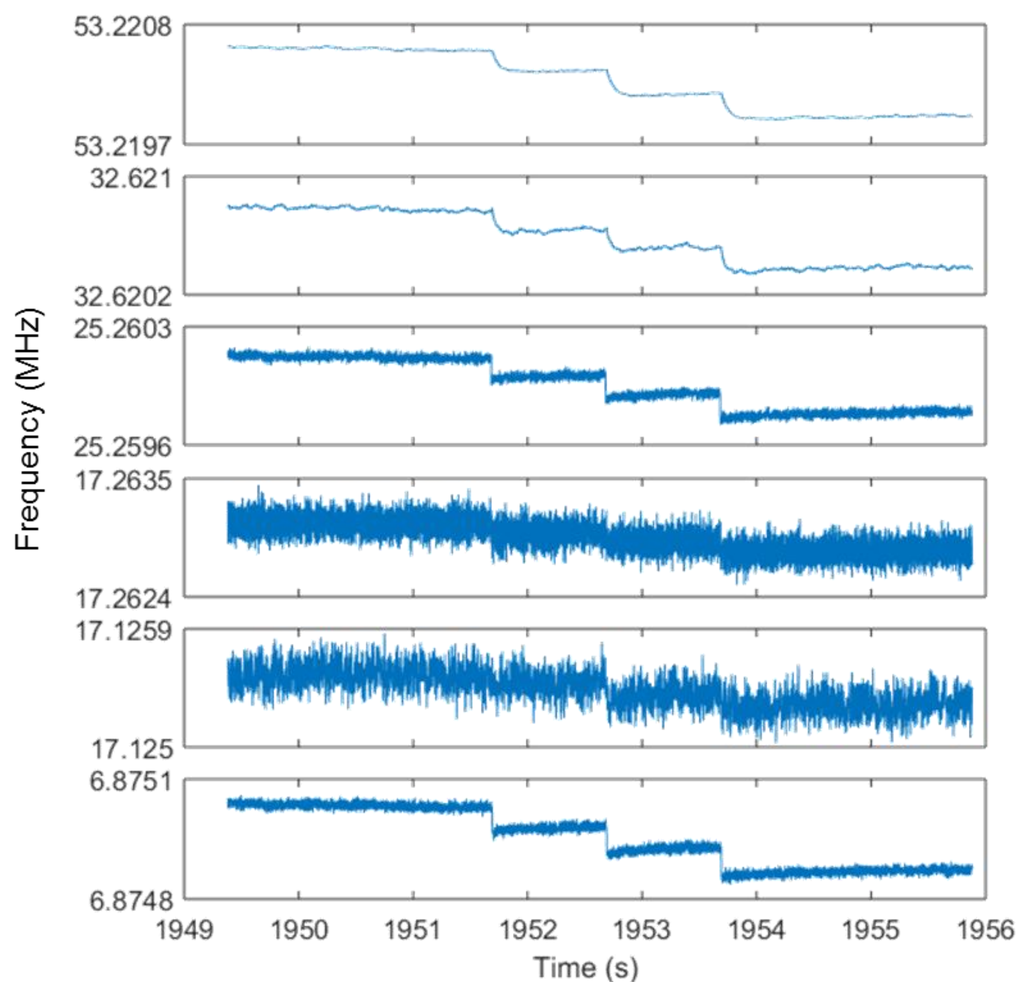

Figure 4-21 Plots of the frequency downshifts of six simultaneous modes from three deposition events of 80 nm GNP.

Starting Freq.	Event 1	Event 2	Event 3
$6.87\ MHz$	45.6 Hz	49.8 Hz	54.5 Hz
$17.12\ MHz$	65.9 Hz	142.5 Hz	102.1 Hz
$17.26\ MHz$	86.5 Hz	97.5 Hz	109.7 Hz
$25.26\ MHz$	110.8 Hz	121.2 Hz	136.2 Hz
$32.62\ MHz$	121.2 Hz	119.7 Hz	133.9 Hz
$53.22\ MHz$	145.5 Hz	165.7 Hz	167.3 Hz

Table 4-4 Summary of the frequency downshifts from the three 80 nm diameter GNP deposition events.

While there were discrete frequency downshifts in the mass loading trials, these results are not consistent with the case where one assumes that only one particle landed on the device during each event. If one assumes that, it would require the particle or $40\ nm$ or $80\ nm$ diameter to land at the same location each time on the $26\ \mu m$ by $26\ \mu m$ square plate device, which is statistically impossible. In this, as in our previous work with electrospray injection, we expect the adsorption positions of the GNPs to be stochastic and the adsorption yield per UV laser pulse to follow a Poisson distribution.

Instead, if one assumes the mass loading to be due to the desorption of a large number of very small particles from the LIAD substrate that, subsequently, deposit uniformly over the NEMS device surface, it would explain the observed frequency downshift in these experiments. In our controlled experiment, we periodically observed discrete frequency downshifts corresponding to the time that the laser pulsed. Later experiments showed the epoxy used for adhering the LIAD substrate to the glass slide may have be ablated by the laser pulse and resulted in uniform deposition of spurious materials onto the device. Analysis indicates that a uniform distribution of minute particles adsorbed to the device will appear equivalent to a single point mass located at the position corresponding to the peak of the convolution of the mode shapes employed. Next steps in this effort will insure that spurious small particle deposition after laser pulses is suppressed. This leads to the requirement that the integrated spurious adsorption across the active area of the NEMS sensor should induce a negligible frequency shift compared to that expected from the (localized)

mass of the analyte. This imposes stringent constraints; for example, assuming an effective (circular) contact area for a $40\ nm$ Au nanoparticle corresponding to a region $\sim 10\ nm$ in diameter (an area of $\sim 7.5\times\ 10^{-5}\ \mu m^2$), the ratio of contact to device areas is ~10^{-7}. Given the mass of a Au nanoparticle is $\sim 390\ MDa$ ($\sim 6.5\ \times\ 10^{-16}\ g$), uniform accumulation of spurious materials on the device surface must be suppressed below $\sim 4\ MDa$ to attain 1% error in determining analyte mass. This corresponds to only $\sim 0.4\ Da$ over the GNP contact area. Further work is required to suppress spurious adsorption to these levels in the LIAD setup.

Our analysis of the NEMS-II data elucidated another aspect of the analysis that was unanticipated. We observed that the mode shape of each of the normal modes deviates from the expected mode shape, and this can become especially pronounced for the higher modes. As discussed in Section 4.2 Operating Principal of NEMS-MS and NEMS-II, the mode shape for each normal mode is critical to the calculation in NEMS-MS and NEMS-II, especially when analyzing the higher spatial moments of the analyte mass distribution. In the case of the circular NEMS resonators it is possible to arrive at an analytic solution of the mode shape for clamped boundary conditions. For square NEMS resonators, while there is an analytic solution to the square and rectangular membrane boundary condition problem, with the bending moment of the plate included, the second order differential equation becomes a fourth order differential equation which is not possible to solve analytically. In our experiments, we typically calculated the mode shape obtained via FEM simulations, and employed the interpolated numerical results to carry out NEMS-II analysis. This

can provide erroneous results, especially for the higher moments if the actual mode shapes deviate from those obtained numerically. In the next section, we explore the experimentally obtained mode shapes of square and circular plates and compare these to what is expected ideally.

4.6 Ideal Mode Shape in 2D NEMS via Simulations and Calculations

As discussed in the previous sections, using the actual mode shapes of the normal modes is critical to analyzing data in NEMS-MS and NEMS-II. In this section, we show the mode shapes from FEM and a numerical solution to the mode shape using Raleigh-Ritz energy minimization. The FEM mode shapes presented in this section used the dimensions and material properties of those from our measurement.

Figure 4-22 and Figure 4-23 show the mode shape results from FEM. Calculations are based on a circular plate that is $4.7\ \mu m$ in diameter and $140\ nm$ thick, whereas calculations for the square plate assume $26\ \mu m$ sides and thickness similar to the circular plate. In both cases, any holes, cuts, etc. induced by the fabrication process were included to ensure correspondence with the measured system.

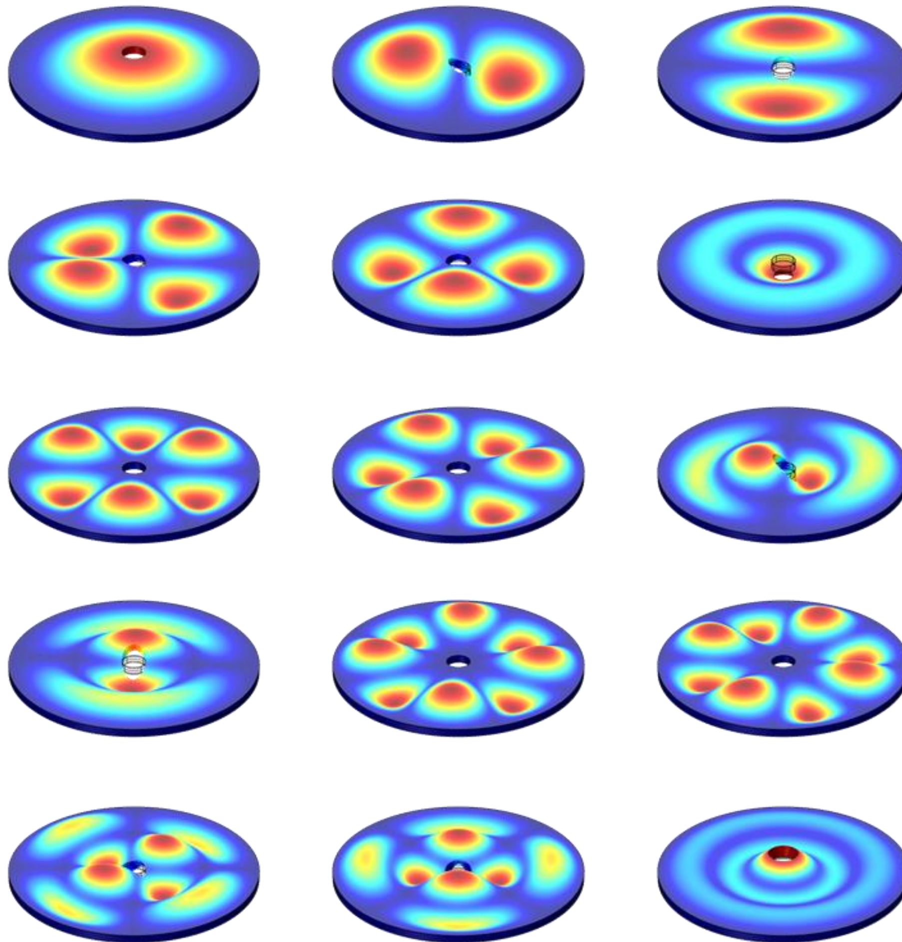

Figure 4-22 Mode shapes for a circular plate from FEM. A diameter of 4.7 μm and a thickness of 140 nm were used for the simulation.

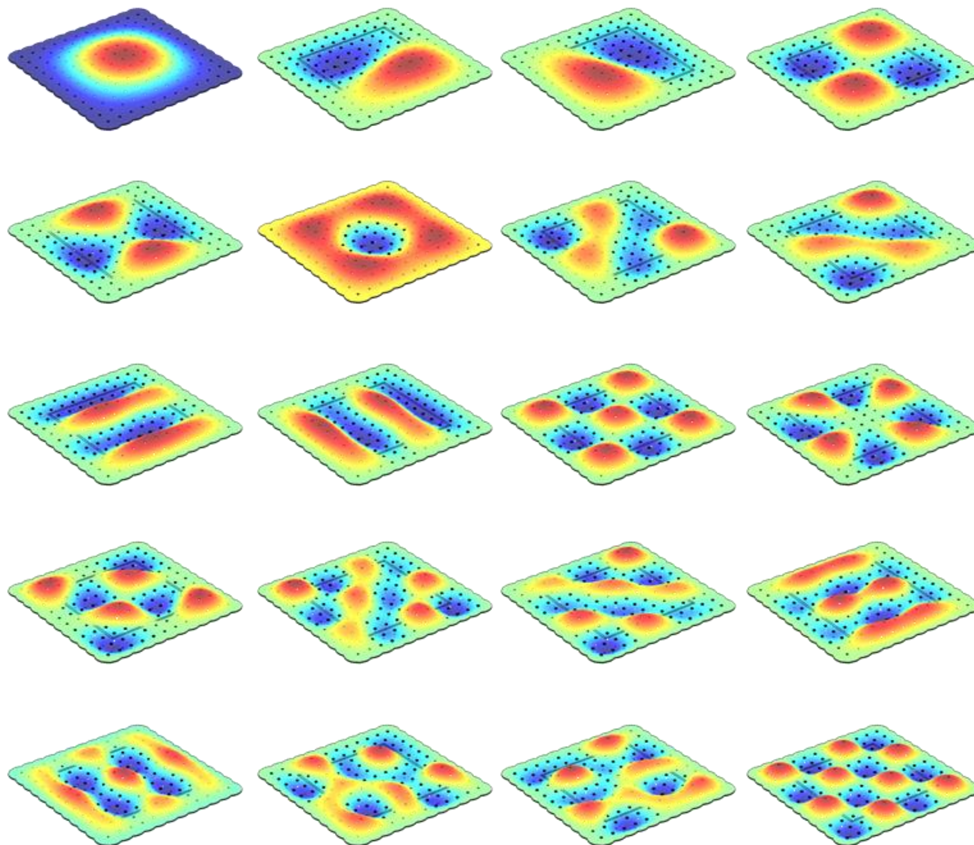

Figure 4-23 Mode shapes for a circular plate from FEM. Sides of $26\ \mu m$ long and a thickness of $140\ nm$ were used.

In the calculations for NEMS-MS and NEMS-II, the mode shape must be converted into a numerical form. While it was possible to import the mode shape generated from FEM and to interpolate, the results we obtained were sometimes far from ideal, especially when the second or higher derivatives were needed as for the case of NEMS-II. We found that it is much preferable to have an analytic solution of the mode shape. In the case of the circular plate, by solving the equation of motion

with clamped boundary conditions, the mode shapes for the first three modes are given by:

$$\Phi_{01} \propto \left(J_0(k_{01}r) + \mu_{01}I_0(k_{01}r)\right), \quad \text{Eq. 4-15}$$

$$\Phi_{11} \propto \left(J_1(k_{11}r) + \mu_{11}I_1(k_{11}r)\right)\sin(\theta), \quad \text{Eq. 4-16}$$

$$\Phi_{11} \propto \left(J_1(k_{11}r) + \mu_{11}I_1(k_{11}r)\right)\cos(\theta), \quad \text{Eq. 4-17}$$

where J_n is the Bessel function of the first kind, I_n is the modified Bessel function of the first kind, k_{nm} are the solutions to the boundary value problem with clamped edges, and μ_{nm} are the ratios between the two Bessel functions to satisfy the remaining boundary conditions [27].

In the case of the square plate, analytic solutions to the boundary value problem are not possible. There are, however, analytic solutions for a square membrane without a bending moment. In the case where the plate is thin, the solutions for the square plate and those of the square membrane are extremely similar. We used the set of square membrane mode shapes as a set of basis to approximate the square plate mode shapes. We approximated the solution using Raleigh-Ritz energy minimization method, which assumed the general mode shape to be a linear combination of the square membrane mode shapes and solved for the coefficients in the linear combination to minimize the resonant frequency [28].

4.7 Measured Mode Shape

In the previous section, we discussed several methods for arriving at a numerical expression for the mode shapes: via interpolation of FEM results, by solving the boundary value problem, and by approximating the solution using Raleigh-Ritz variation. In our experiment, in order to compare the accuracy of each of the above methods, we measured the mode shapes experimentally using the optical setup depicted in Figure 3-11. It was during this experimental verification process that we first discovered the degree to which measured mode shapes can deviate from the ideal mode shapes. For the remainder of this chapter, we will elucidate the observed deviation of these mode shapes from ideality, and describe our experiments to isolate the cause of these deviations. We first discuss careful measurements of mode shapes.

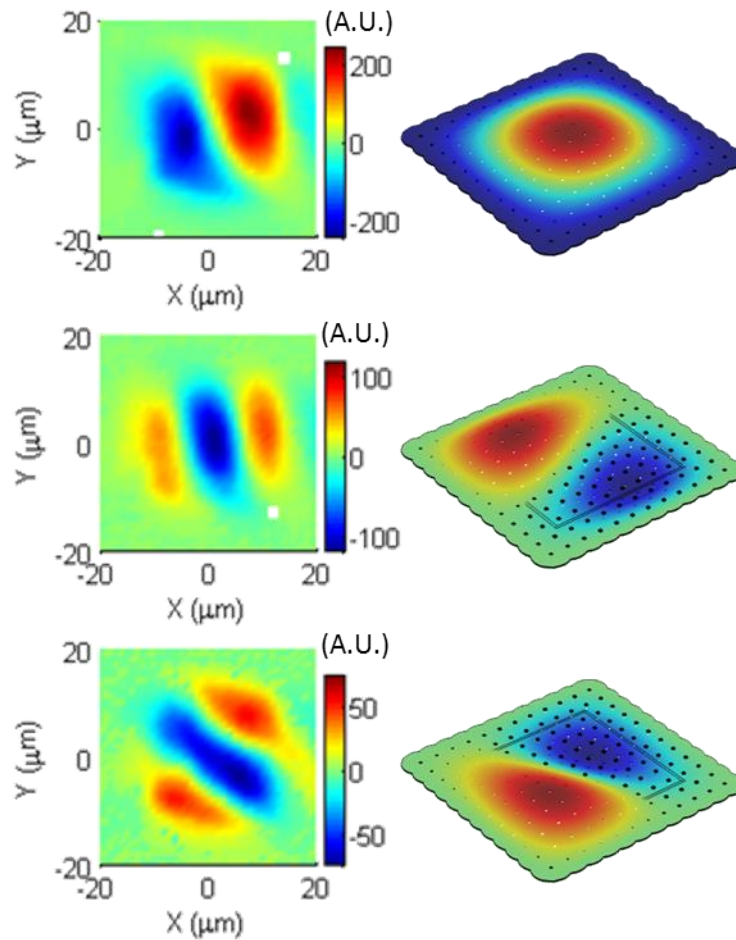

Figure 4-24 Comparison of the lowest three measured (left column) and simulated (right column) mode shapes for a square plate resonator clamped at its edges. (top) Mode corresponding to the lowest frequency measured or simulated fundamental mode. (middle and bottom) Degenerate modes corresponding to the next modes measured and simulated.

In Figure 4-24 we present a comparison of the first two simulated and measured mode shapes. For the simulation results, the second mode corresponds to out-of-plane antiphase motion occurring simultaneously between the two halves of the plate. Note that the lowest measured mode shape resembles the second mode

shape obtained from the simulations. Careful analysis of our experimental results seem to indicate that the lowest measured mode is actually the fundamental mode. Evidence for this is as follows: Multiple square plate devices were actuated with piezoelectric actuation as well as piezoshaker actuation; yet no lower-lying modes were observed experimentally. If the lowest mode observed experimentally was indeed the second mode, another near-degenerate resonance peak would be expected; this was not observed. By contrast, the second set of measured modes does exhibit such degeneracies. Further, the spacing of the measured resonant frequencies for the first thirteen modes all match expectations from simulations within 0.5% of the ideal resonant frequency spacing, as shown in Figure 4-25. Finally, we have carefully verified that the spatial variation in the lowest measured mode is not caused by the intrinsic nonlinearity in optical interferometry. (This intrinsic nonlinearity arises because between adjacent constructive interference maxima, the interferometer's signal intensity response is sinusoidal.) Accessing the regime of nonlinear response would require the device motional amplitudes to be comparable to the wavelength of the detection laser. This is not the case in our experiments; we verified that the induced response is linear with the actuation drive Figure 4-26. This evidence leads us to believe that the lowest measured resonance is actually the fundamental mode.

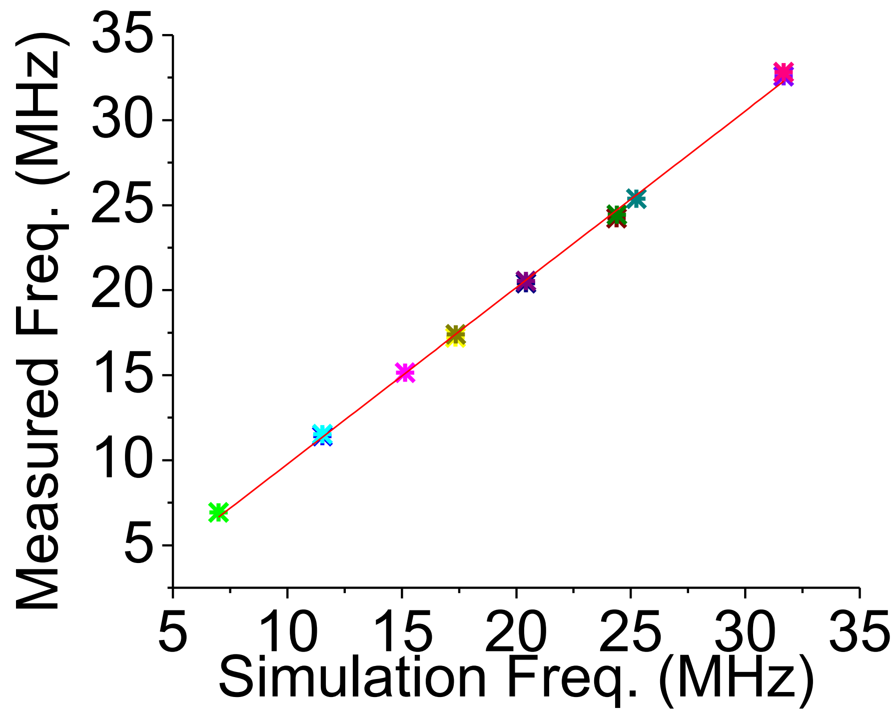

Figure 4-25 Comparison of the ideal and measured normal mode frequencies for the first thirteen modes of a square plate with sides of 26 μm long. For each data point in this plot, the x-coordinate is the frequency from FEM while the y-coordinate is the frequency measured. No modes were omitted in order to match frequencies from FEM.

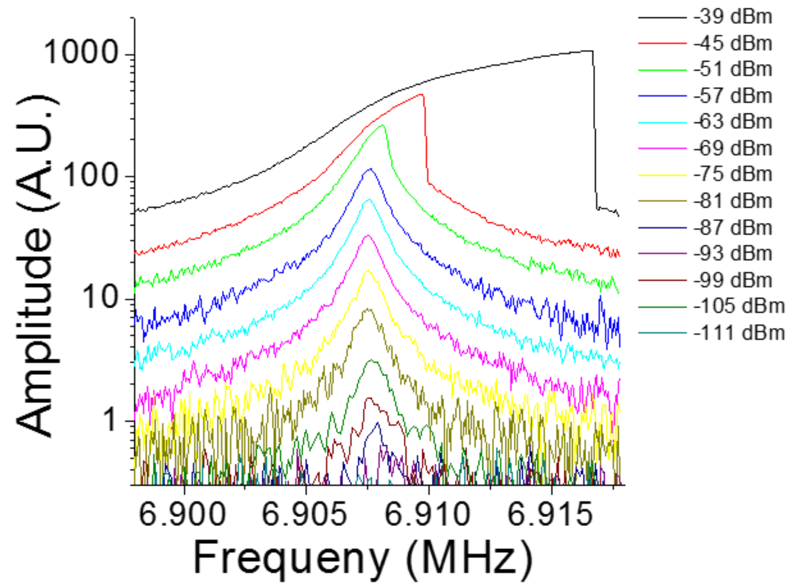

Figure 4-26 Frequency sweep of the device driven from the linear response regime to the nonlinear response regime. This was performed using piezoelectric actuation and the actuation power was doubled each time. The displacement doubled with the doubling of the actuation power with no signs of compression; this provides evidence the regime of optical nonlinearity for the interferometry system is not accessed.

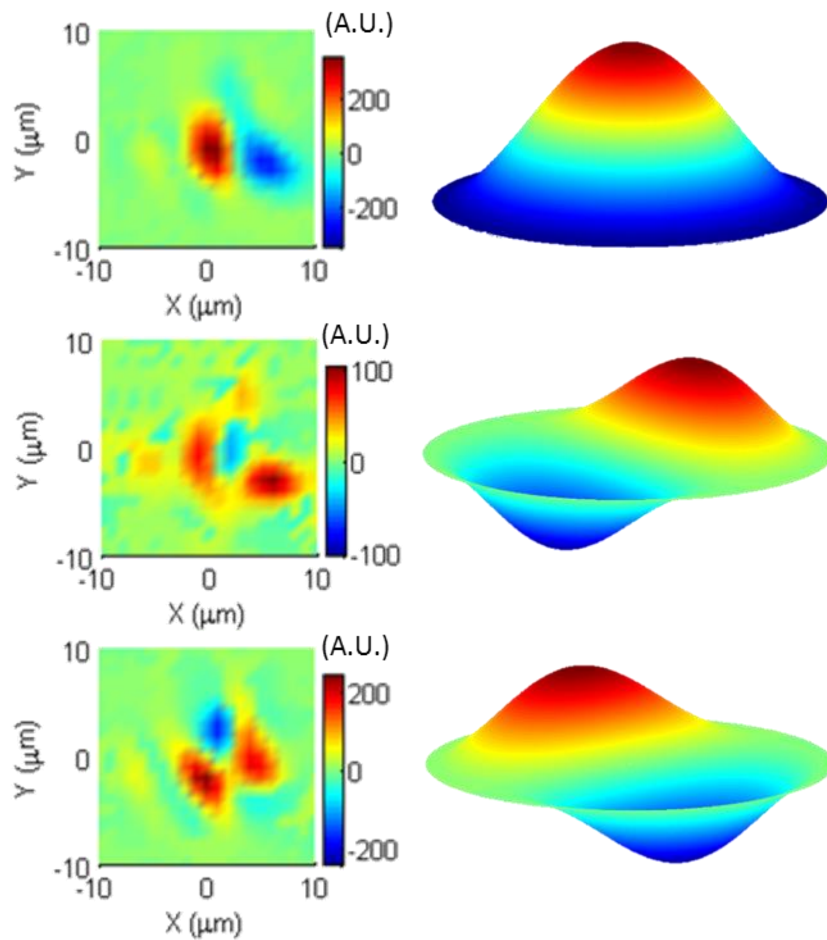

Figure 4-27 Comparison of three lowest mode shapes obtained from measurements (left column) and simulations for ideal (right column) circular plates.

Upon careful examination, we observed that while circular plates did not have obvious deviations from the ideal mode shape such as those seen in the square plates, there are still deviations as seen in Figure 4-27. While not explicitly discussed in a recent publication [29], such deviations have been observed in the measured mode shapes of microscale circular plate resonators (in this case patterned from graphene). As shown in Figure 4-27, this is especially evident for the higher modes.

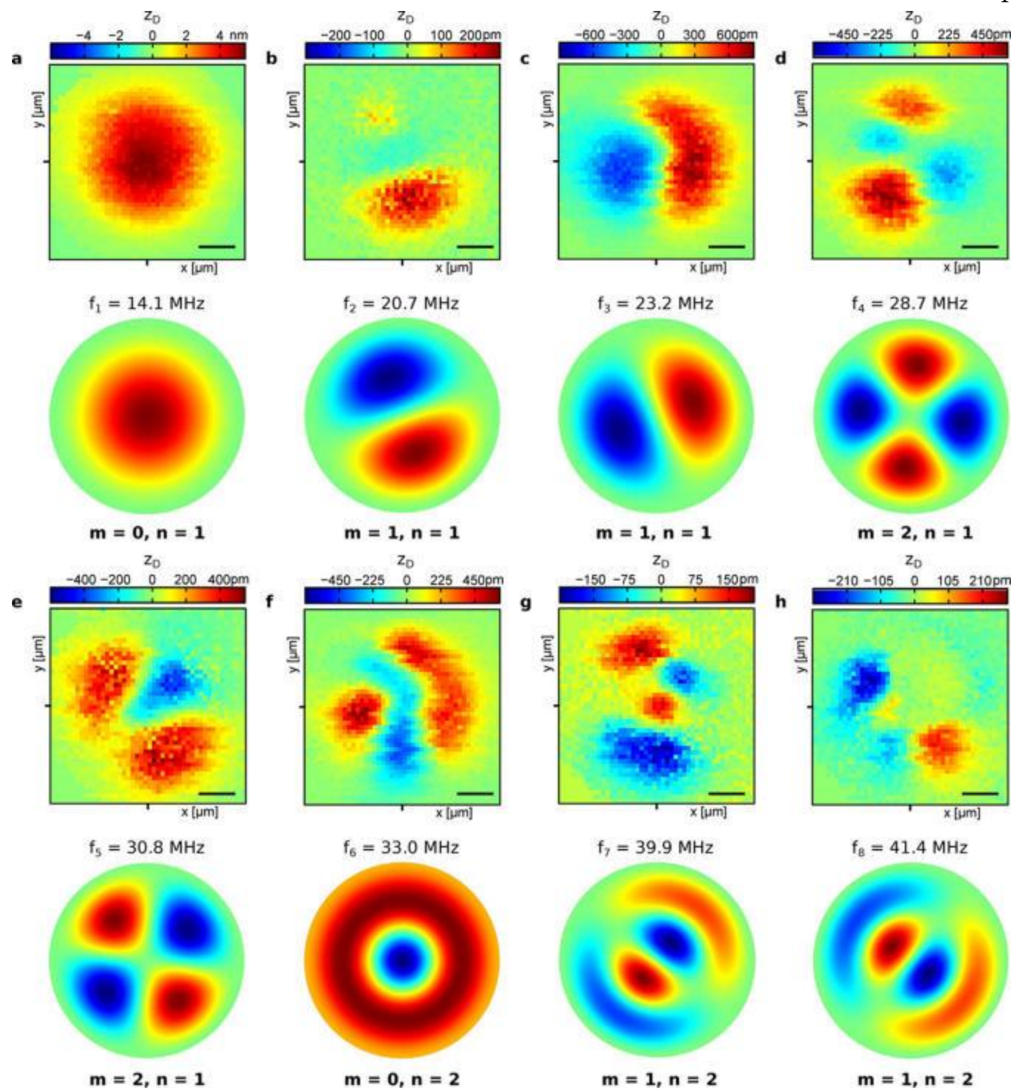

Figure 4-28 Comparison of the lowest eight measured and ideal circular membrane mode shapes using a graphene device. Image is reproduced from Davidovikj, D., *et al.* [29].

Because the exact mode shapes are critical in NEMS-MS and NEMS-II, in the next section, we test various non-ideal conditions to explain the non-matching mode shapes.

4.8 Effect of Non-idealities on Mode Shape

It is critical to employ accurate experimental mode shapes in NEMS-MS, and particularly, higher moment NEMS-II analysis. Accordingly, in this section we explore potential sources for the mode shape non-idealities we have observed. For most of these explorations, we base our measurements and calculations on square plate resonators with $26\ \mu m$ sides. Multiple square plates from different fabrication batches were tested to ensure that the observed deviations from ideality were not due to specific defects in individual devices. We tested for mode shape dependence upon different actuation methods, on actuation power, on detection laser power, on the presence of static anisotropic stress in the membranes, and on methods for stress reduction.

We first explore the dependence of mode shape on different actuation methods and actuation amplitude. Since the square plates were typically driven using piezoelectric actuation, we first explored whether nonuniformity in the plate and actuation electrode geometries could be inducing the observed mode shape deviations. To pursue this question, we actuated devices using a piezoshaker mounted to the back of the device. This served to induce uniform A.C. acceleration across the device at the resonance frequency. Figure 4-29 compares results from piezoshaker-induced inertial actuation against those obtained with piezoelectric actuation of the AlN membrane. For both actuation methods, the device was driven within the linear regime, to the onset of nonlinearity, and beyond – *i.e.* in the regime of nonlinear

mechanical response. For a well-controlled comparison, the actuation forces applied were matched for these two methods, so that the induced device response amplitudes were identical. The results show that the lower the actuation power, the weaker the response. However, regardless of the driving power or the actuation methods, the mode shape of the lowest mode remains unchanged, with two opposing lobes, resembling what is expected from the second mode of an ideal square plate.

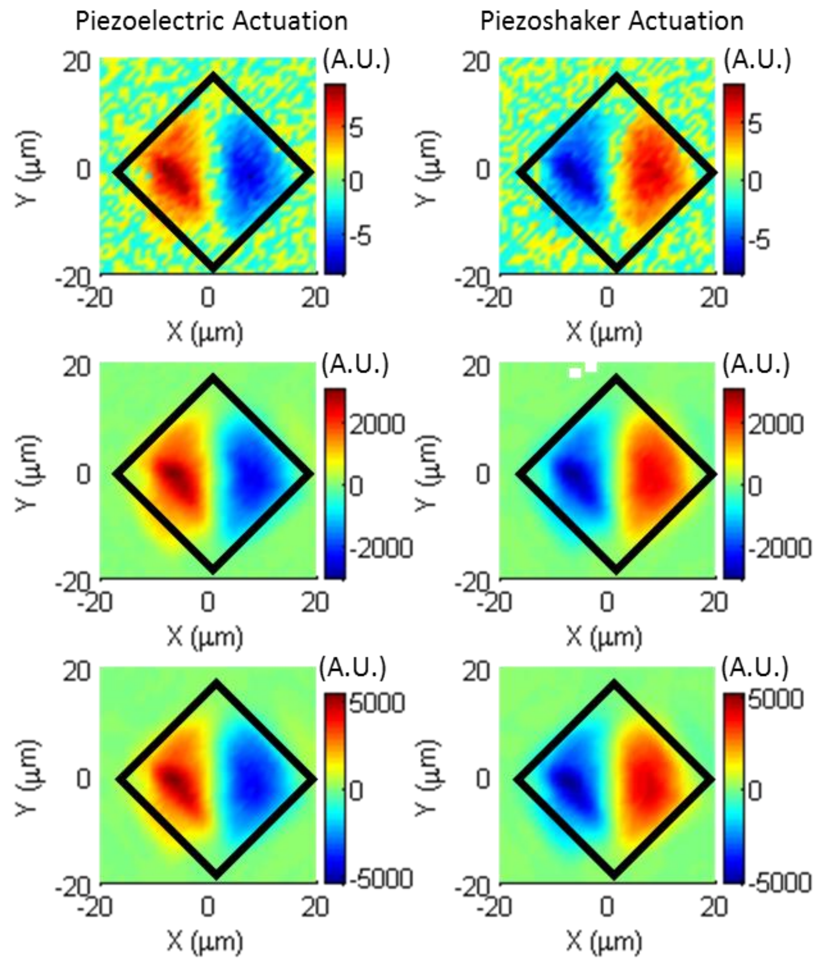

Figure 4-29 Effect of actuation method and actuation power on the putative fundamental mode shape. The black square denotes the approximate boundary of the square plate. The left column was driven using piezoelectric actuation of the AlN material. The right column was driven using a piezoshaker mounted on the chip. The top row was driven to the linear response regime of the device. The middle row was driven to the onset of nonlinearity of the device. The bottom row was driven to the nonlinear regime of the device. In all cases, the mode shape resulted in two lobes with opposite motions.

Since the actuation power did not appear to affect the response, we explored the effect of detection laser power, used for optical interferometry in displacement transduction, on the mode shape. The detection laser for all of the experiments in this thesis has a maximum of $2.5\ mW$ power. We attenuated the laser power from full power (100%) to 0.1% of the laser power. As the laser power decreased, the signal decreased as well, but the deviation from the expected mode shape remained constant.

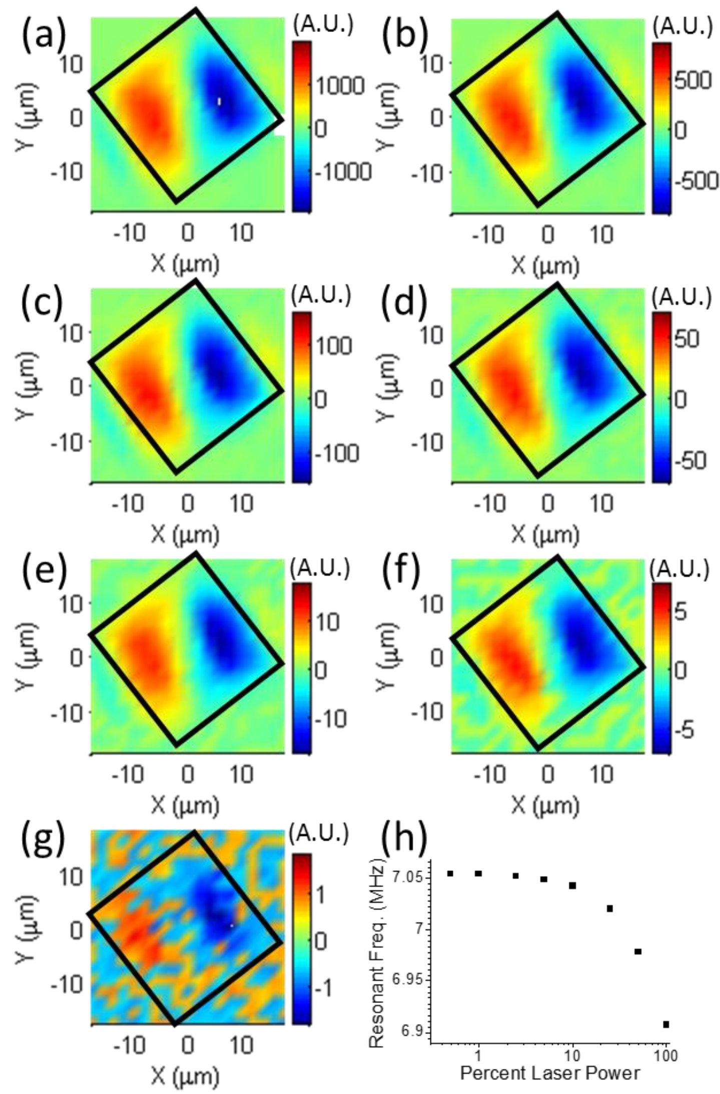

Figure 4-30 Effect of detection laser power on the mode shape of the lowest measured square plate mode. (a-g) Mode shape displacement as a function of laser power. The laser powers were (a) 100% (b) 50% (c) 10% (d) 5% (e) 1% (f) 0.5% and (g) 0.1% of $\sim 1.25\ mW$. As the laser power is attenuated, the signal is weaker, but the deviation from the expected mode shape is still the same. (h) Resonant frequency as a function of percent laser power. By $\sim 0.5\%$ of the laser power, the effect of laser power on resonant frequency is negligible.

Since it appears that the actuation method, actuation power, and laser detection power do not induce the observed deviations from ideal mode shape, we explored the effect of stress on the mode shape. In Chapter 3, we demonstrated that the stress can indeed change the mode shape. Specifically, we hypothesized that anisotropic stress could qualitatively alter mode shapes.

Through FEM, the square plate with anisotropic stress was simulated. For this simulation, a stress of $300\ MPa$ was applied in the x direction while the stress in the y direction was varied: $300\ MPa$, $30\ MPa$, $3\ MPa$, $0\ MPa$, $-3\ MPa$, and $-30\ MPa$. Figure 4-31 shows the result from the simulation; it is evident that no noticeable difference emerges from anisotropic stress. The only effect that emerges is the breaking of the x-y symmetry for the degenerate modes. This is, of course, to be expected when stress in the x and y directions are not the same. However, regardless of magnitude of the imposed stress anisotropy, the measured fundamental mode shapes – one displaying two opposite lobes – were not recovered from these simulations.

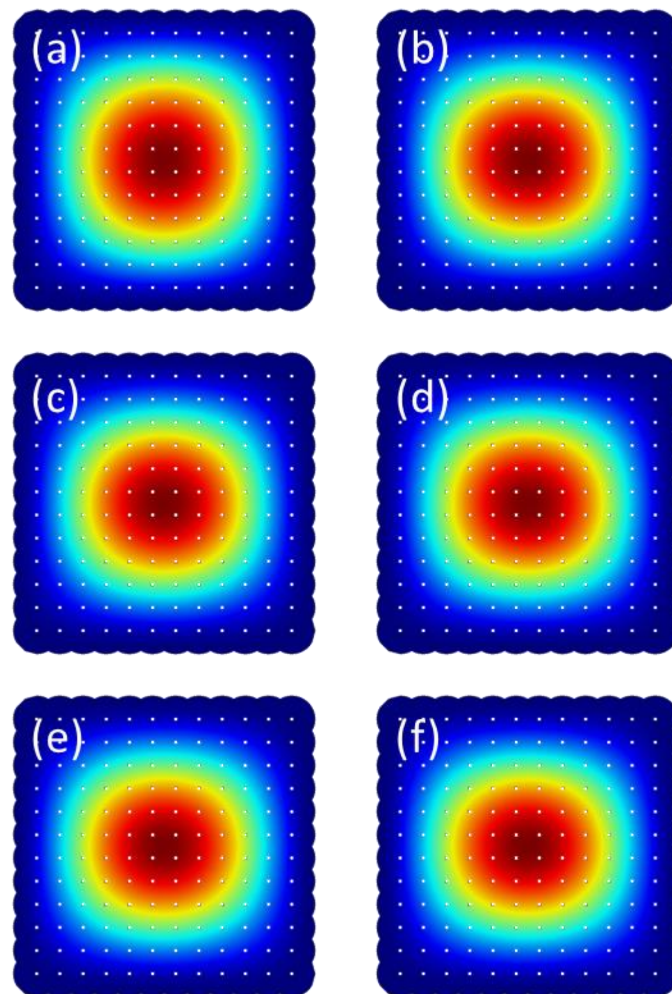

Figure 4-31 FEM on the effect of anisotropic stress on mode shape. All six simulations have $300\ MPa$ of stress in the x direction. The stress in the y direction varies as follows: (a) $300\ MPa$, (b) $30\ MPa$, (c) $3\ MPa$, (d) $0\ MPa$, (e) $-3\ MPa$, (f) $-30\ MPa$.

We tested the effect of stress reduction on the mode shape. When we compare the frequencies obtained from our FEM simulations with the experimentally measured modal frequencies, we are able to obtain a match if we assume the membranes are under an isotropic stress with $300\ MPa$ tensile stress. Square plate

devices similar to those measured previously were fabricated. The difference in these devices is that material from part of the device was removed to help reduce the stress within the device. Symmetry was preserved in the removal of the material. Compared to our FEM simulations with the experimentally measured modal frequencies for these devices, we are able to obtain match by assuming the membranes are under an isotropic stress with 1 MPa tensile stress, 2.5 orders of magnitude lower than the previously measured devices. Figure 4-32 shows that the mode shape for such a device still exhibits two halves moving in opposite directions, which appears to indicate that stress reduction does not suppress the deviation from the ideal mode shapes.

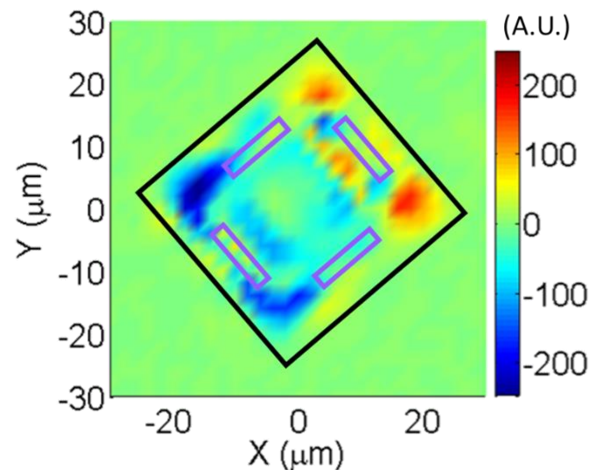

Figure 4-32 Effect of reduction of stress on mode shape. A square plate similar to those measured before but with material within the purple rectangles removed is driven. The response is the lowest resonant mode shape, which still exhibits two lobes moving in opposite directions.

Finally, we tested the effect of uncontrolled spatial variations in the optical interferometer. To achieve displacement detection for a mechanical resonator, it is sufficient to measure at one locale of a spatially extended device. Here, however, we are interested in measuring the spatial mode shapes for the devices. Since we are using an optical interferometry detection scheme, non-parallel reflection surfaces in the interference cavity would result in a background phase difference that is static, spatially dependent, and independent of the actual mode shape being measured. To explore whether this explains the anomalous mode shape data, we assume this mechanism alters our data and determine the phase correction by calculating the phase difference between the first measured mechanical mode (Figure 4-33a) and the first calculated mode (Figure 4-33b). If this explains the anomalies present, we should be able to apply this phase correction to the higher modes and recover the true (calculated) mode shape. To deduce the phase correction, $\theta(x, y)$, we created a spatial map, $\cos[\theta(x, y)]$, relating the first measured and calculated mode (Figure 4-33c):

$$\varphi_n'(x, y) = \varphi(x, y)\cos[\theta(x, y)]. \qquad \text{Eq. 4-18}$$

Here, $\varphi(x, y)$ is the calculated (normalized) mode shape for mode *n*. $\varphi_n'(x, y)$ is the measured (normalized) mode shape for mode n, assuming it is altered by a static, position-dependent phase shift due to a non-ideal interferometer. The deduced position-dependent phase shift arising from non-ideal cavity (in radians) is

$$\theta(x, y) = \cos^{-1}\left[\frac{\varphi_n'(x, y)}{\varphi_n(x, y)}\right]. \qquad \text{Eq. 4-19}$$

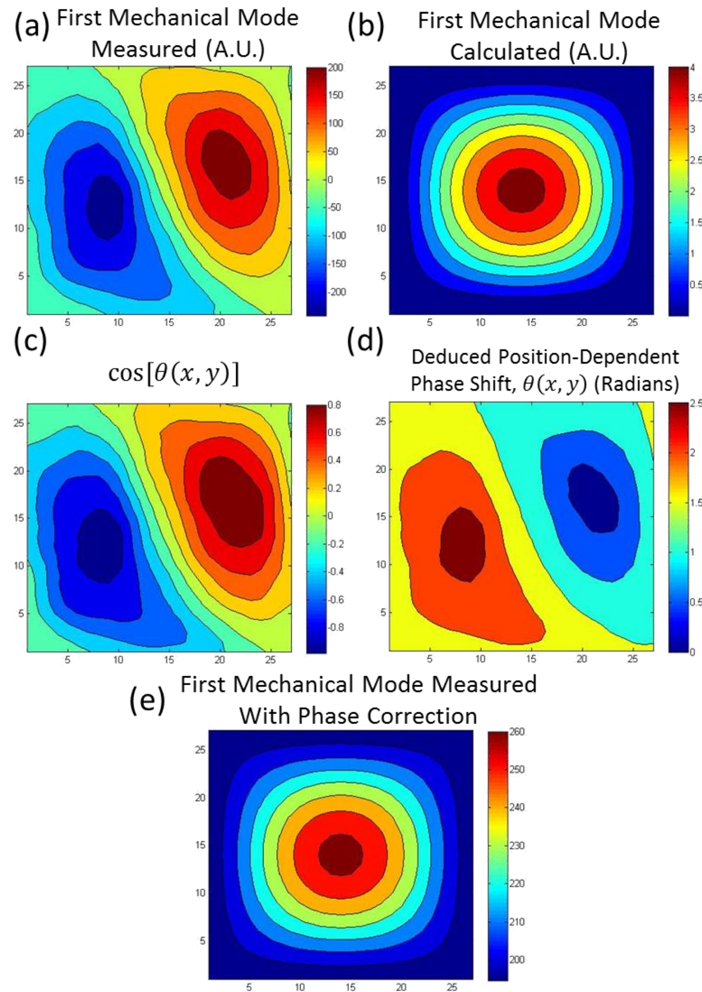

Figure 4-33 Effect of variation in optical cavity in the first mechanical mode. (a) First measured mechanical mode. (b) First calculated mechanical mode. (c) Quotient of the first measured mode to first calculated mode. (d) Phase difference between measured and calculated mode. (e) Result of applying the phase correction to the first measured mode to recover the first calculated mode.

We verify the phase correction g by applying it back to the first mechanical mode measured and recovering the calculated first mechanical mode shape.

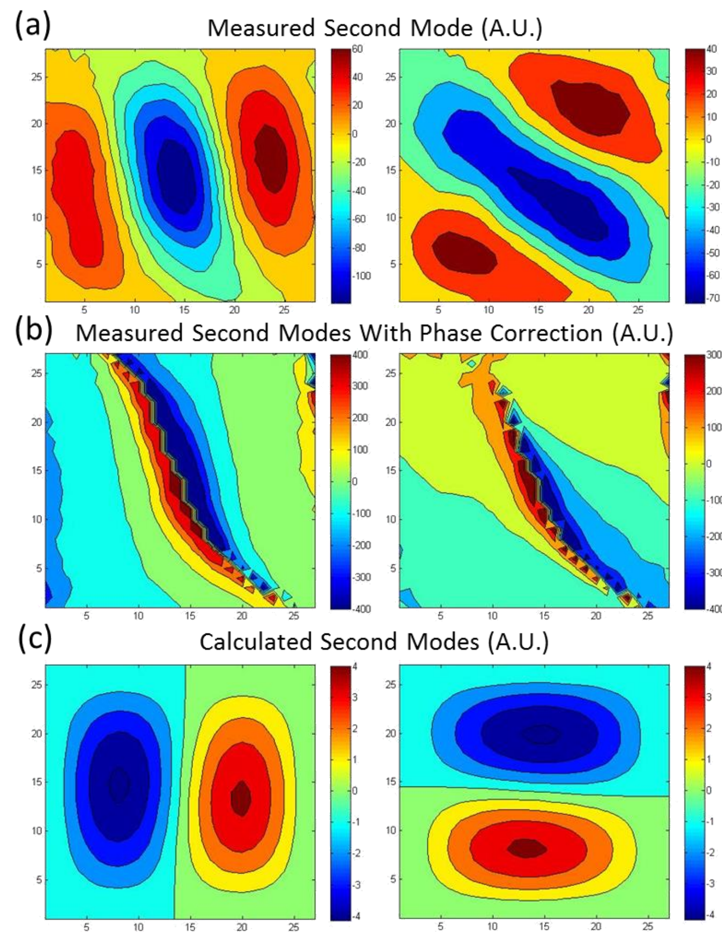

Figure 4-34 Phase correction applied to two degenerate second mechanical mode. (a) Measured degenerate second modes. (b) Phase corrected degenerate second mode. (c) Calculated degenerated second modes.

We apply the phase correction obtained above to the measured second mechanical mode (Figure 4-34a). However, the phase corrected second modes (Figure 4-34b) do not resemble the calculated second modes (Figure 4-34c). Thus, it does not seem that the phase correction is sufficient to correct for the anomalous mode shape data.

While the various tests did not find the cause for the deviation of the mode shape, we showed that the deviation was not caused by actuation method, actuation power, laser interrogation power, anisotropic stress, the amount of stress, or the variation in the optical cavity. It is possible that thickness variations in the device, due to unknown and potentially uncontrolled etching processes, could induce the observed nonidealities. Further tests are in progress to establish the mechanisms underlying these mode shape deviations. We are also beginning to explore other membrane geometries that may be less susceptible to these effects.

4.9 Summary

In this chapter, we have discussed well-established methods of mass spectrometry and describe how NEMS can overcome their intrinsic limitations. We have described the operating principles of NEMS mass spectrometry (NEMS-MS) and NEMS inertial imaging (NEMS-II), and report our experiments to measure gold nanoparticles with these new methods. While our preliminary data is promising, we discussed reasons why we believe the data may not be representative of gold nanoparticle inertial imaging. We also showed that the data could be consistent with deposition of spurious fine particles desorbed by laser-induced acoustic desorption (LIAD) pulses. We have also carried out a detailed investigation of the mode shapes of NEMS plates. Knowledge of the precise experimental mode shapes for the NEMS sensors employed is crucial in performing NEMS-MS and NEMS-II. We have demonstrated that the experimentally-measured mode shapes of both square and

circular plates can significantly deviate from idealized mode shapes obtained from simulations and calculations. We tested various potential reasons for the deviations, including actuation methods, actuation power, laser detection power, anisotropic stress, and the reduction of stress, and have shown that these do not appear to explain the mode shape deviations we have observed. While we have made much progress toward pulsatory (MALDI and LIAD-based) NEMS-MS and NEMS-II, additional effort is still required to obtain careful analyte deposition in this case. (It is noteworthy that, since electrospray ionization is a continuous and non-pulsatory method, such background effects can clearly be separated from the sudden shifts arising from discrete analyte absorption events.)

4.10 Bibliography

1. Potts, P.J., et al., *Microanalytical Methods in Mineralogy and GeochemistryInductively coupled plasma-mass spectrometric analysis of geological samples: A critical evaluation based on case studies.* Chemical Geology, 1990. **83**(1): p. 105-118.
2. Cohen, A.S. and F.G. Waters, *Separation of osmium from geological materials by solvent extraction for analysis by thermal ionisation mass spectrometry.* Analytica Chimica Acta, 1996. **332**(2–3): p. 269-275.
3. Eggins, S.M., et al., *A simple method for the precise determination of ≥ 40 trace elements in geological samples by ICPMS using enriched isotope internal standardisation.* Chemical Geology, 1997. **134**(4): p. 311-326.
4. Longbottom, J.E., et al., *Determination of Trace-Elements in Water by Inductively-Coupled Plasma-Mass Spectrometry - Collaborative Study.* Journal of Aoac International, 1994. **77**(4): p. 1004-1023.
5. Garbarino, J.R., *Methods of analysis by the U.S. Geological Survey National Water Quality Laboratory; determination of dissolved arsenic, boron, lithium, selenium, strontium, thallium, and vanadium using inductively coupled plasma-mass spectrometry*, in *Open-File Report*. 1999.
6. Hirsch, R., et al., *Determination of antibiotics in different water compartments via liquid chromatography–electrospray tandem mass spectrometry.* Journal of Chromatography A, 1998. **815**(2): p. 213-223.

7. Nakahara, Y., et al., *Hair Analysis for Drug Abuse: I. Determination of Methamphetamine and Amphetamine in Hair by Stable Isotope Dilution Gas Chromatography/Mass Spectrometry Method.*

8. Dams, R., et al., *Urine drug testing for opioids, cocaine, and metabolites by direct injection liquid chromatography/tandem mass spectrometry.* Rapid Communications in Mass Spectrometry, 2003. **17**(14): p. 1665-1670.

9. Øiestad, E.L., U. Johansen, and A.S. Christophersen, *Drug Screening of Preserved Oral Fluid by Liquid Chromatography–Tandem Mass Spectrometry.* Clinical Chemistry, 2007. **53**(2): p. 300-309.

10. Aebersold, R. and M. Mann, *Mass spectrometry-based proteomics.* Nature, 2003. **422**(6928): p. 198-207.

11. Ong, S.-E. and M. Mann, *Mass spectrometry-based proteomics turns quantitative.* Nat Chem Biol, 2005. **1**(5): p. 252-262.

12. Bantscheff, M., et al., *Quantitative mass spectrometry in proteomics: a critical review.* Analytical and Bioanalytical Chemistry, 2007. **389**(4): p. 1017-1031.

13. Sage, E., et al., *Neutral particle mass spectrometry with nanomechanical systems.* Nat Commun, 2015. **6**.

14. Hanay, M.S., et al., *Single-protein nanomechanical mass spectrometry in real time.* Nat Nano, 2012. **7**(9): p. 602-608.

15. Glish, G.L. and R.W. Vachet, *The basics of mass spectrometry in the twenty-first century.* Nat Rev Drug Discov, 2003. **2**(2): p. 140-150.

16. Loo, J.A., *Studying noncovalent protein complexes by electrospray ionization mass spectrometry.* Mass Spectrom Rev, 1997. **16**(1): p. 1-23.

17. Fenn, J., et al., *Electrospray ionization for mass spectrometry of large biomolecules.* Science, 1989. **246**(4926): p. 64-71.

18. Cameron, A.E. and D.F. Eggers, *An Ion "Velocitron".* Review of Scientific Instruments, 1948. **19**(9): p. 605-607.

19. Cotter, R.J., *Time-of-Flight Mass Spectrometry*, in *Time-of-Flight Mass Spectrometry*. 1993, American Chemical Society. p. 16-48.

20. Lifshitz, R. and M.C. Cross, *Nonlinear Dynamics of Nanomechanical and Micromechanical Resonators*, in *Reviews of Nonlinear Dynamics and Complexity*. 2009, Wiley-VCH Verlag GmbH & Co. KGaA. p. 1-52.

21. Naik, A.K., et al., *Towards single-molecule nanomechanical mass spectrometry.* Nat Nano, 2009. **4**(7): p. 445-450.

22. Hanay, M.S., *Towards Single-Molecule Nanomechanical Mass Spectrometry*. 2011, California Institute of Technology.

23. Matheny, M.H., et al., *Phase Synchronization of Two Anharmonic Nanomechanical Oscillators.* Physical Review Letters, 2014. **112**(1): p. 014101.

24. Deegan, R.D., et al., *Capillary flow as the cause of ring stains from dried liquid drops.* Nature, 1997. **389**(6653): p. 827-829.

25. Tanaka, K., et al., *Protein and polymer analyses up to m/z 100 000 by laser ionization time-of-flight mass spectrometry.* Rapid Communications in Mass Spectrometry, 1988. **2**(8): p. 151-153.

26. McLean, J.A., K.A. Stumpo, and D.H. Russell, *Size-Selected (2−10 nm) Gold Nanoparticles for Matrix Assisted Laser Desorption Ionization of Peptides.* Journal of the American Chemical Society, 2005. **127**(15): p. 5304-5305.

27. Kerschen, G., *Modal Analysis of Nonlinear Mechanical Systems*. 2014: Springer Vienna.

28. Holzweissig, F., *A. W. Leissa, Vibration of Plates. (Nasa Sp-160). VII + 353 S. m. Fig. Washington 1969. Office of Technology Utilization National Aeronautics and Space Administration. Preis brosch. $ 3.50.* ZAMM - Journal of Applied Mathematics and Mechanics / Zeitschrift für Angewandte Mathematik und Mechanik, 1971. **51**(3): p. 243-243.

29. Davidovikj, D., et al., *Visualizing the Motion of Graphene Nanodrums.* Nano Letters, 2016. **16**(4): p. 2768-2773.

Chapter 5

CONCLUSIONS AND PERSPECTIVES

This chapter concludes the thesis by summarizing the findings from each of the three applications of nanoelectromechanical systems (NEMS): NEMS switches, *in-situ* measurement of material properties in a nano-device, and NEMS mass spectrometry (NEMS-MS) and NEMS inertial imaging (NEMS-II). A futuristic outlook of these technologies developed is described.

5.1 Summary

In this thesis, we discussed three novel applications of NEMS. We started with a discussion of what NEMS and MEMS are and many applications emerging with relevance to our everyday lives. We also described the history and challenges in miniaturizing transistors and introduced mass spectrometry and its applications to various fields of science and engineering.

For our first application of NEMS, we discussed NEMS switches and their advantages. We described two different geometries – doubly-clamped beams and cantilevers – for NEMS switches as well as different performance metrics for an ideal switch. We discussed various common materials used for NEMS switches and showed that graphene is an interesting material for this application. We described fabrication processes for our graphene NEMS switches and demonstrated unprecedented switching results. We continued

with the optimization of the transfer of chemical vapor deposition (CVD) graphene, which allows for their large-scale production, and showed the improvement to the device from the optimizing. Lastly we discussed using aluminum nitride (AlN) as another material for NEMS switches because of its unique ability for piezoelectric actuation.

In our second application, we described a new method of using the anharmonic nonlinearity of NEMS resonators to determine *in-situ* the stress and speed of sound in a material. Compared to previous methods, this new method considers the effects of stress on the mode shape, which affects the measured speed of sound and stress. It also allows for an accurate measurement to be performed even if the device is not in the tension-dominating regime or unstressed regime. We tested the method by fabricating silicon doubly-clamped beams along different crystallographic orientations, which resulted in different speeds of sound for the family of devices. We verified this method by experimentally measuring the speeds of sound of the various silicon beams.

In our third application of NEMS, we discussed the use of NEMS for 2D mass spectrometry and inertial imaging, which permits determination of higher mass moments such as variance and skewness in the spatial mass distribution. We used AlN circular and square plate resonators and deposited gold nanoparticles (GNP) using two different deposition techniques, matrix-assisted laser desorption/ionization (MALDI) and laser-induced acoustic desorption (LIAD). We presented our preliminary data, but showed that the results were not clearly due to the deposition of the GNP. We also investigated the deviations of measured mode shape from the theoretical mode shape, a critical piece of information that

is needed for NEMS-MS and NEMS-II analyses. We hypothesized potential causes for these deviations, but so far our tests showed that the deviations do not appear to originate from actuation method, actuation power, laser detection power, or anisotropic stress, nor do they appear to be controllable by methods of intrinsic-stress reduction.

5.2 Perspectives and Future Topics

In the final section of this thesis, we propose the following interesting research topics based on the experiments we performed.

While graphene has unique properties, making it an interesting candidate for NEMS switches, its single atomic layer characteristic makes them prone to damage, as shown in our prototype devices failing after fewer than 20 cycles. AlN and other materials may be better suited for the actual switch, and draping graphene over much more robust switches may create more optimal contacts and reduce friction. These factors could ultimately greatly increase the life expectancy of the mechanical switch.

From our experimental work with MALDI- and LIAD-based NEMS-MS and NEMS-II, more work is still needed before this approach can be used reliably. In particular, with both LIAD and MALDI, each laser pulse appeared to induce adsorption of both the analyte as well as a uniform coating of spurious fine particles to the device. This must be stringently controlled, given the huge area differences involved between the analyte contact area and the total active area of the NEMS sensor. Unlike a constant background which can be subtracted away, in this pulsatory approach to NEMS-MS and NEMS-II this spurious

background showed up along with the analyte signal with each pulse, and it is not impossible to distinguish between them – as is the case for continuous method involving use of electrospray ionization. Additional tests are needed to reduce the effects of background particles and to determine the maximum acceptable level of spurious adsorption per pulse.

Finally, we have demonstrated the deviations from idealized mode shapes that can occur in actual NEMS devices. Additional effort is required to understand and control the cause(s) of the deviations. These deviations appear to be rather generic – they are evident not just in AlN plates we have investigated, but also graphene membranes studied (but not commented upon) by others. Having accurate mode shapes is critical to accurate NEMS-MS and NEMS-II signal analyses. Once MALDI- and LIAD-based NEMS-MS and NEMS-II techniques have been perfected, they can be used to improve the capabilities of current mass spectrometry systems.